Photobase Effect in Carbon Dot based Photocatalysis

Jiawen Fang

from Zhejiang, China

Munich, July, 2021

Photobase Effect in Carbon Dot based Photocatalysis

Dissertation

submitted by

Jiawen Fang

Of Zhejiang, China

at the Faculty of Physics

Ludwig-Maximilians-Universität München

Munich, 06.07.2021

First reviewer:	Prof. Dr. Jochen Feldmann
Second reviewer:	Prof. Dr. Emiliano Cortes
Additional members of the examination:	PD Dr. Bert Nickel
	Prof. Dr. Bettina Lotsch

Date of oral examination: 05. 10. 2021

To my mother

for her endless support

List of publications, conferences and awards

Scientific publications of results presented in this thesis

J. Fang, T. Debnath, S. Bhattacharyya, M. Döblinger, J. Feldmann, J. Stolarczyk*. Photobase effect for just-in-time delivery in photocatalytic hydrogen generation. Nature communications, 11(1), 1-8 (2020).

J. Fang, Y. Wang, T. Debnath, J. Feldmann, J. Stolarczyk. intrinsically photobasic carbon dots in dual role: photocatalytic hydrogen generation and excimer lasing. Manuscript preparation

Additional publication

S. Rieger, T. Fürmann, K. Frank, J. Fang, V. Steidl, M Döblinger, B. Nickel, J. K. Stolarczyk, J. Feldmann. Thickness control of bismuth oxyhalide BiOX (X = Cl, Br, I) nanoplatelets for photocatalysis. Manuscript preparation

Conferences and Workshops

- Oral presentation at the "Workshop on Optical Spectroscopy of New Materials (OPTIMA)", Haigerloch, Germany (2019, March)

- The 11th International Conference on Quantum Dots, online conference, Munich, Germany, 2020, December

- Oral presentation titled "Just-in-time delivery: Photobase effect in photocatalytic hydrogen generation" in 9th SolTech Conference 2020, online conference, Bayreuth, Germany, 2020, October

- Oral presentation titled "Photobase Effect in Photocatalytic Activity of Carbon Dots" in Materials research society (MRS) fall meeting in Boston, Massachusetts, USA, 2019, December.

- Poster presentation titled "Photobase Effect in Photocatalytic Activity of Carbon Dots" in 8th SolTech Conference 2019, Nürnberg, Germany, 2019, October.

- poster presentation “” in CeNS/CRC235 Workshop "Evolving Nanosciences", Venice International University, San Servolo, Italy, 2019, September

- Attendee in 3rd Silicene workshop, International School of Solid-State Physics, Erice, Italy, 2018, July

- Attendee in 6 th SolTech Conference 2017, Munich, Germany, 2017, October

Award

CeNS Publication Award, Best Junior Scientist Publication
for “Photobase effect for just-in-time delivery in photocatalytic hydrogen generation” in Nature Communication
Munich, Germany, November 2020

Zusammenfassung

Die photokatalytische Wasserspaltung ist eine vielversprechende Strategie zur direkten Nutzung von Sonnenenergie für eine kostengünstige und nachhaltige Erzeugung von Wasserstoff. Photokatalysatoren, die auf organischen Materialien basieren, haben vor allem aufgrund ihrer leicht einstellbaren elektronischen Strukturen zunehmendes Interesse erlangt. Diese Arbeit behandelt in Speziellen metallfreie Kohlenstoffquantenpunkte (CDs). Einzigartige organische photophysikalische Effekte, einschließlich des photoinduzierten Protonentransfers und der langlebigen angeregten Triplett-Zustände, werden mittels zeitintegrierter und zeitaufgelöster optischer Spektroskopie untersucht und auf die photokatalytische Wasserspaltung angewendet.

Photokatalyse ist ein komplexer mehrstufiger Prozess, dessen Effizienz durch den langsamsten zugrundeliegenden Prozess begrenzt wird. Im Allgemeinen ist der Protonentransfer der ratenlimitierende Schritt (~μs). Einige organische Moleküle (Photobasen) haben eine höhere Protonenaffinität im angeregten Zustand als in ihrem Grundzustand, was darauf hindeutet, dass der Protonentransfer durch Licht manipuliert werden kann. Der photoinduzierte Protonentransfer wird als Photobaseneffekt bezeichnet. Diese organische photophysikalische Eigenschaft wird zum ersten Mal in der Photokatalyse genutzt, und es wurden zwei Systeme entwickelt: 1) ein nicht-photobasisches CD/photobasisches Molekül-Hybridsystem und 2) intrinsisch photobasische CDs. Es wird gezeigt, dass das photobasische Molekül, Acridin, innerhalb von 30 ps ein Proton aus Wasser im angeregten Zustand aufnehmen kann, was durch zeitaufgelöste Absorptionsspektroskopie nachgewiesen wird. Dies ermöglicht einen schnellen protonengekoppelten Elektronentransfer von CDs zu Acridin, wodurch die zeitliche Diskrepanz zwischen Protonendiffusion und Elektronenmigration reduziert werden kann. Die H_2-Erzeugungsrate wurde durch die Ausnutzung des Photobaseneffekts drastisch verbessert. Die intrinsisch photobasischen CDs können das Proton sogar innerhalb von 10 ps binden und erweisen sich als effiziente Photokatalysatoren. Der Photobaseneffekt erklärt, warum CDs als Photokatalysatoren funktionieren. Interessanterweise kann meine Entdeckung der stimulierten Emission in den photobasischen CDs möglicherweise zu gänzlich neuen zukünftigen Anwendungen in Exzimer-Lasern führen.

Die Lebensdauer der angeregten Zustände ist entscheidend für die photokatalytische Effizienz, was darauf hindeutet, dass die langlebigen Triplett-Zustände (>μs) für die Photokatalyse von Vorteil sein können. Hierfür wurden metallfreie phosphoreszierende CDs entwickelt. Ein Interkombinationsinhibitor wird eingesetzt, um die Besetzung der Triplett-Zustände zu kontrollieren. Es wird gezeigt, dass die Quantenausbeute der angeregten Triplett-Zustände reduziert wird, während die der angeregten Singulett-Zustände nahezu unverändert bleibt. Die Korrelation zwischen der ausgelöschten Phosphoreszenz und der stark reduzierten photokatalytischen Aktivität zeigt, dass angeregte Triplett-Zustände substantiell zur Photokatalyse beitragen. Die Arbeit ebnet den Weg zum Design organischer phosphoreszierender Materialien für die Photokatalyse.

Die Arbeit zeigt mithilfe von Untersuchungen mittels optischer Spektroskopie, dass der Photobaseneffekt und die langlebigen Triplett-Zustände für die photokatalytische Wasserstofferzeugung genutzt werden können. Die Arbeit schafft wichtiges Verständnis aufgrund dessen effiziente Photokatalysatoren auf der Basis organischer Materialien designt und deren photokatalytische Effizienzen optimiert werden können.

Abstract

Photocatalytic water splitting is a promising strategy for low-cost, sustainable production of hydrogen by utilizing solar energy. Photocatalysts based on organic materials have garnered increasing interest mainly due to the easily tunable electronic structures. Metal-free carbon dots (CDs) are the focus material in this thesis. The unique organic photophysics, including photoinduced proton transfer and long-lifetime triplet states, is investigated by time-integrated and time-resolved optical spectroscopy, and applied to photocatalytic water splitting.

Photocatalysis is a complex multi-step process, limited by the slowest step. Generally, proton transfer is the rate-limiting step (~μs). Some organic molecules (photobases) have higher proton affinity in the excited state, suggesting the proton transfer can be manipulated by light. The photoinduced proton transfer is called photobase effect. This organic photophysical property is utilized in photocatalysis for the first time, and two systems were developed: 1) a non-photobasic CD/photobasic molecule hybrid system, 2) intrinsically photobasic CDs. It is shown that the model photobasic molecule, acridine, can abstract a proton from water in the excited state within 30 ps probed by transient absorption spectroscopy. It enables swift proton-coupled electron transfer from CDs to acridine, which can reduce the timescale discrepancy between proton diffusion and electron migration. The H_2 generation rate has been dramatically improved where the photobase effect can manifest itself. The intrinsically photobasic CDs can even pull the proton within 10 ps and are proved to be an efficient photocatalyst. The photobase effect can explain why CDs work as photocatalysts. Interestingly, my discovery of stimulated emission in the photobasic CDs can possibly extend the application to the area of excimer laser.

The lifetime of excited states is decisive to photocatalytic performance, suggesting the long-lived triplet states (>μs) can be beneficial to photocatalysis. Herein metal-free phosphorescent CDs have been developed. An intersystem crossing inhibitor is employed to control the population of triplet states. It is demonstrated that the quantum yield of triplet states is reduced while that of the singlet states remain almost unchanged. The correlation between the quenched phosphorescence and dramatically reduced photocatalytic activity indicates that triplet states contribute to photocatalytic performance. The work paves the way to design organic phosphorescent materials for photocatalysis.

The thesis demonstrates that the photobase effect and long-lived triplet states can be applied to photocatalytic hydrogen generation after being investigated by optical spectroscopy. The work can pave the way to the design efficient photocatalysts based on organic materials and improve the photocatalytic efficiently.

Table of contents

Zusammenfassung ..... **IX**

Abstract ..... **XI**

Chapter 1 Introduction **1**

Chapter 2 Fundamentals **3**
2.1 Photocatalytic hydrogen generation 4
2.1.1 Thermodynamics 4
2.1.2 Light absorption 7
2.1.3 Charge separation 9
2.1.4 Surface reactions 10
2.2 Carbon dots (CDs) 12
2.2.1 What are carbon dots? 12
2.2.2 Optical properties 13
2.2.3 Origin of photoluminescence 15
2.2.4 Energy conversion applications 17
2.3 Photophysical process of organic molecules 20
2.3.1 Absorption 20
2.3.2 Radiative recombination 22
2.3.3 Nonradiative transition 25
2.3.4 Photobase effects 28
2.3.5 Room temperature phosphorescence 31

Chapter 3 Material synthesis and methods **35**
3.1 Synthesis of CDs 36
3.1.1 Nitrogen-free CDs 36
3.1.2 Photobasic CDs 37
3.1.3 Phosphorescent CDs 38
3.2 Structural analysis 39
3.2.1 Transmission electron microscopy (TEM) 39
3.2.2 Dynamic light scattering (DLS) 41
3.3 Photocatalysis setup and product detection 42
3.4 Identification of the photobase effect 43
3.5 Time-resolved and ultrafast spectroscopy 45
3.5.1 Time-correlated single-photon counting 45
3.5.2 Transient absorption spectroscopy 46

Chapter 4 Evidence of photobase effects on CDs photocatalysts **51**
4.1 Photobase effect in acridine 52

4.2 Attaching photobase to CDs 55
4.2.1 Optical properties of CDs 55
4.2.2 Optical properties of CD/photobase hybrid 56
4.3 Protonation dynamics 61
4.3.1 Protonation in acridine 61
4.3.2 Protonation in CDs/Photobase hybrids 66
4.4 Photocatalytic H_2 generation with CDs 68
4.5 Photocatalytic control experiments 71

Chapter 5 Intrinsically photobasic CDs for photocatalysis 73
5.1 Identification of the photobase effect 74
5.2 Protonation dynamics in CDs 78
5.3 Analogue to excimer emission 81
5.4 Photobasic CDs for photocatalytic water splitting 83
5.4.1 pH-dependence 83
5.4.2 Dependence on the ratio of urea/citric acid 85

Chapter 6 Using triplet states for photocatalysis 89
6.1 Evidence of long-lifetime triplet states 90
6.2 Triplet states on photocatalysis 94
6.2.1 Effects of the ISC inhibitor on triplet states 94
6.2.2 Effects of the ISC inhibitor on singlet states 96
6.2.3 Effects of the ISC inhibitor on photocatalysis 97
6.3 Heavy atom effect 98

Chapter 7 Conclusions and summary 101

Appendix 103

References 105

Acknowledgement 113

Chapter 1 Introduction

The global CO_2 emission has been rising dramatically since the industrial revolution. As the concentration of greenhouse gases increases, heat energy is trapped near the surface of the earth, resulting in global warming. The global average atmospheric carbon dioxide reached 415.26 ppm in 2021, the highest number in the past 800,000 years. The planet's average surface temperature has risen about 0.8-1.1 °C, threatening the ecosystem. The artificial carbon dioxide sources are directly linked to fossil combustion. In response, the EU has set an aggressive goal to reach carbon neutrality by 2050.

To mitigate the climate change and achieve the ambitious goal of carbon neutralization, new technologies are highly needed to be developed for harnessing sustainable energy sources. Hydrogen has been regarded as a promising, energy-rich and clean fuel. A promising hydrogen source is the abundant water that can be reduced to hydrogen via semiconductor-based photocatalysis. Photocatalytic water splitting has garnered growing attention in the past five decades as a promising method of renewable energy production without fossil combustion or carbon dioxide emission. It is an appealing concept of facilitating reactions between the photoinduced electrons and protons to produce hydrogen, and the driving force is coming from the sun. The approach can potentially provide a renewable solution to the global energy supply. The most extensively investigated photocatalysts are mainly from inorganic semiconductors, such as CdS and TiO_2. In the recent decade, organic materials have also risen as a new photocatalyst candidate, especially for carbon nitride and covalent organic frameworks, mainly due to the easily tunable electronic structure. In this thesis, carbon dots, composed of polycyclic aromatic hydrocarbons, are selected as a model organic photocatalyst, and are investigated by steady-state and time-resolved optical spectroscopy systematically.

Due to the complex electronic structure, photocatalysts based on organic materials are poorly understood. Thus, organic photocatalysis has not stimulated enough interest and suffers from a lack of systematic investigation. Approaches inspired by inorganic semiconductors have been always applied, such as heteroatom doping, to improve the photocatalytic activity of organic materials. Despite the progress these approaches have made, far less attention has been paid to utilize their organic photophysical properties in photocatalysis. For example, the protonation of some molecules can be controlled by light on an ultrafast timescale. Moreover, the nitrogen position in organic molecules/materials is crucial to the tradeoff between emission and photocatalytic activity. Just like the famous lecture “There’s Plenty of Room at the Bottom” given by Richard Feynman in 1959, there is also plenty of room for applying organic materials/molecules to photocatalytic water splitting. Could the unique organic photophysical properties in the excited state of organic semiconductor/molecules be utilized in photocatalytic water splitting? This thesis exhibits our efforts made to answer this question.

Before presenting the results, the fundamentals regarding photocatalysis and a concise introduction to organic photophysics are given first in **Chapter 2**. The present understanding of CD structure, optical properties, and the progress of applications is also included. **Chapter 3** will give a detailed introduction to the synthesis method, investigation tools, and optical spectroscopy applied. **Chapter 4** illustrates the trial of checking whether the photoinduced proton transfer, that is, photobase effect, contribute to photocatalytic water splitting. Generally, the lifetime of the photoinduced charge carrier is in the range of several nanoseconds, while the timescale of proton diffusion and photocatalytic reactions is around ~μs and ~ms, respectively. The large discrepancy in timescale between electron lifetime and proton diffusion can essentially limit the photocatalytic activity. A class of aromatic hydrocarbons, photobases, have one unique photophysical property: to pull the protons from the solvent in the excited state on an ultrafast timescale. Could the enchanting organic properties reduce the time discrepancy in photocatalytic water splitting? Such an effort has been made in this chapter. **Chapter 5** illustrates the trial to make intrinsically photobasic CDs and apply them to photocatalytic water splitting. As the photobasic moieties are also embedded in many organic materials, such as carbon nitrides, can the moieties make organic materials photobasic? Finally, **Chapter 6** gives a trial of applying the long-lifetime triplet states in photocatalysis based on metal-free room temperature phosphorescent materials. Triplet states generally have a much longer lifetime (>μs) than that of singlet states (~ns). Could triplet states be utilized in photocatalytic hydrogen generation? **Chapter 7** summarizes the work and gives an outlook on applying organic materials/molecules to photocatalyst.

Chapter 2 Fundamentals

The first part of the chapter focuses on the photophysical processes and physical concepts related to photocatalytic hydrogen generation. The photocatalytic activity mainly depends on the efficient absorption, charge separation and conversion of the energy from the sun, which will be extensively discussed. Moreover, carbon dots (CDs), a new metal-free and non-toxic organic photocatalyst, is employed in this thesis. The current interpretation of structure, optical properties and progress of the applications will be presented. In the final part, as CDs are composed of polycyclic aromatic hydrocarbons, the related organic photophysical properties of organic molecules in the excited state will be discussed.

2.1 Photocatalytic hydrogen generation

2.1.1 Thermodynamics

The energy stored in the chemical bond of fuels can be released by combustion and used for daily life. Due to the growing demand for renewable energy, hydrogen, a zero-carbon fuel, has been considered the perfect fuel since decades ago. However, producing hydrogen from low-carbon energy is costly at this moment. In the ideal case, solar energy can be used directly to drive hydrogen production. To this end, solar energy is used to drive the energetically uphill reactions and produce the high-energy compound from water (**Fig. 2.1a**). As shown in **Fig. 2.1b**, the absorption of light can increase the rate of the endergonic reaction, where the sign of the Gibbs free energy change is inverted to negative. In this way, water splitting is thermodynamically possible. Here the established principles related to inorganic semiconductor-based photocatalysis are introduced first.

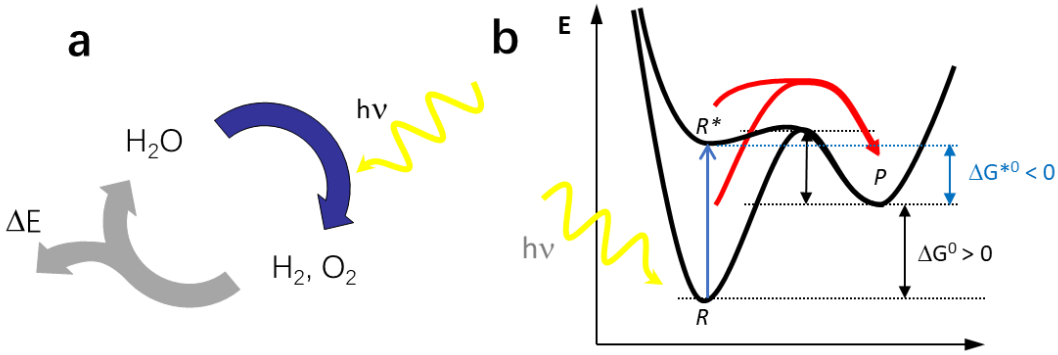

Figure 2.1 a) solar energy storage and conversion of H_2O into chemical fuels. b) Energy diagram of photoinduced endergonic reactions.

In 1972 Honda and Fujishima reported for the first time that semiconductor-based water splitting could be driven by light [1]. This pioneering work triggered decades' ever-growing enthusiasm and efforts to investigate the mechanism, design photocatalytic semiconductors, and improve the efficiency [2-9]. The overall water splitting reaction comprises the hydrogen evolution reaction and oxygen evolution reaction (**Eq. 2.1-2.2**) [10]. Listed along the equations are the related standard redox potential $\Delta E°$ and the Gibbs free energy $\Delta G°$. Water splitting into H_2 and O_2, thermodynamically, is an uphill reaction as the Gibbs free energy is a considerable positive value, +237.2 kJ·mol^{-1} (**Eq. 2.3**). The oxygen evolution reaction is more difficult and complicated as four electrons are needed to drive the oxidation reaction to remove four protons [11].

$$\mathbf{2H^+ + 2e^- \rightarrow H_2\ (g)}\ (\mathbf{\Delta E° = -0.41\ V}) \quad (2.1)$$

$$2H_2O\ (l) \rightarrow O_2\ (g)\ + 4H^+ + 4e^-\ (\Delta E° = +0.82\ V) \quad (2.2)$$

$$H_2O\ (l) \rightarrow H_2\ (g) + \frac{1}{2}O_2\ (g)\ (\Delta G°{=}{+}237.2\ kJ{\cdot}mol^{-1},\ \Delta E°{=}\ {+}1.23\ V,\ pH = 7) \quad (2.3)$$

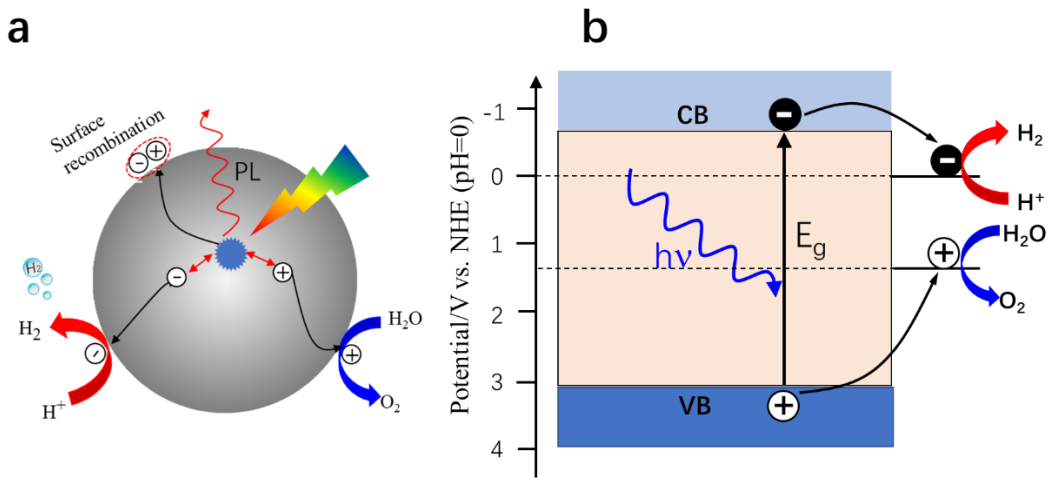

Figure 2.2. Schematic diagram of semiconductor-based photocatalytic water splitting. a) photon absorption and the charge carrier pathway; b) energy diagram of the same process.

The fundamental principle of photocatalytic H_2 generation by semiconductors has been investigated in detail [4, 12], and schematically described in **Fig. 2.2**. After absorption of an incident photon, an electron-hole pair is photogenerated inside the semiconductor nanocrystal and further dissociated into free charge carriers (electron and hole). To achieve the photocatalytic reaction, fast electron and hole recombination must be avoided and the free charges should migrate separately to the reactant species bound at the surface [13, 14]. The photoinduced electrons and holes can reduce protons and oxidize water molecule, respectively, as illustrated in **Fig. 2.2(a)**. Nevertheless, the oversimplified processes neglect the driving force for the charge separation and transfer, while the energy diagram can offer more information, as shown in **Fig. 2.2 (b)**. If the excitation energy is larger than the bandgap (Eg) of the semiconductor, an electron will be promoted to the conduction band (CB), leaving a hole behind in the valence band (VB). The photoexcited carriers relax down to the respective band edge via thermalization and achieve a quasi-equilibrium carrier distribution. Therefore, the energy positions of CB minimum (CBM) and the VB maximum (VBM) determine the ability of reduction and oxidation of photoexcited electrons and holes, respectively. The chemical potential of the quasi-Fermi levels of electrons and holes at the band edges intrinsically (F_n and F_p) can be calculated according to [15, 16]

$$\boldsymbol{F_n = E_c + k_B T \cdot \ln \frac{n}{N_c}} \tag{2.4}$$

$$F_p = E_v - k_B T \cdot \ln \frac{p}{N_V} \tag{2.5}$$

where E_C and E_V are the energy values corresponding to the CBM and VBM, respectively; k_B is the Maxwell-Boltzmann distribution constant; T is the absolute temperature; n and p are the corresponding density of electrons and holes, respectively; N_C and N_V are the related densities of states at CBM and VBM, respectively.

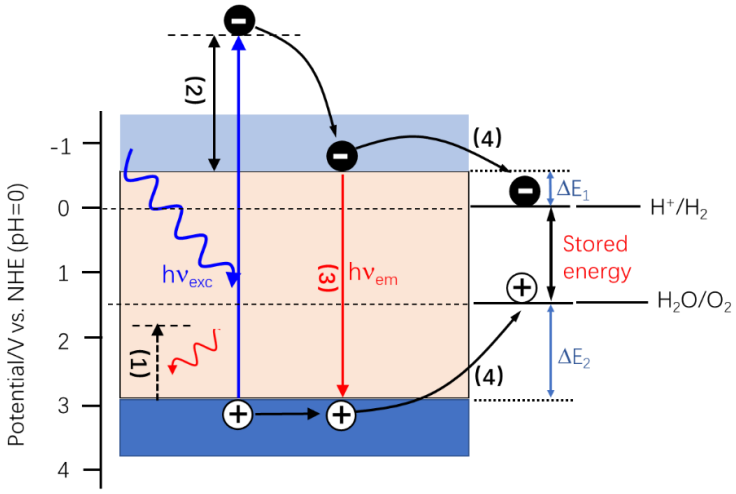

Figure 2.3. The bandgap diagram of semiconductor nanocrystals together with a redox potential of water photoreaction. The energy loss pathways are depicted: (1) below bandgap photon, (2) thermalization, (3) charge recombination, (4) overpotential.

Not every photon can be absorbed by a semiconductor. To achieve overall water-splitting over a single photocatalyst, the VBM and CBM of photocatalyst mast exceed the redox potential of H^+/H_2 (0 eV vs NHE at pH 0.0) and O_2/H_2O (+1.23 eV vs NHE at pH 0.0), as shown in **Fig. 2.3**. In other words, the CBM must be energetically higher than the reduction potential of water splitting, while the VBM should be energetically below the oxidation potential. In this way, it can provide overpotentials for both the transfer of an electron and a hole to the corresponding reaction sites.

The energy difference between the hydrogen reduction potential and oxidation half-reactions amounts to the energy available for the photocatalytic process [17]. Generally, only part of the energy can drive the photocatalytic reactions, as the energy loss results from undesired reactions and energy partial loss. The detailed process is illustrated in **Fig. 2.3**. Firstly, the photons with insufficient energy to lift electrons to the conduction band would not be absorbed. Therefore, a large solar energy ratio will be lost, especially for the semiconductors with an absorption onset in the UV range (**Process (1)**) [18]. Secondly, after absorption of photons with sufficient energy, the semiconductors will generate hot charge carriers followed by fast thermalization (**Process (2)**). Thirdly, the electronic transition probability is another constraint of the actual light absorption. Forbidden transitions usually have small absorption coefficients. Accordingly, far fewer photons can be utilized. Therefore, the semiconductors with allowed bandgap transition are the best candidates for photocatalysts. Moreover, the carrier recombination, both radiatively and nonradiatively, can occur both in bulk and at the surface, constituting the third energy loss channel (**Process (3)**) [19]. Finally, the overpotential between the conduction/valence band edge and the redox level boosts the charge transfer, and the energy is dissipated (**Process (4)**).

The energy loss pathways described above are only applicable to stable semiconductors where photoinduced electrons and holes do not reduce or oxidize the nanocrystal itself [20]

or the surface stabilizing agents [21]. The situation usually occurs if the redox potential of the semiconductor lies above the water oxidation potential. For example, the oxidation of lattice ions (S^{2-} to SO_4^{2-}) has been found in chalcogenide II-VI semiconductors [20, 22], which leads to nanocrystal dissolution. Moreover, if the stabilizing ligands are oxidized and tend to desorb, the nanocrystals are expected to aggregate. To avoid the situation, hole scavengers, typically reducing agents, are usually incorporated to deplete the holes. The hole scavengers can also balance the slow hole transfer limiting the overall rate [23, 24]. To select an appropriate hole scavenger, the scavenger's redox potential is required to be above the oxidation level of the semiconductor. In this way, the hole would preferably transfer to the scavenger [25-27]. The same rule applies to electron scavengers to prevent reductive photodegradation. Employment of sacrificial agent constitutes another energy loss mechanism because the stored energy is accordingly dissipated [16]. The thesis focuses on photocatalytic hydrogen production, and hole scavengers are employed to deplete the holes.

2.1.2 Light absorption

As discussed previously, only a small value of energy, 1.23 V, theoretically, is required to split water. However, the value is far from enough as extra overpotentials are required to overcome kinetic constraints. Generally, the photocatalytic active materials have bandgaps larger than 3.5 eV [11, 28, 29]. According to Marcus' theory, a larger overpotential will result in faster charge transfer to the reaction sites [30]. A wider bandgap amounts to a larger overpotential, but the photons absorbed are limited to smaller energy. Thus, only a limited range of the solar spectrum can be utilized. Therefore, a tradeoff has to be made between a wide bandgap to gain enough overpotential and the photons with lower energy absorbed. To utilize the visible light range in solar energy, the absorption range must be extended while satisfying the thermodynamic constraints. Generally, three methods have been widely utilized: 1) multiple photons absorption of below-gap photons to reach the CB (up-conversion)(**Fig. 2.4a**) [31]; 2) sensitization to extend the absorption onset (**Fig. 2.4b**) [32, 33]; 3) introduction of defect states to reduce the bandgap (see **Fig. 2.4c**) [34].

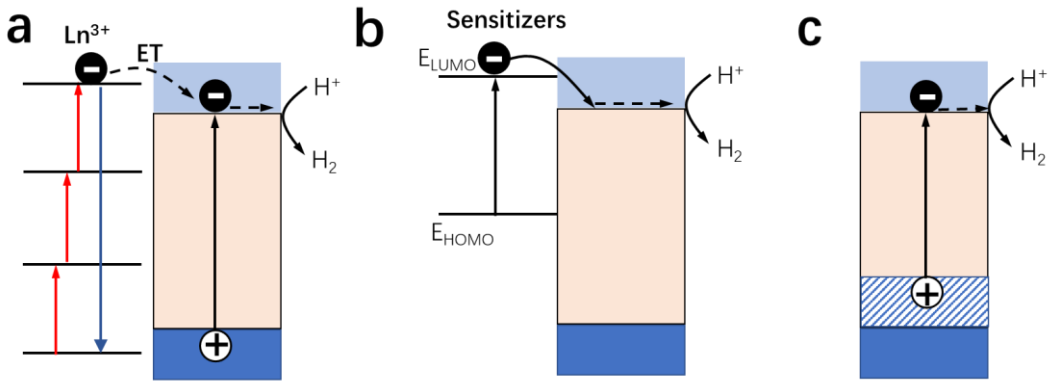

Figure. 2.4 Methods of light absorption extension of semiconductors with large band gaps, (a) up-conversion. b) sensitize the semiconductor with a dye or another semiconductor, c) lift the valence band or introduce defect states.

Starting with multiphoton absorption, the photons with low energy, especially the near-infrared (NIR) part of the solar spectrum that cannot drive the photoreactions, can be utilized. Multiphoton absorption simultaneously can lift electrons to a higher energy state by virtual states. Unfortunately, it can only be achieved under very high illumination intensity, which is not applicable to the photocatalysis system. However, inorganic materials containing *d*-block or *f*-block elements can also upconvert two or more sequential photons into one photon emission with higher energy [35-37]. A typical case is lanthanide-doped nanoparticles, where the up-conversion can take place via intermediate 4*f* states. Therefore, through the delicate selection of dopants (Er^{3+}, Yb^{3+}, Tm^{3+}) and design [38, 39], the emission can shift to ultraviolet range while the semiconductor absorbs NIR light. In this way, wide bandgap semiconductors, typically TiO_2, can be sensitized via energy transfer [40-42] **(Fig. 2.4a)**.

The second approach is to decrease the energy to lift electrons to the CB to extend the absorption onset. A general solution is to introduce a visible light active molecule/dye requiring that the LUMO of the molecule is close to the CB of the semiconductor. In this way, the photoinduced electrons can easily be injected into the conduction band of a wider bandgap semiconductor (**Fig. 2.4b**). The hole scavenger can regenerate the molecule that functions as a dye in dye-sensitized solar cells [2, 33]. The best dye candidate reported is the dye $Ru(bpy)_3^{2+}$ with an extraordinary long metal-ligand charge transfer lifetime [43-45]. Meanwhile, a variety of quantum dots (CdS, CdSe) can also function as a sensitizer as long as it has a higher energy conduction band edge than the paired semiconductor [46-48]. Metal nanoparticles, especially Au and Ag, have also been investigated as a sensitizer to couple the wide bandgap semiconductors [49-51]. They have a much stronger absorption capability as the metal nanoparticle usually has a robust localized surface plasmon resonance. After being excited, the surface plasmon can charge transfer to the semiconductor, similar to the process in a dye-sensitized solar cell [52-55].

The third alternative approach is to decrease the band gap while retaining the semiconductor oxidative properties. In oxide semiconductors, the valence band edge composed of O 2*p* orbitals is low, typically approximately +2.9 V vs. NHE at pH 0. The number is relatively large compared with +1.23 V (NHE at pH 0) for ideal water oxidation. Meanwhile, there is little room for the reduction side as the margins are narrow [34]. Therefore, lifting the valence band edge is key to narrowing the bandgap. To this end, nitrogen atoms can be introduced and hybridized with the O 2*p* orbitals to lift the valence band edge [56] (see **Fig. 2.4c**). A typical case is tantalum oxide. After nitrogen hybridization, the bandgap is primarily reduced from 3.7 eV [27] to 2.4 eV [57], while the conduction band edge remains the same. Nitrogen-doped tantalum oxide has been proven as an efficient photocatalyst [58-60]. Meanwhile, lattice defects can also induce additional states and extend the visible light absorption. A notable example is that the bandgap of active black TiO_2 is reduced to 1.54 eV due to O vacancies and Ti interstitials [61, 62].

2.1.3 Charge separation

The photogenerated carriers can either recombine or further migrate to the reaction sites at the nanocrystal surface. Generally, the carrier lifetime is an indicator of the photocatalytic efficiency of photocatalysts. A short lifetime indicates that the majority of carriers recombine before reaching the reaction sites. Typically, the photogenerated carrier lifetime of semiconductors is on nanosecond timescale [63-65], while the timescale of the water reduction reaction is milliseconds, and the water oxidation reaction even requires seconds [11]. Therefore, there exists a significant timescale mismatch between the carrier recombination and the typical photocatalytic reactions. To address this issue, continuous efforts have been made to retard the carrier recombination and increase surface reaction rates. In addition, the metal-semiconductor and semiconductor-semiconductor heterojunction [13] can improve charge separation, as schematically shown in **Fig. 2.5**.

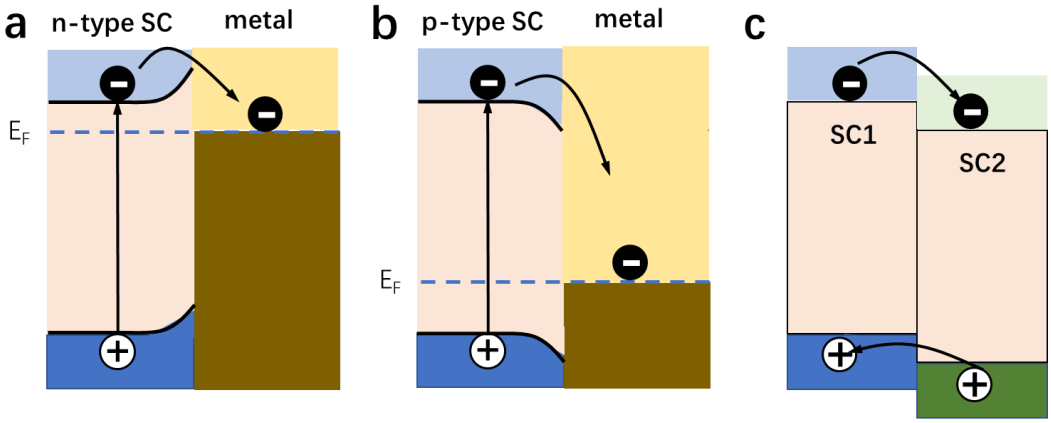

Figure 2.5. Metal-semiconductor and semiconductor-semiconductor heterojunctions to separate carriers spatially to improve charge separation: (a) n-type semiconductor-metal junction; (b) p-type semiconductor-metal junction; (c) pair semiconductors with Type II band alignment.

The scheme of metal–n-type semiconductor junction is illustrated in **Fig. 2.5a**. If the semiconductor's CBM is energetically higher than the Fermi level of the metal, the photoinduced electron of the semiconductor will transfer to the metal. Meanwhile, the Schottky barrier at the interface will prevent electron back-transfer [46]. The subsequent electron transfer from the metal to the adsorbate can also be facilitated. In this case, the metal nanoparticle functions as an electron sink in the metal-semiconductor composite. As a result, the Fermi level shifts upward, making the metal more reductive. Similarly, in a p-type semiconductor-metal junction, the photoinduced electrons can easily transfer to the metal. As the energy barrier would impede the hole transfer, charge separation can be improved as well (**Fig. 2.5b**). That is why noble metal nanoparticles (Pt, Au) are usually added as co-catalysts to the photocatalytic system [34, 66].

Efficient charge separation can also be achieved simply through the Type II band alignment of two semiconductors [67, 68]. As illustrated in **Fig. 2.5c**, the electrons and holes transfer in opposite directions and are confined spatially afterwards. The small wavefunction

overlap will result in a longer lifetime. If only one semiconductor is selectively excited, only one carrier will move across the interface while leaving the other behind. The process is identical to sensitization. Type II alignment has been widely used in photocatalytic systems, and a typical example is CdS/TiO_2 [68, 69].

2.1.4 Surface reactions

After the photoinduced carriers reach the surface of the nanocrystals, they can participate in water reduction. Many semiconductors have been reported with sufficiently reductive conduction bands to reduce water [52]. They are listed in **Fig. 2.6**. Among those, several nanocrystals, TiO_2, ZnO, CdS and CdSe, have been extensively investigated as photocatalyst candidates [6, 11, 34, 65]. As discussed previously, noble metal co-catalysts are always included to lower the overpotential to boost hydrogen generation. Platinum nanoparticles are the best choice as platinum has very low overpotential (only 150 meV) above the water reduction potential [5].

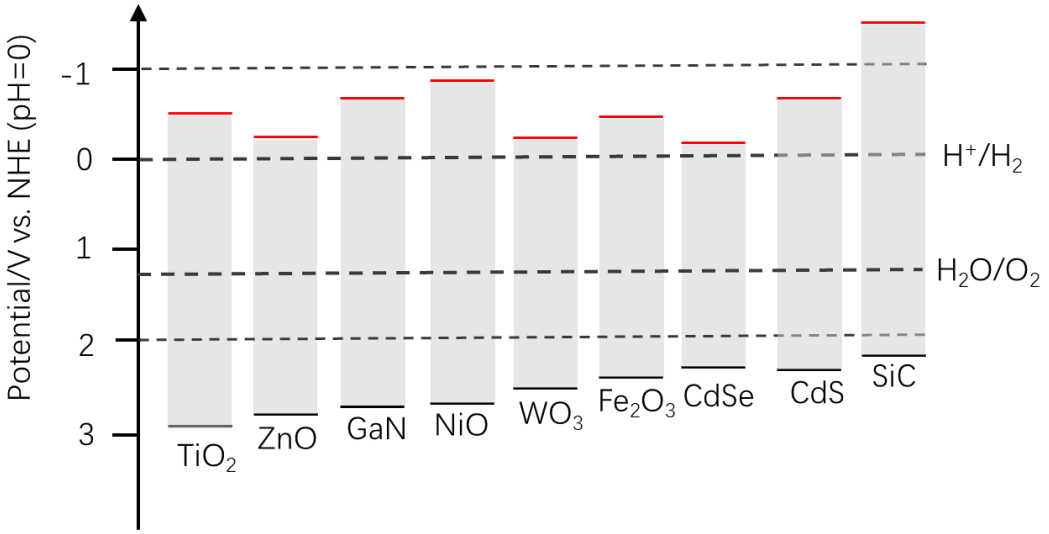

Figure 2.6. Band alignment of several semiconductors with redox potentials of water reduction and oxidation.

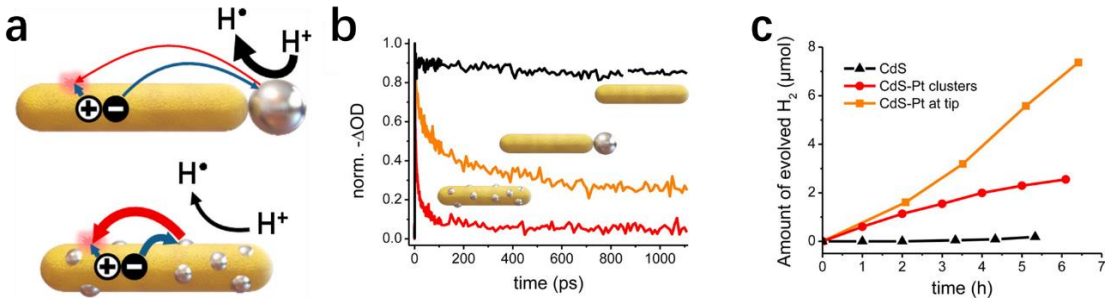

Figure 2.7. (a) Comparison of charge recombination rates in two kinds of platinum decorated CdS nanorods. (b) Relaxation of the bleach in transient absorption for nanorods with/without platinum. (c) photocatalytic reduction rate. [adapted from Reference [70]].

Pt tip-decorated CdS nanorods were designed to investigate the role of pathways for the photoinduced electrons to the co-catalyst [70, 71], as illustrated in **Fig. 2.7a**. Pt nanoparticles were selectively decorated at the rod tips or randomly distributed on the rods. The nanostructure belongs to the metal-semiconductor system. Upon excitation, the photoinduced electron is transferred to the Pt nanoparticle while the hole is depleted by a hole scavenger. Surprisingly, shortening the transfer path by random deposition of Pt nanoparticles at the surfaces increased the transfer rate but deteriorated the photocatalytic performance. It shows that the random hole trapping on the surface is harmful to photocatalysis, which can be solved by localization of holes away from the reaction site by the longer-distance separation (**Fig. 2.7b,c**). In this case, the tip-decorated nanorods are a more efficient photocatalyst, as the photoinduced carriers have a much longer general distance to the Pt nanoparticles.

Accumulated evidence proves that the electron transfer takes place quite efficiently. However, it is not the case for hole reactions. CdS nanorods decorated with Pt clusters were coupled with different hole scavengers and their photocatalytic performances were compared [72]. The resulting hydrogen generation rates were found to correlate with the redox potential of the scavenger. It is because the larger overpotential will result in a faster hole transfer and depletion. The longer lifetime of electrons can lead to a faster H_2 generation rate, which implies that the hole transfer is also a crucial rate-limiting step. The result is consistent with previous carrier dynamics studies [23, 24].

2.2 Carbon dots (CDs)

The previous section has discussed the fundamental aspects of inorganic semiconductor-based photocatalysis. In this thesis, an organic material, carbon dots, are utilized for photocatalysis due to its non-toxic, metal-free, and easily tunable electronic structure.

2.2.1 What are carbon dots?

Carbon dots are zero-dimensional carbon-based materials with a size of less than 10 nm. CDs were first discovered during the electrophoretic purification of carbon nanotubes fabricated by arc-discharge methods in 2004 (**Fig. 2.8a)** [73]. As a new class of carbon nanomaterials, CDs show tunable fluorescence and exhibit unique optical and electric properties. Immediately, they have attracted growing attention [74-76]. **Fig. 2.8** lists several memorable milestones from the course of CDs development. In 2006, it was the first time to employ surface passivation to greatly enhance the emission by altering surface chemistry [74] **(Fig. 2.8b)**. In 2010, the size-controlled CDs were successfully isolated, showing size-dependent photoluminescence [77] (**Fig. 2.8c**). In 2013, polymers were used to synthesize CDs for the first time (**Fig. 2.8d**). In 2016, chiral CDs were reported for the first time, extending the CDs application [78] (**Fig. 2.8e**). In 2018, the homogeneous triangularly shaped CDs were synthesized, and the bandwidth of the emission is ultra-narrow [79] (**Fig. 2.8g**). Inferred from the course of CDs development, we can conclude that pure and size-homogeneous CDs with well-defined structures are growingly demanded and developed for investigation and extending the applications.

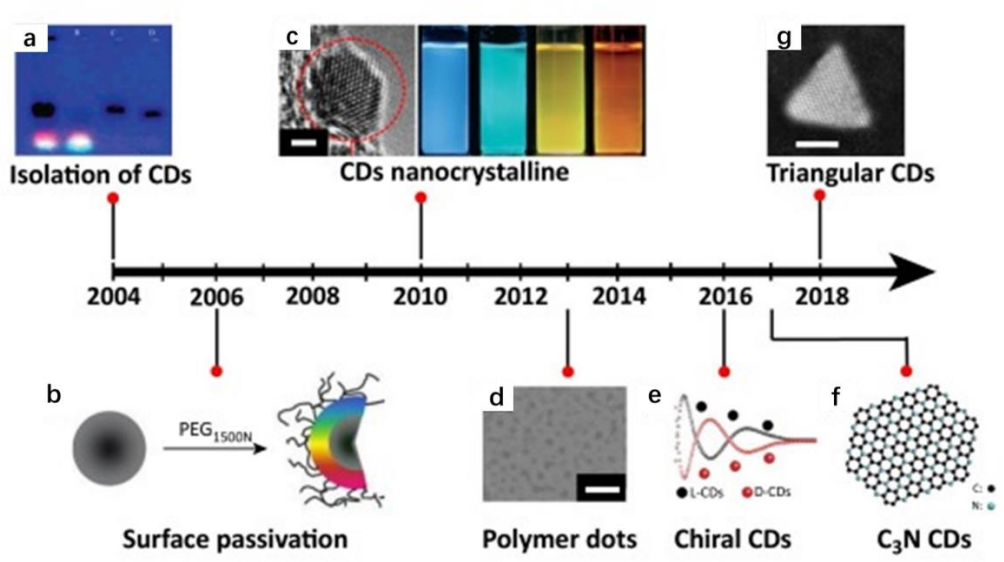

Figure 2.8. Selected major milestones in CDs development. (a) CDs were first found via gel electrophoresis of carbon nanotube. (b) CDs passivation to be more emissive. (b) Crystalline CDs and size-dependent fluorescence (d) fluorescent polymer dots; (e) Circular dichroism spectrum of chiral CDs; (f) The chemical structure of the C_3N CDs. (g) morphology-controlled CDs. [adapted from Reference [80]].

The various polar functional groups, including hydroxyl, carbonyl and amino, render CDs with superior water solubility. CDs are also suitable for surface functionalization with organic, inorganic, even biological species [81, 82]. Meanwhile, CDs also exhibit robust chemical photostability and possess better biocompatibility, lower toxicity than traditional semiconductor quantum dots. As a new fluorescent nanomaterial, CDs have shown broad applications, including chemical sensing [83], photodynamic therapy [84], bioimaging [85], drug delivery [86], and photocatalysis [87]. Due to the interesting optical properties, metal-free CDs have been the focus materials for photocatalytic applications throughout this thesis.

2.2.2 Optical properties

Though having diverse chemical structures, the absorption spectra of CDs share a similar feature where a strong absorption appears in the UV range with a tail extending into the visible region [88-91]. A representative absorption spectrum is shown in **Fig. 2.9(a)**. For example, the CDs synthesized from the citric acid and urea usually have an absorption band around 280-340 nm [92, 93]. To better interpret the CDs' optical properties, CDs have long been regarded as large organic molecules. Unlike the absorption of inorganic semiconductor quantum dots constrained by the quantum confinement [94, 95], the absorption of CDs results from transitions induced by non-bonding (n)/lone-pair orbital (l) in the functional group and conjugated electron (π) in the sp^2 hybridized nanodomain [96, 97]. The absorbance in the longer wavelength range is due to the $\pi \rightarrow \pi^*$ transitions from aromatic carbon and $n \rightarrow \pi^*$ transitions from heteroatom dopants/functional groups [80, 86, 98]. The absorption spectra shape and intensities can be modulated through solvent selection, surface modification, and heteroatom doping [76, 99]. Because of the broad, featureless absorption spectra and their complex nature, limited information can be gained from the absorption spectra alone. However, with photoluminescence excitation spectra, the states contributing to the emission can be more easily revealed.

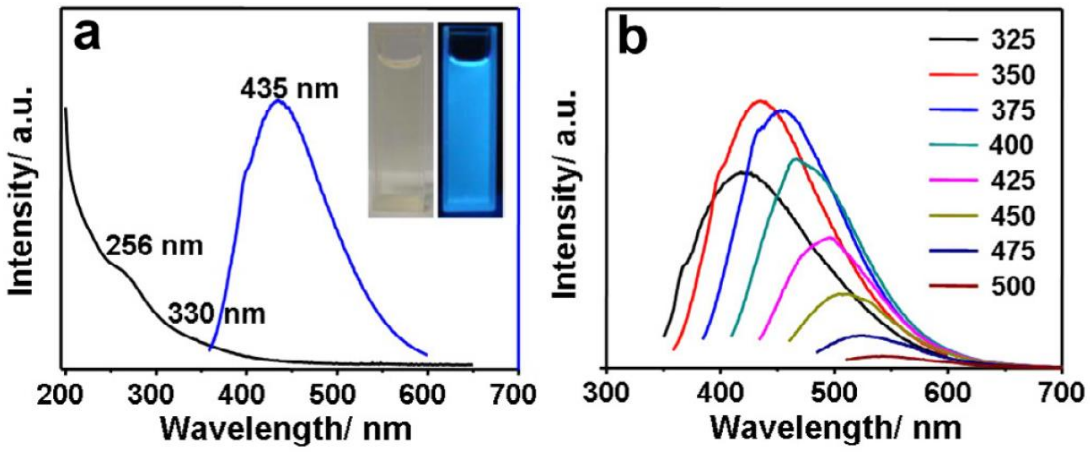

Figure 2.9. Representative absorption spectra (a) and excitation dependent fluorescence (b) of CDs. The inset is optical images of CDs under daylight (left) and UV light (right). [adapted from Reference [100]].

The most notable feature of CDs is the excitation wavelength-dependent photoluminescence. Thus, CDs can exhibit different colors with different excitation wavelength. Generally, CDs have strong emission in the short-wavelength region, but the intensity decreases rapidly in the long-wavelength region [92, 99], as shown in **Fig. 2.9b**. In most cases, the photoluminescence spectrum of CDs is broad and structureless due to the heterogeneity in size and complicated photophysics involved [99]. The main reason for the dispersity is due to poorly controllable synthesis processes. Moreover, the PL spectrum always accompanies a significant Stokes shift, which can even be more than 100 nm [93].

Great efforts have been made to control the broadness and intensity of CDs emission delicately. In the view of molecular fluorescence, to design the optical properties of CDs is to mainly control the conjugation length and introduction of functional groups [101]. The conjugation lengths are significantly affected by the precursors and the synthesis condition. The electronic structures of the resulting CDs are primarily affected by the precursors. Selecting aromatic precursors, such as 1,3,6-trinitropyrene, m-phenylenediamine [102], is the shortcut to achieve narrow-bandgap CDs. While for non-conjugated precursor, for example, PEG, the resulting CDs usually have strong absorbance/emission only in the UV range [103]. Meanwhile, the temperature, solvent selection and reaction time will decide the carbonization and dehydration process [90]. A delicate selection of experiment parameters can control the conjugation length of the resulting CDs. Even non-aromatic precursors can result in CDs with emission varying from UV to NIR range with the suitable experimental parameters [90]. Surface functionalization provides another intriguing method to modify the optical properties. The related research has been upgrading from directionless surface functionalization to directional surface functionalization. In the initial research period, a typical example of directionless surface functionalization is strong acid treatment. The functional groups at the surface would be unselectively oxidized into carboxyl, carbonyl [74]. Nowadays, specific functional groups will be targeted and transformed into another. Especially some groups that are electron acceptors can be functionalized and transformed into electron donors. For example, the carboxylic acid groups at the surface can be aminated [79]. The surface functionalization will notably change the optical properties of CDs.

CDs can be both excellent electron donors and electron acceptors [104]. The CDs synthesized by laser ablation have PL emission centered 425 nm, which can be quenched by the electron acceptor 4-nitrotoluene (-1.19 V versus NHE). The corresponding Stern-Volmer quenching constant is 38 M^{-1}, and the biomolecular rate constant was found 9.5×10^{9} $M^{-1}s^{-1}$, and the immense value suggests the highly efficient electron transfer process. The quenching constant proves that the CDs can function as an efficient electron donor. Meanwhile, the CDs were also found an efficient electron acceptor, as they can quench the fluorescence of electron donor, N,N-dimethylaniline (0.88 V versus NHE at pH 0) efficiently. The quenching phenomenon was independent of solvents and was more efficient in polar solvents.

2.2.3 Origin of photoluminescence

The interpretation of the complicated PL spectra of CDs has been a challenging task. Though significant progress in the CDs synthesis, the origin of fluorescence emissions remains a debatable topic [93, 97, 105]. Nowadays, several approaches have been developed to interpret the PL mechanisms of CDs. There are mainly two plausible mechanisms proposed. The first one is the research of Fu *et al*. who claimed that the typical Stokes shift in CDs is due to the exciton self-trapping process [93]. They viewed CDs as polycyclic aromatic hydrocarbons (PAH). A model system to mimic CDs fluorescence was employed where three typical different conjugated PAHs (anthracene, pyrene, and perylene) were dispersed in poly(methyl methacrylate), an amorphous matrix, and the results are shown in **Fig. 2.10 (a-c)**. Films containing PAH molecules exhibited CD-like absorption and fluorescence wavelengths, along with the large Stokes shifts. Interestingly, the excitation wavelength-dependent photoluminescence was only observed in films containing all three PAHs (**Fig. 2.10c**). Thus, the excitation-dependent emission is proposed to be due to energy transfer between PAHs with different energy gaps. In this regard, CDs can be viewed as different sp^2 domains embedded in a sp^3 amorphous matrix. The concentrated CDs can form excimer, which result in the formation of self-trapped exciton. The energy of self-trapped exciton is reduced by several hundred millielectronvolts than free excitons, which can explain the large Stokes shift in CDs (**Fig. 2.10d**). In this way, surface functional groups or surface functionalization in the amorphous matrix were suggested minor effects on the observed optical properties.

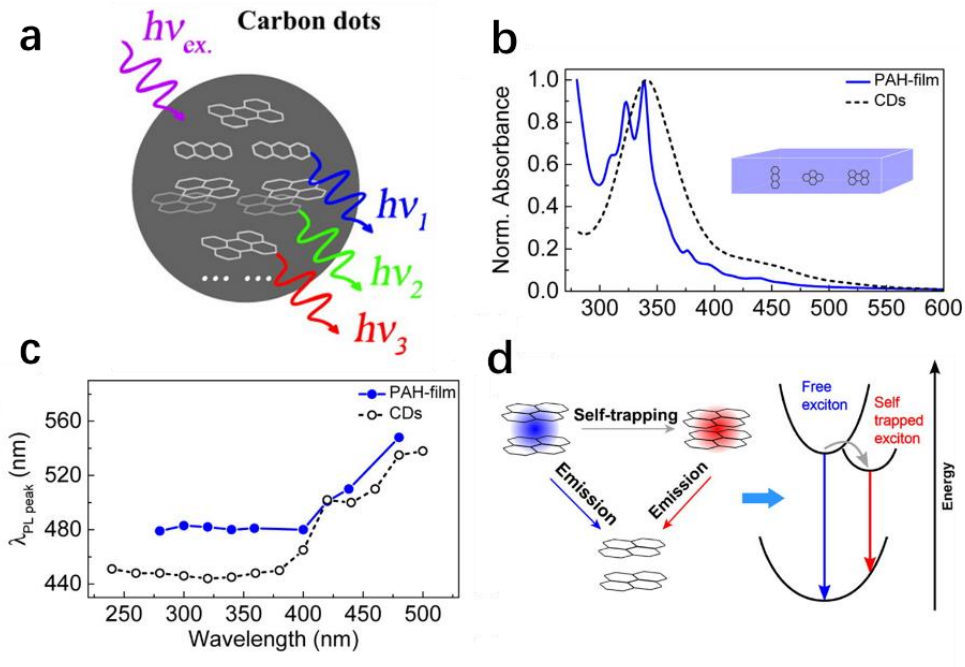

Figure 2.10. a) The optical properties of CDs were modelled by three typical PAHs (anthracene, pyrene, and perylene); b) normalized absorption of blended PAHs and the CDs in solution; c) Excitation dependent PL peak location; d) Scheme of the self-trapping exciton in a pyrene molecule pair with reduced energy. [adapted from reference[93]].

The second reasonable argument is that the surface/edge plays the most crucial role in affecting the CDs' photoluminescence [105-107]. It can be partially evidenced by the fact that the shape and intensity of PL spectra can be modulated mainly by the pH value of the solvent. There are also various functional groups sensitive to pH evidenced by the Fourier-transform infrared spectroscopy characterization. The various arrangements of the functional groups can bring many possibilities. Even with the same carbon core (in other words, carbon nanodomain), different arrangements of functional groups connected with the core can result in different energy states. Thus, different CDs can have different electronic structures. The energy transfer between different CDs can result in excitation-dependent emission. Sun *et al.* proved that the emission of CDs could be adjusted significantly by tuning the amount and species of functional groups [108]. Xiong *et al.* reported a series of excitation wavelength-independent CDs purified through column chromatography. The resulting CDs are found to possess an increasing degree of surface oxidation [107], showed in **Fig. 2.11a**. The correlation between surface oxidation and fluorescence wavelength shows that the bandgap reduces with the increasing oxygen content, as plotted in the scheme **Fig. 2.11b**. Therefore, surface oxygen species play a crucial role in affecting the optical properties.

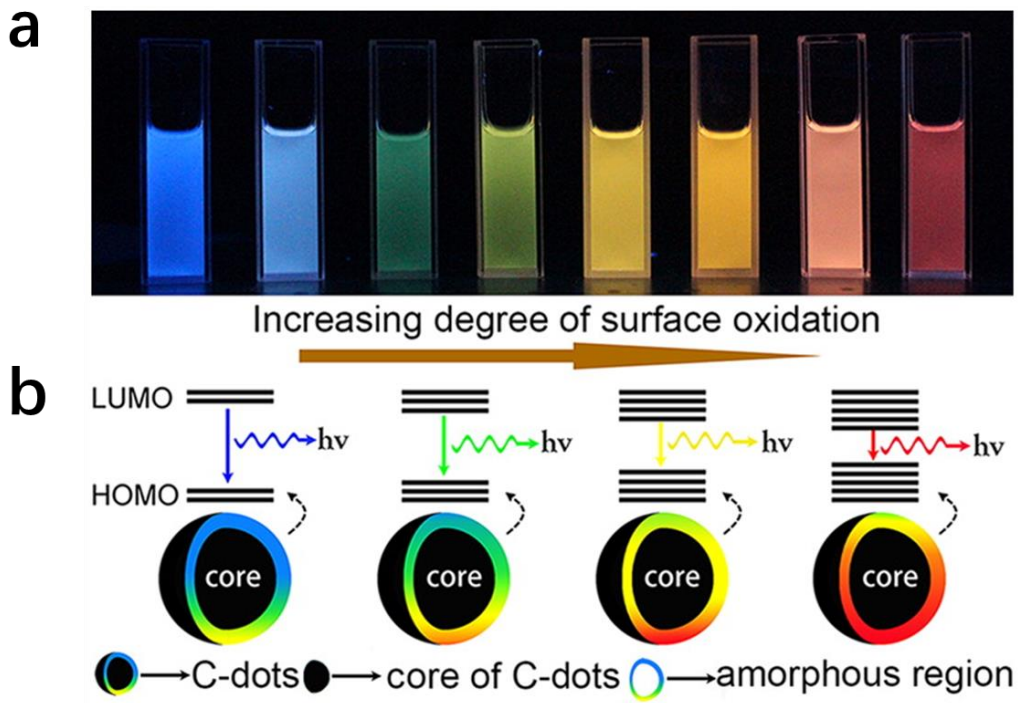

Figure 2.11. a) The emission color of eight separated and purified CDs via silica column chromatography with 365 nm excitation. b) scheme for the tunable PL of CDs with different degrees of oxidation. [adapted from reference [107]]

Besides the oxygen-containing groups, the amine group has also been reported to be responsible for the strong emission in CDs. Tetsuka et al. reported a method to grant CDs with an edge-terminated amine [109]. The effective orbital resonance modifies the electronic structure of CDs. It was evidenced by the redshifted emission peak with

increasing numbers of amine groups. The resonance feature between the non-bonding orbital of NH_2 groups and the delocalized π orbital of core results in narrowing the optical bandgap.

2.2.4 Energy conversion applications

Although many parameters involved in the optical properties make the relaxation process complicated in CDs, solutions have been explored to reduce the nonradiative relaxation and apply CDs to energy conversion applications. Besides that, CDs also have the advantages of low cost, non-toxicity and tunable electronic properties. Here two applications are introduced, blue-light OLEDs and photocatalysts.

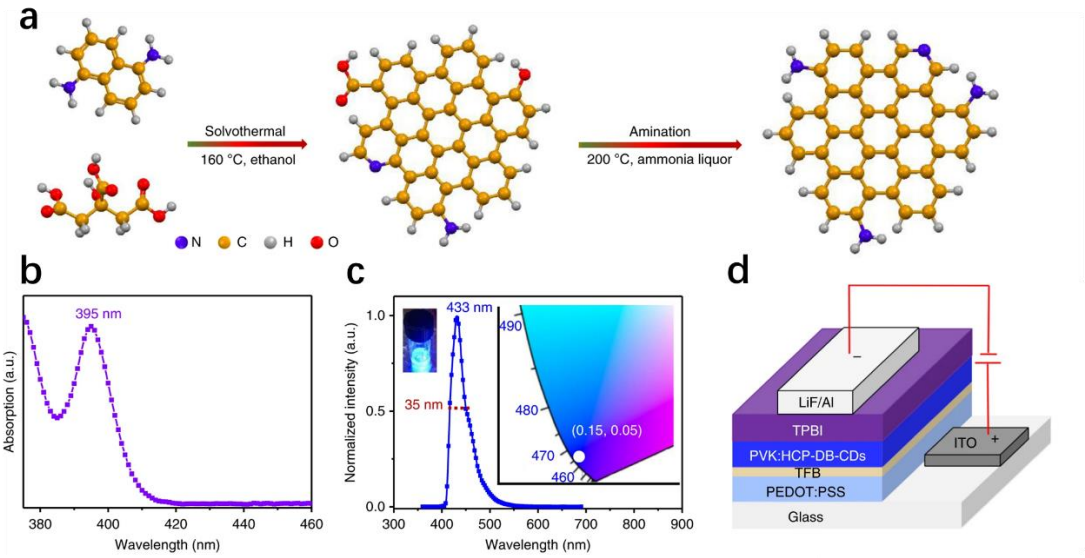

Figure 2.12. a) Amine passivated CDs for efficiency and high color purity emission; b) absorption and c) narrow emission with an FWHM of 35 nm of CDs; the deep-blue emission has a color coordinate of (0.15, 0.05); d) LED device structure. [adapted from reference[110]]

The organic light-emitting diode (OLED) digital display has been considered as a superior alternative to liquid-crystal display because of its extensive color space, high efficiency of operation, and improved contrast [111]. Though tremendous progress has been made regarding the OLED technology, bright narrowband (full-width at half-maximum should be less than 60 nm) has been a great challenge. Therefore, developing novel high-efficiency, non-toxic and high-color-purity materials has been an active topic. CDs are advantageously metal-free and composed of abundant elements. These outstanding features endow CDs with promising opportunities in displays [112-114]. However, CDs suffer from their broad emission (FWHM >80 nm) and insufficient color purity. The issue has been solved by Yuan *et al.* who passivated CDs with amine to eliminate the oxygen-containing functional group [110], as shown in **Fig. 2.12a**. As a result, the surface functionalized CDs based deep-blue LEDs have high color purity and narrow emission (FWHM ≈ 35 nm) (**Fig. 2.12b,c,d**).

Notably, the LEDs have a maximum luminance of 5,240 $cd \cdot m^{-2}$, and the external quantum efficiency (EQE) can reach 4%, significantly outperforming other colloidal semiconductor-based deep-blue LEDs (**Fig. 2.12c**). The superior performance is related to the high exciton binding energy, 150 ± 14 meV, determined by the temperature-dependent PL intensity. The large binding energy can lead to radiative recombination, and the quantum yield is enhanced correspondingly. The surface amination method is demonstrated to achieve high-color-purity CDs, offering a new solution to achieve heavy-metal-free emitters for future flat-panel display applications. Prashant *et al.* also investigated the possibility of applying the waste biomaterial, human hair derived CDs to OLED [113]. The CDs with QY of 87% assembled in the OLED device function as an emitting layer, showing an impressive luminescence of 700 $cd \cdot m^{-2}$. Ever-growing passion has fueled the research of metal-free CDs based OLED [114]. However, CDs are only superior to apply to blue-light OLED, and few trials in other color of OLED have been reported. CDs have been applied to sustainable metal-free carbon-based optoelectronic devices for prospective future smart living.

Solar-driven conversion of CO_2 or water into molecular fuels has been considered an ideal solution to the energy crisis and environmental challenges. Various kinds of inorganic nanocrystals like CdS and TiO_2 have been developed, tested as photocatalysts [23, 26, 34]. However, these materials suffer from containing toxic elements or having limited light absorption of solar energy. Since its early development, non-toxic CDs have been modified and applied to photocatalytic energy conversion reactions, including CO_2 reduction and water splitting [115, 116]. The CD-based photocatalysts can be classified into two types: pure CD photocatalysts and CD-based composite photocatalysts.

For pure CDs photocatalysts without co-catalysts, the photocatalytic activity is usually far beyond satisfactory. Generally, doping CDs with other elements, such as N, O, S and P, is an effective method to enhance photocatalytic activity [117-119]. Nitrogen element has been the first choice to doped into CDs. The mechanism interpretation has also been a hot topic. A typical example is that Bhattacharyya *et al.* found that the PL quantum yield and photocatalytic activity are related to nitrogen position [120]. The CDs doped with pyridinic nitrogen had significantly enhanced photocatalytic activity, as showed in **Fig. 2.13**. Interestingly, the CDs with graphitic/pyrrolic nitrogen positions are increasingly emissive and have a relatively large PL quantum yield. Therefore, there is an anti-correlation between the amount of graphitic nitrogen and photocatalytic activity. Phosphorus atom is also a good choice, which can also work as an n-type impurity after introducing CDs. Meanwhile, as the atom size is larger than that of a carbon atom, it can induce substitutional defects and the optical properties can be modified accordingly [121]. For example, a redshift from 420 to 470 nm in the emission is found in the phosphorus-doped CDs.

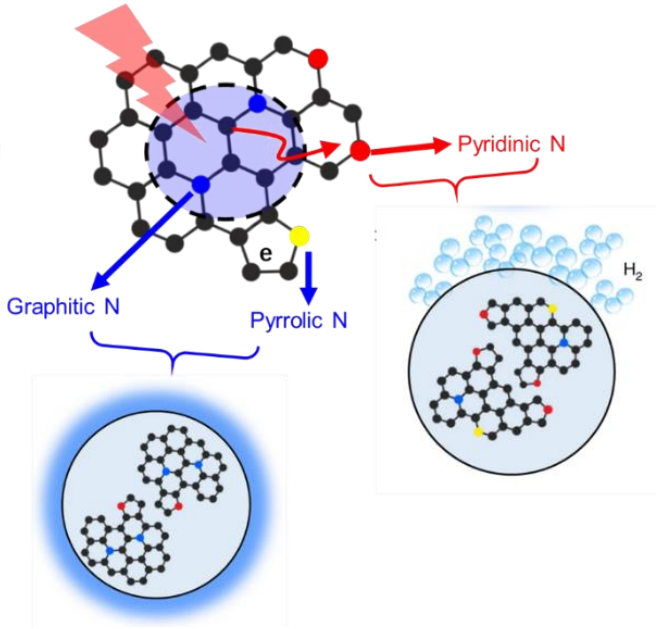

Figure 2.13. CDs with two nitrogen positions, graphitic nitrogen and pyrrolic nitrogen-containing CDs are beneficial to emission, while pyridinic nitrogen-containing CDs are beneficial to photocatalytic H_2. [adapted from reference [120]]

For CD-based composite photocatalysts, CDs generally function as sensitizers to enhance light absorption, decompose peroxide, or store electrons for reduction reactions and efficiently improve charge separations [122]. A typical example is CDs modified TiO_2 reported by Yu *et al* [123]. The chemical bonds on the surface between CDs and TiO_2 can enhance electron transfer from CDs to the conduction band of TiO_2. After introducing CDs, the composite has an extended absorption range, and the lifetime is also prolonged due to efficient charge separation can lead to enhanced photocatalytic activity. The composite exhibits 4 times higher hydrogen generation rate than pure TiO_2. The composite also shows photocatalytic activity even in the visible range where TiO_2 has no absorption. The photocatalytic efficiency can be boosted significantly in a metal-free CDs/C_3N_4 composite photocatalyst reported by Kang *et al*. The composite has the highest catalytic performance so far reported and the overall solar energy conversion efficiency reaches surprisingly 2.0% [124].

In this thesis, metal-free, functional CDs have been synthesized and investigated extensively and further tested in the application to photocatalytic hydrogen generation.

2.3 Photophysical process of organic molecules

Since CDs are composed of polycyclic aromatic hydrocarbon, herein, organic photophysics are needed to understand and interpret CDs' optical properties. Therefore, the section will give a short introduction to organic photophysics required to understand and interpret the complicated carrier dynamics in CDs.

2.3.1 Absorption

Same as inorganic semiconductors, photons absorption will promote electrons to an excited state in organic molecules. In terms of quantum mechanics, the molecule's Hamiltonian is added with a term corresponding to the absorption process. Assuming a perturbation term H' is added to the original Hamiltonian H_0 to give $H = H_0 + H'$, it is reasonable to assume that the wavefunction and eigenvalues change only a tiny amount. A suitable operator is the electronic dipole operator e**r**. Most importantly, the transition rate k_{if} between the initial Ψ_i and final state Ψ_f can be derived from Fermi's golden rule (**Eq 2.6**).

$$\boldsymbol{k_{if}} = \frac{\mathbf{2}\pi}{\hbar}|\langle \Psi_{\boldsymbol{f}}|\boldsymbol{H'}|\Psi_{\boldsymbol{i}}\rangle|^{\mathbf{2}}\cdot\rho \tag{2.6}$$

wherein ρ is the density of final states. The molecular wavefunction Ψ can be approximated by the product of many-electron electronic wavefunction Ψ_{el}, the spin wavefunction Ψ_{spin} and the vibrational wavefunction Ψ_{vib} (**Eq.2.7**). The equation **Eq 2.6** can be transformed into **Eq.2.8** after inserting the wavefunction and dipole operator**.**

$$\Psi = \Psi_{\boldsymbol{el}} \cdot \Psi_{\boldsymbol{spin}} \cdot \Psi_{\boldsymbol{vib}} \tag{2.7}$$

$$k_{if} = \frac{2\pi}{\hbar}|\langle \Psi_{el,f}\,\Psi_{vib,f}\,\Psi_{spin,f}|\mathbf{er}|\,\Psi_{el,i}\,\Psi_{vib,i}\,\Psi_{spin,i}\rangle|^2\rho \tag{2.8}$$

The incident light, an electromagnetic wave with a time-dependent electrical dipole, forces the electrons to move in resonance, while the heavy nuclei cannot respond simultaneously. That is also the definition of the Born-Oppenheimer approximation [125]. Meanwhile, the spins are kept constant, as the time-dependent magnetic field of light is too small to make a difference. Therefore, the dipole operator only acts on the electronic wavefunction. The vibrational wavefunction Ψ_{vib} and the spin wavefunction Ψ_{spin} can be treated like constant factors. The equation can be transformed into **Eq 2.9**

$$\boldsymbol{k_{if}} = \frac{\mathbf{2}\pi}{\hbar}\rho\left|\langle \Psi_{\boldsymbol{el,f}}\left|\mathbf{er}\right|\Psi_{\boldsymbol{el,i}}\rangle\right|^{\mathbf{2}}\cdot\left|\langle \Psi_{\boldsymbol{vib,f}}\right|\left|\Psi_{\boldsymbol{vib,i}}\rangle\right|^{\mathbf{2}}\cdot\left|\langle \Psi_{\boldsymbol{spin,f}}\right|\left|\Psi_{\boldsymbol{spin,i}}\rangle\right|^{\mathbf{2}} \tag{2.9}$$

First, let us discuss the term $\langle \Psi_{el,f}|\boldsymbol{er}|\,\Psi_{el,i}\rangle$. If the integral value is zero, the transition is dipole forbidden, otherwise, it is dipole-allowed or partially allowed. Generally, rates between orbitals in the same region of the molecules (e.g., $\pi\rightarrow\pi^*$ transitions) will be larger

than those between orbitals located in different spaces (e.g., n-π transition, charge-transfer transitions). The absorption strength can also be used to identify the kinds of transitions, as each transition type has a different oscillator strength f. The oscillator strength is given by **Eq 2.10**

$$\boldsymbol{f} = \frac{\mathbf{4.39\times10^{-9}}}{\boldsymbol{n_0}} \int \varepsilon(\nu)\mathbf{d}\nu \tag{2.10}$$

wherein $\varepsilon(\nu)$ is the molar decadic extinction coefficient at a specific wavenumber ν, and n_0 is the refractive index of the surrounding medium. The oscillator strength represents the absorption band's total area, and the maximum value is 1. Generally, the oscillator strength of singlet transitions with a $\pi\rightarrow\pi^*$ character is in the range of 10^{-2} to 1, while that of singlet transitions with a charge transfer character (including $n\rightarrow\pi^*$ transition and charge transfer transitions) is 10^{-5} to 10^{-3}. For forbidden transition, such as the transition from S_0 to T_1, the oscillator strength can even be more negligible (from 10^{-9} to 10^{-4}) due to the difference in spin multiplicity. The value of triplet transition also depends on whether heavy atoms are incorporated. These values are of great importance to identify the transition type of the peaks in the absorption spectrum.

The electronic wavefunction decides the transition intensity, while the spectra shape of both absorption and emission is decided by the vibrational wavefunction $\langle \Psi_{vib,f} | \Psi_{vib,i} \rangle$. The integral is an expression of the Franck-Condon Principle. The principle states that an electronic transition is most probable when the initial and final vibrational state wavefunctions overlap most [126]. When a photon is absorbed, an electron is lifted from the ground state's zeroth vibrational level to the *m*th vibrational level of an electronically excited state. The intensity can be calculated by the square of the overlap of vibrational wavefunctions, $|\langle \Psi_{vib,f} | \Psi_{vib,i} \rangle|^2$, also called Franck-Condon-overlap-factor. The spin-wavefunction Ψ_{spin} (α_i, β_i), the integral value $\langle \Psi_{spin,f} | \Psi_{spin,i} \rangle$, is the last term to determine the transition rate. The integral only has two values, 1 or 0. If the initial and final state spins are equal, the value is 1, otherwise 0 if they are different. Thus, transitions between singlet states or between triplet states, such as $S_0\rightarrow S_1$ or $T_1\rightarrow T_n$ are spin-allowed, yet transitions within different multiplicities, such as $T_1\rightarrow S_0$, are spin-forbidden.

Although the shape, position and intensity of absorption is intrinsically determined by the Fermi's golden rule, the environmental effects, especially the solvent polarity and hydrogen bonding, can also affect the absorption profoundly. It is important to investigate the effects brought by hydrogen bonding in water as the thesis focuses on photocatalytic water splitting. The hydrogen bonding can occur both in the ground state and excited state. The hydrogen bonding in the excited state, or photoinduced protonation, will be discussed in **Section 2.3.4**. If hydrogen bonding between the solvent and molecules with $^1(n, \pi^*)$ states as the lowest singlet state (e.g., aldehydes and ketones) is formed in the ground state, the absorption

spectrum will blueshift. The blueshift is due to the decrease of the molecule's dipole moment after hydrogen bond formation [127]. Generally, the charge distribution of aldehydes/ketones is weighed toward oxygen atom due to the presence of lone pair electrons. The lone pair electrons are eliminated in the excited state, resulting in a smaller dipole moment. Given the dielectric effect, the molecule in the ground state will be more stabilized than the excited state. Therefore, a blueshift in the absorption spectra can be noticed. **Table 2.1** shows that the energy needed for the $n \rightarrow \pi^*$ transition in acetone is growing larger in a stronger protic solvent. In contrast, the absorption due to $\pi \rightarrow \pi^*$ transition would not be affected by hydrogen bonding [128]. Hydrogen bonding induced blueshift has been an indicator to identity $n \rightarrow \pi^*$ transitions in absorption spectrum [129].

Table 2.1 The effects of hydrogen bonding on the n→π* transition in acetone mixed in different solvents [130] .

Solvent	Hexane	Chloroform	Ethanol	Methanol	Water
λ_{max} (nm)	279	277	272	270	265

2.3.2 Radiative recombination

After absorbing photons, the electronically excited species can be regarded as "hot" species with respect to the surrounding ground-state molecules. The excited molecules will dissipate energy through radiative and nonradiative relaxation, which is displayed in **Fig 2.14**. The Jablonski diagram has been widely used to visualize the possible photophysical processes. After being lifted to the excited state, the electron would relax to S_1 via internal conversion, or to T_1 via intersystem crossing. The electron and hole pair can further recombine radiatively or nonradiatively. Depending on whether the transition is spin allowed or spin forbidden, the radiative recombination can be divided into fluorescence or phosphorescence. Similarly, nonradiative transitions between states of the same multiplicity are termed internal conversion, while intersystem crossing (ISC) refers to the transition between states of a different multiplicity [131].

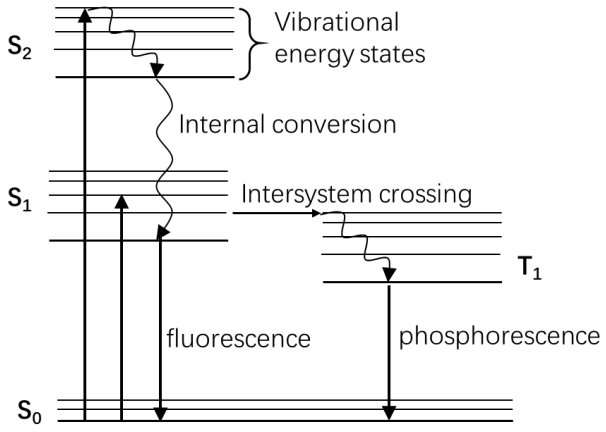

Figure 2.14 A typical Jablonski diagram.

The emission from the singlet state, in most cases S_1, relaxing to the ground state S_0 is called fluorescence. The fluorescence emission is, generally, not dependent on the excitation wavelength. The emission of a photon is a spontaneous process. However, the molecules can stay in the singlet states for a specific time, from a few picoseconds to several hundred nanoseconds, depending on the medium and the intrinsic properties of the molecule. Emission is a spontaneous process. Each excited molecule has the same probability of emitting throughout its lifetime. It means that some fluorophores can emit at an earlier time, while the other at a later time. The process can be depicted by an exponential decay in **Eq 2.11**,

$$\boldsymbol{n(t) = n_0 exp(-t/\tau)} \tag{2.11}$$

wherein τ is the lifetime. If all these photons could be collected and counted, the diagram of arrival times against the photon number would present the intensity decay. The lifetime can be determined from the photon counting. A crucial physical concept in photophysics is quantum yield Φ, defined as the fraction of the photons used for undergoing a specific process. A kinetic form can also be expressed where the rate of a specific pathway is compared to the total decay rate of all pathways, as shown in **Fig. 2.12**. The general expression is as follows,

$$\Phi = \frac{\boldsymbol{k_0}}{\boldsymbol{k_0 + \sum k_i}} = \boldsymbol{k_0} \cdot \tau \tag{2.12}$$

wherein Φ is the efficiency of forming a emitting state, k_0 is the rate constant of the emission, and $\sum k_i$ is the sum of all the nonradiative pathways. The luminescent lifetime τ depends mainly on the value of $\sum k_i$ compared to that of k_0. The latter would not change much under different conditions, while $\sum k_i$ can be significantly changed by experimental conditions. A general method is to minimize $\sum k_i$ by cooling the sample down to a low temperature or disperse the sample into a polymer. Generally, the decreasing temperature would increase in the fluorescence quantum yield and lifetime because the nonradiative deactivations related to thermal agitation are significantly suppressed [132].

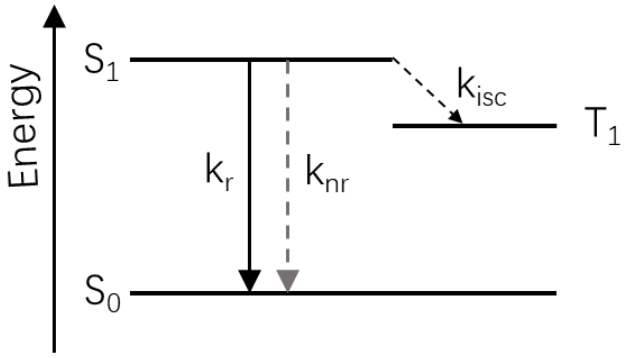

Figure 2.15. A typical state diagram indicates the radiative and nonradiative decay from S_1 to S_0 with rates k_r and k_{nr} in a general fashion.

As CDs are composed polycyclic aromatic hydrocarbon, the relaxation process of aromatic carbonyl compounds is also discussed. The decay dynamics is strongly influenced by the existence of the low-lying (n, π^*) singlet state. Because the n orbital and π orbital is orthogonal, their overlap is negligible. Therefore, the absorption coefficient of $n \rightarrow \pi^*$ transition is much smaller than $\pi \rightarrow \pi^*$ transition. Consequently, the radiative decay of the lowest singlet state with a (n, π^*) configuration is generally much slower than that one with a (π, π^*) configuration. In general case, the fluorescence decay of a S_1 (n, π^*) state is too slow to compete with nonradiative decay. Therefore, molecules with a lowest singlet state $S_1(n, \pi^*)$ always possess a small fluorescence quantum yield, in contrast to the case with $S_1(\pi, \pi^*)$ which generally has a larger quantum yield [128].

The emission from the lowest triplet state (T_1) is called phosphorescence. As the transition $T_1 \rightarrow S_0$ is forbidden, the related radiative constant due to spin-orbit coupling is quite small compared to fluorescence. The resulting lifetime is usually longer than 1 μs, which is also the starting point to explore the possibility of applying phosphorescent organic materials to photocatalytic hydrogen generation. The results are illustrated in **Chapter 6**. Due to the small radiative constant of triplet emission, a faster nonradiative process and spontaneous emission can prevail, and generally, phosphorescence is barely observed at room temperature.

2.3.3 Nonradiative transition

Non-resonant light absorption usually generates an excited state at a high vibrational level, followed by fast dissipation of the vibrational energy to the surrounding environment. The nonradiative relaxation can occur between two different electronic states as well as in one electronic state. As the name "nonradiative" suggests, there is no photon emitting. The rate constant of nonradiative relaxation can also be calculated by the Fermi's golden rule, based on perturbation theory [133],

$$\boldsymbol{k_{nr}} = \frac{\boldsymbol{2\pi}}{\hbar}|\langle \Psi_{\boldsymbol{f}}\boldsymbol{S_f}|\boldsymbol{H'}|\,\Psi_{\boldsymbol{i}}\boldsymbol{S_i}\rangle \sum_{\boldsymbol{n}}\langle\, \Psi_{\boldsymbol{vib,f,n}}|\,\Psi_{\boldsymbol{vib,i,0}}\rangle^{\boldsymbol{2}} \tag{2.13}$$

Let us discuss the internal conversion first. The relevant electronic matrix element is $\langle \Phi_f|H_{IC}|\Phi_i\rangle$, where H_{IC} is the nuclear kinetic energy operator. It is termed for an isoenergetic transition from the zeroth vibrational level of the higher state to the *m*th vibrational level of the lower energy state. Internal conversion also includes the case where vibrational relaxation from the first singlet state into the vibrationally equilibrated ground state ($S_1 \rightarrow S_0$). The electrons' lifetime at a higher excited state is usually very short, and their corresponding quantum yields of emission are tiny.

Generally, the nonradiative transition from S_1 to the ground state (S_0) is a much slower process than the internal conversion ($S_n \rightarrow S_1$). The fast internal conversion ends typically at the S_1 state and does not continue to relax to the ground state S_0. The energy gap law states that the probability of nonradiative transition decreases exponentially with the two states' energy gap. In the zero-order where no surface crossing between S_1 and S_0, the internal conversion starting from S_1 must occur via the "Franck-Condon forbidden" mechanism. Specifically, the nuclei must change dramatically in position and momentum to increase the overlap of vibrational wavefunctions of both states [134, 135]. In this case, the Franck-Condon factor will limit the rate of the $S_1 \rightarrow S_0$ internal conversion. The factor is found sensitive to the energy gap, ΔE, between the zero-point vibrational levels of the states. The k_{ic} can be estimated as follows,

$$\boldsymbol{k_{ic}} \sim \boldsymbol{10^{13}exp}(-\alpha \boldsymbol{\Delta E}) \tag{2.14}$$

wherein α is a constant. It implies that a larger energy gap will result in poorer vibrational overlap caused by the higher vibrational quantum number of the lower state's isoenergetic level [136, 137]. Generally, the internal conversion between S_1 and S_0 is negligible if bandgap is larger than 2 eV.

In terms of intersystem crossing, the matrix element for the coupling energy is $\langle \Psi_f|H_{so}|\,\Psi_i\rangle$, where H_{so} is the operator for spin-orbit coupling. The spin-orbit coupling can be regarded as the interaction between the magnetic moment (μ_S) resulting from the electron's spin angular momentum (S) and the magnetic moment (μ_L) resulting from the electron's orbital

angular momentum (L). The magnetic coupling strength is decided by the orientation, magnitude, and distance of the magnetic moments. The operator H_{so} has the form of **Eq 2.15**, where ς_{SO} is the spin-orbit coupling constant and related to the nuclear charge.

$$\boldsymbol{H_{so}}=\varsigma_{\boldsymbol{SO}}\cdot\boldsymbol{S}\cdot\boldsymbol{L}\ \sim\ \varsigma_{\boldsymbol{SO}}\cdot\mu_{\boldsymbol{S}}\cdot\mu_{\boldsymbol{L}} \tag{2.15}$$

$$E_{SO}=\langle\Psi_f|H_{so}|\Psi_i\rangle=\langle\Psi_f|\varsigma_{SO}\cdot S\cdot L|\Psi_i\rangle\sim\langle\Psi_f|\varsigma_{SO}\cdot\mu_S\cdot\mu_L|\Psi_i\rangle \tag{2.16}$$

The magnitude of spin-orbit coupling (E_{SO}) is given by a matrix element that has the form of **Eq 2.16**. For organic molecules containing only "light" atoms (e.g., H, C, O, and N), the value of the spin-orbit coupling constant ς_{SO} is typically small (~0.01-0.1 kcal·mol^{-1}). However, in the presence of "heavy" atoms (e.g., Br or Pb), the magnitude of ς_{SO} can be large and even exceed vibrational energies. For atoms with nuclear charge Z, the strength of spin-orbit coupling is proportional to Z^4. Therefore, the presence of heavy atoms in molecules or solvent is beneficial to phosphorescence, which is termed as the "heavy atom effect". In molecules, the spin-orbit coupling is a local effect depending on the distance between the electron and the heavy atom [138].

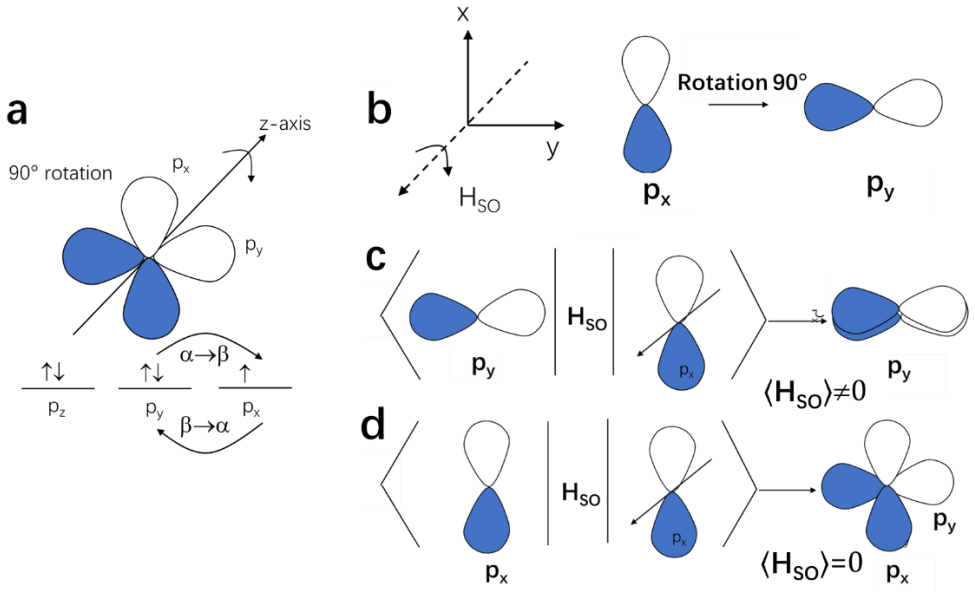

Figure 2.17 (a) Scheme of the effect of H_{SO} on the orientation of a p orbital; (b)(c)(d) Visualization of the matrix element for spin-orbit coupling.

Here an example illustrates how the spin-orbit coupling works. Suppose there is an electron with one unit of orbital angular momentum ($\hbar$) in a p orbital. If the spin changes its orientation by one unit of angular momentum (β(-1/2) →α(+1/2) or α(+1/2)→β(-1/2)), the p orbital has to change precisely one unit of angular momentum, as the angular momentum conservation must be fulfilled. One unit of orbital angular momentum can be achieved by the orbital rotation of 90° around the arbitrary *z*-axis (**Fig 2.17a**). This move is equivalent to rotating and overlap with an adjacent p orbital (in this case, $p_x \rightarrow p_y$). It is the requirement to rotate about an axis in orbital orientation to couple the spin flip that is reflected in the form of the operator H_{so}.

The matrix $\langle \Psi_f | H_{so} | \Psi_i \rangle$ is a direct measure of the magnitude of spin-orbit coupling between the initial state and the final state. The magnitude of matrix will be large if the state Ψ_i "looks like" state Ψ_f. Given the effect brought by the operator H_{so}, the magnitude will be large if Ψ_i overlaps Ψ_f after rotating the wavefunction by 90° (**Fig 2.17b**). Therefore, the spin-orbit coupling will be more effective in inducing transition between orthogonal orbitals, for example n and π orbital (**Fig 2.17c**). It can explain why the ISC quantum yield of triplet formation for carbonyl compounds is nearly unit. However, the value is primarily small for polycyclic aromatic hydrocarbons due to the parallel of the initial state (π) and final state (π) (**Fig 2.17d**).

The singlet states with electronic configurations of (n, π^*) and (π, π^*) are the two low-energy states mainly responsible for the intersystem crossing process for organic molecules. First consider now the intersystem ${}^1(n, \pi^*) \leftrightarrow {}^3(n, \pi^*)$. Since the initial and final states have the same configuration, the previous discussion has shown that the resulting matrix element $\langle \Psi_f | H_{so} | \Psi_i \rangle$ amounts to zero. The same result can also apply to case ${}^1(\pi, \pi^*) \leftrightarrow {}^3(\pi, \pi^*)$ intersystem crossing. Similarly, for the ${}^1(n, \pi^*) \leftrightarrow {}^3(\pi, \pi^*)$ intersystem crossing, the direct product $\Psi_i \times \Psi_f$ is not symmetric, so that this process is allowed.

In summary, the transitions

$${}^1(n, \pi^*) \leftrightarrow {}^3(\pi, \pi^*) \text{ and } {}^3(n, \pi^*) \leftrightarrow {}^1(\pi, \pi^*)$$

are allowed, while transitions

$${}^1(n, \pi^*) \leftrightarrow {}^3(n, \pi^*) \text{ and } {}^3(\pi, \pi^*) \leftrightarrow {}^1(\pi, \pi^*)$$

are forbidden. It is summarized in **Fig. 2.18** where the solid and dash line represents allowed and forbidden transition, respectively.

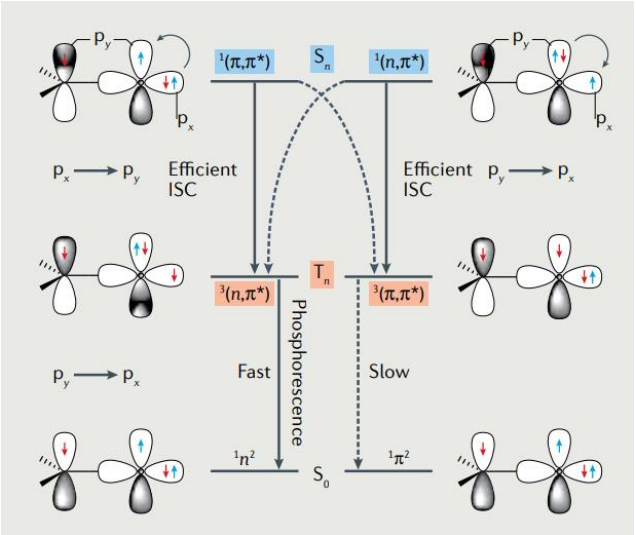

Figure 2.18 Schematic representation of ISC. [adapted from reference [139]]

The intersystem crossing $S_1 \rightarrow T_1$ process can occur either by direct spin-orbit coupling of S_1 to the higher vibrational levels of T_1 or to one of higher states but energy-closer T_n and follow by rapid internal conversion $T_n \rightarrow T_1$. The rate-determining step is the spin-flip,

and the rate constant k_{ST} is in the range 10^7- 10^{11} s^{-1} [131]. The ISC rate also depends on the energy difference between the states and the extent of spin-orbit coupling. Regarding the energy gap dependence of the intersystem crossing rate, the triplet state with energy closer to S_1 has a higher ISC rate than other triplet states with a larger energy difference.

2.3.4 Photobase effects

Organic molecules have unique exceptional photophysics, especially in the excited state, which is hardly found in inorganic materials. Could any organic photophysical property be utilized and improve photocatalytic hydrogen generation? Photobase effect, that is, photoinduced proton transfer is one example. The related work is discussed in detail in **Chapter 4** and **Chapter 5**. The molecule after being excited will have a different bonding situation and the equilibrium geometry is changed as well, as an electron is excited from a bonding orbital to an antibonding orbital. The more difference in the bond length before and after the transition, the more pronouncedly the geometry will be changed. Accordingly, the electron density is redistributed in the excited state. The excited molecules can have different chemical and physical properties against the ground state. One typical example is that the basicity/acidity change after photon absorption [140, 141].

The excited molecules with donor and acceptor groups often possess an intramolecular charge transfer from the donor/nanodomain (π) system to the acceptor. Consequently, the dipole moment in the excited state is generally more prominent than that in the ground state. The acceptors, such as pyridinic nitrogen, have vacant π orbitals that can allocate electrons from the donor/π system. In this way, the acceptor group can have a much stronger affinity to protons due to the extra electron. If the attraction is large enough, it can abstract the proton even from water, leaving OH^- in the solvent, making it more basic. That is the definition of photobase [142, 143]. Similarly, electron transfer occurs from the electron donors, such as the phenolic hydroxyl group, to the π system or an electron acceptor. This results in a weaker affinity to the proton. That is the definition of photoacid [138]. In this way, the proton transfer can be manipulated by light. The difference can be presented by the value change in pK_a, denoting losing or gaining a proton in the excited state. If the pK_a decrease in the excited state (pK_a^*<pK_a) where the asterisk denotes the excited state, the excited molecule tends to dissociate the proton. On the other hand, if the pK_a increases ($pK_a^* > pK_a$), the excited molecule tends to abstract a proton from the solvent [131, 140]. Although the interesting photophysics has been well investigated by optical spectroscopy, few works on the applications of photobase have been reported [144, 145].

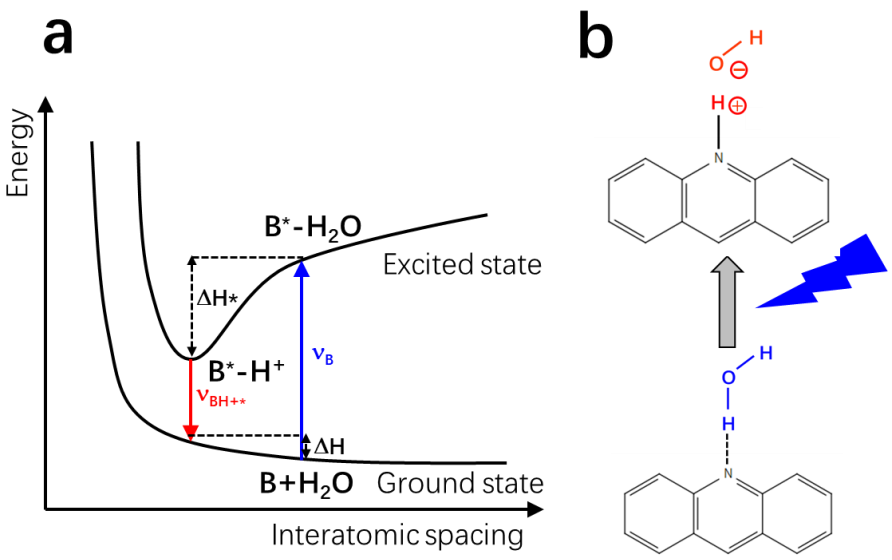

Figure 2.18. a) Scheme potential energy diagram of Förster cycle for proton transfer; b) a model photobase, acridine, in the ground state (deprotonated) and excited state (protonated).

The variation of basicity in the excited state can be explained by this equation (**Eq. 2.17**).

$$\mathbf{B^* + H_2O \leftrightarrow B^* - H^+ + OH^-} \tag{2.17}$$

Upon excitation, B^* is in a high-energy state and tends to evolve into B^*H^+. The protonated species (B^*H^+) can emit photons with a longer wavelength from the non-protonated species. Thus, the molecule in the excited state is a stronger base. Whether a proton transfer will occur in the excited state is decided by its lifetime and energy barriers in the excited potential energy surface [131]. As illustrated in **Fig. 2.18a**, the scheme shows an indirect method of deciding the pK_a^* value in the excited state based on excitation energy change upon protonation and molar enthalpy change, which is called the Förster cycle [146]. The scheme can be illustrated in the equation as follows **Eq. 2.18**

$$\boldsymbol{N_L h \nu_B + \Delta H = N_L h \nu_{BH+} + \Delta H^*} \tag{2.18}$$

Or

$$\boldsymbol{\Delta H^* - \Delta H = N_L (h \nu_B - h \nu_{BH+})} \tag{2.19}$$

wherein ν_B and ν_{BH+} are the frequencies of the lowest absorption bands of B and B^*H^+, respectively, ΔH (ΔH^*) is the molar enthalpy changes in the ground (excited) states, h and N_L are the Planck's constant and the Avogadro number, respectively. The value ΔH can be further approximated by ΔG_0 on the condition that entropy effects can be neglected,

$$\boldsymbol{\Delta G_0 = -RTlnK = -2.303RTpK_a} \tag{2.20}$$

In this way, the equation can be transformed into

$$\boldsymbol{N_L\,(h\nu_B - h\nu_{BH+}) \approx \Delta\Delta H_0 \approx \Delta\Delta G_0 \approx 2.303RT \cdot \Delta pK_a} \qquad (2.21)$$

After the corresponding numerical values are inserted, the concise equation can be derived relating the shift $\Delta\nu$ of LUMO for the lowest singlet or triplet transition with the change in the pK_a value due to protonation at room temperature T=298 K:

$$\boldsymbol{\Delta pK_a = 0.00209(\nu_B - \nu_{BH+})}/\text{cm}^{-1} \qquad (2.22)$$

The value of ΔpK_a is the orders of magnitude the molecule will evolve into stronger photobasic/photoacid in the excited state. It is well established that the electron-donating acidic substituents hydroxyl and amino, become stronger acid while the electron-accepting groups, pyridinic nitrogen, will become stronger bases [138, 143, 147]. **Fig. 2.18b** depicts the status of a typical photobase model, acridine, in the ground state and excited state. In general, for the aromatic-based photobase, the basicity at the lowest singlet state can be enhanced by a factor 10^5~10^{10}. However, the pK_a value of molecules in the triplet states, generally, is comparable to that in the ground state. Excitation into the T_1 state changes the pK_a value in the same direction as excitation into the S_1 state, but generally much less, and the $pK_a(T_1)$ value tends to be closer to $pK_a(S_0)$ than to $pK_a(S_1)$. The relationship can be listed as follows [131].

$$pK_a(S_0) < pK_a(T_1) << pK_a(S_1) \qquad \text{for photobasic}$$

It can be explained by the intramolecular charge transfer contribute to the resonance hybrid constituting S_1, but not T_1, as the Pauli rules keep electrons with parallel spin apart [131].

Table 2.3. pK_a values of several general molecules in the ground/excited state [138]

Molecule	$pK_a(S_0)$	$pK_a(S_1)$	$pK_a(T_1)$
1-naphthoic acid	3.7	10-12	3.8
2-naphthol	9.5	3.1	8.1
2-naphthylamine salts	4.1	-2	3.3
Acridine	5.5	10.6	5.6
Fluorene	20.5	-8.9	5.0
Naphthalene	-4	11.7	-2.5
Phenol	10	4	8.1

Table 2.3 summarizes the pK_a values of the ground state and the lowest singlet and triplet states of several common molecules. After the specific molecule absorbs one photon, the

pK_a values change depending on whether the electronic transition decreases or the basic moiety. The large difference in the pK_a between the ground state and excited state can provide a unique method to manipulate the proton transfer.

What deserves to stress is that the timescale of abstracting a proton in the excited state is from several picoseconds to 100 ps [141, 143]. Thus, compared to the long timescale of proton diffusion (~μs), the photoinduced protonation in photobase is short. That is why photobase molecules are introduced to the photocatalysis system and tested for photocatalytic water splitting. The related works are illustrated in **Chapter 4** and **Chapter 5**.

2.3.5 Room temperature phosphorescence

Generally, fluorescence is spin-allowed with a short lifetime but relatively high quantum yields, while phosphorescence is spin-forbidden with a meagre quantum yield. Researchers have been focusing on extending the lifetime of the singlet states by enhancing charge separation and utilize the electrons in the singlet states in photocatalytic reactions. Interestingly, the triplet states usually have a much longer lifetime (> 1 μs). Here comes the question of whether the triplet states can also be utilized in photocatalytic reactions. The triplet states with a long lifetime are plausible to contribute to the photocatalytic reactions. That is also the topic of **Chapter 6**.

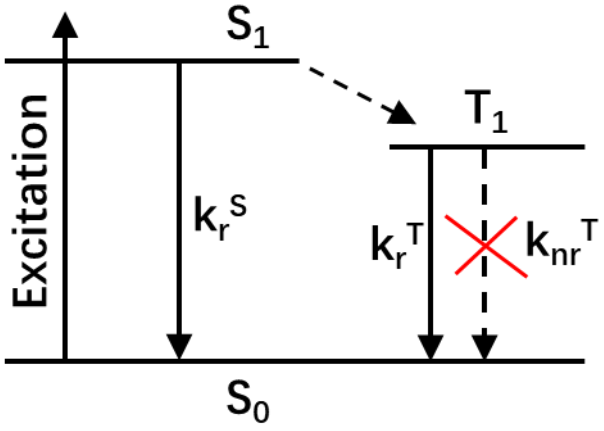

Figure 2.19. Photoluminescence process. The solid line and dashed line represent the radiative and nonradiative relaxation, respectively. The red cross mark is the suppression of the nonradiative relaxation.

Metal-free room-temperature phosphorescent materials are the ideal candidate to investigate whether the triplet states can be used in photocatalysis. Three requirements are needed to achieve room-temperature phosphorescence, based on the **Fig. 2.19**.
(1) spin-flipping by an efficient ISC from singlet state to triplet state,
(2) suppress the nonradiative relaxation,
(3) a slow decay of the radiative recombination.

Regarding the spin-flipping, the intersystem crossing rate is required to be large to compete with the fast fluorescence decay and nonradiative relaxation. The k_{ISC} is related to the singlet-triplet energy difference and the magnitude of effective spin-orbit coupling between S_1 and T_n. Generally, the energy gap between S_1 and T_1 is large, around 0.5-1.0 eV, for polycyclic aromatic hydrocarbon. The large difference is due to exchange energy caused by the same spin states of the unpaired electron [148, 149]. Therefore, a slight overlap of the wavefunctions of the initial state and the final state is the key to achieve a small ΔE_{ST} [150, 151]. The previous section (**Section 2.3.1**) also stresses that the orbitals occupied in the different parts or n orbitals of molecules will have a small wavefunction overlap. Therefore, the general solution is to introduce charge transfer transition (donor-acceptor system) or n orbital.

Efficient ISC occurs when the spin-orbit coupling is large, which has been discussed extensively in **Section 2.3.3**. The ISC is allowed between the singlet state with a configuration $^1(n, \pi^*)$ or $^1(\pi, \pi^*)$ to a triplet state with a configuration $^3(\pi, \pi^*)$ or $^3(n, \pi^*)$, respectively. Thus, n orbital that are orthogonal with π orbital is necessary to achieve a large value of spin-orbit coupling in metal-free organic materials. Another shortcut to promote spin-orbit coupling is to take use of the heavy atom effect. Heavy metal, such as Ir, Pt and Au, is always the first choice.

Moreover, the nonradiative relaxation should be substantially impeded as the emission from the triplet state is a slow process. Generally, the slow phosphorescence process is sensitive to several external perturbations, particular oxygen, and humidity. The most convenient method to minimize the nonradiative decay is to encapsulate samples in a rigid media, typically polymer matrix. Molecular vibrational/rotational motions are restricted mainly to prohibit the nonradiative decay of T_1 due to the interlocking between molecule and polymer. Another possible method is "aggregation-induced emission" where the formation of aggregations interlocks chromophores, and the rotational and twisting motions can also be suppressed. This method mainly applies to non-planar molecules with flexible molecular structures [152].

The triplet state T_1 with different configurations will result in different optical properties. T_1 with a $^3(\pi, \pi^*)$ configuration has an extremely slow decay rate (~1 s^{-1}), because the transition from the antibonding π^* orbital to the bonding π orbital is forbidden (no orbital momentum change). In contrast, T_1 with a $^3(n, \pi^*)$ configuration has a much faster decay rate (>10^2 s^{-1}). Generally, in organic materials, T_1 is rather a hybrid mixture of $^3(n, \pi^*)$ and $^3(\pi, \pi^*)$ configurations than a pure electronic configuration [88]. In other words, the configuration of T_1 can be expressed as $\alpha \cdot {}^3(n, \pi^*)+\beta \cdot {}^3(\pi, \pi^*)$, where $\alpha+\beta=1$. The T_1 state with a hybrid configuration can be further tunable by external parameter, such as temperature and ISC inhibitor. The tunable ratio between the two configurations in T_1 can be used to invesitgate their contributions to photocatalysis. The related work is presented in **Chapter 6**.

Chapter 3 Material synthesis and methods

This chapter will give a detailed protocol of the synthesis of functional CDs, including nitrogen-free, photobasic and phosphorescent CDs, and optical spectroscopy techniques. Structural analysis, including dynamic light scattering and transmission electron microscopy, can give comprehensive information of morphology, size distribution, and materials identification. Steady-state spectroscopy, including UV-vis spectrophotometer and photoluminescence spectrometer, can be used to identify the photobase effect. Optical spectroscopy with higher time-resolution is employed to gain a better understanding of the related photophysical properties in the excited states. Time-resolved spectroscopy can give information of the relaxation process. Transient absorption spectroscopy with femtosecond time resolution is employed to calculate the protonation timescale and study the carrier dynamics. Meanwhile, the introduction to the apparatus to identify and quantify the photocatalytic product hydrogen, that is, gas chromatography, is also included.

3.1 Synthesis of CDs

The metal-free functional CDs in this thesis are all synthesized from hydrothermal method. The term “hydrothermal” generally refers to heterogeneous reactions in water or organic solvents under both high temperature and high pressure to ensure that precursors dissolve and react more efficiently [153]. Thus, the hydrothermal synthesis can be defined as reactions occurring under an environment where high temperature and high pressure (>100 ^{o}C, >1 atm) in a sealed pressure vessel. The hydrothermal technique has been widely employed in the last two decades, but not confined to synthesize monodispersed nanostructures and crystal growth [154]. Thus, it has become a powerful tool to controllably grow various inorganic compounds and raw materials for a wide variety of technological applications.

Regarding CDs synthesis various small organic molecules or polymers are generally selected as precursors and are added to an autoclave for hydrothermal treatment. Due to the high temperature and high pressure, the precursors react, decompose and carbonize [155]. The carbon core is built up during the hydrothermal process while some elements are lost in small molecules (CO_2, CO, H_2O) to increase the conjugation length [156].

Carbon dots are usually a mixture of a variety of carbon-based molecules containing elements of C, H, O and sometimes N. In this thesis, three types of CDs have been synthesized: nitrogen-free CDs, photobasic CDs and phosphorescent CDs. Previous reports show that the N dopants at different locations in the nitrogen-containing CDs could lead to different electronic properties [120].

3.1.1 Nitrogen-free CDs

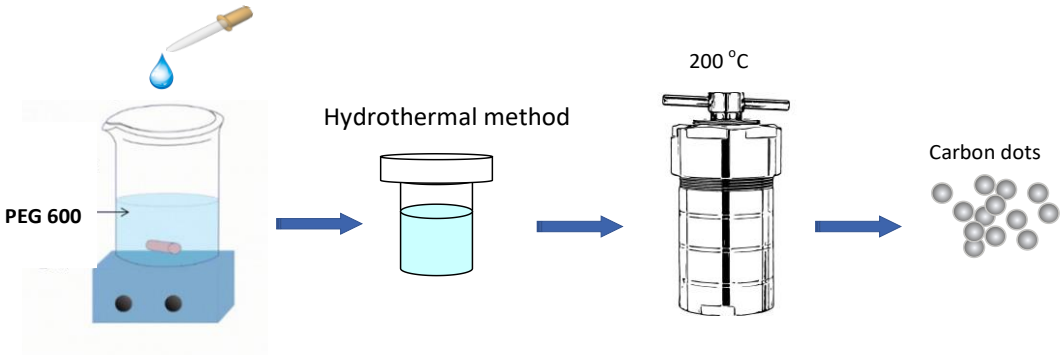

Figure 3.1 Scheme of the hydrothermal method for the synthesis of nitrogen-free CDs for photocatalytic water splitting. PEG is short for Polyethylene glycol.

Polyethylene glycol 600 (PEG 600) was selected as the precursor of metal-free and nitrogen-free CDs. The CDs were synthesized by a straightforward hydrothermal method, as shown in **Fig. 3.1**. Briefly, 318 mg of wax-like PEG 600 was dispersed in 10 mL ethanol

in the presence of vigorous agitation. Afterwards, the transparent solution was further transferred into a 15 mL autoclave held at 200 °C for two hours and cooled down naturally to room temperature. The resulting solution was further purified by a 0.28 μm PVDF (polyvinylidene fluoride) syringe filter to remove the unreacted precursor, and was subject to high centrifugation (5000 rpm) for 5 min. Only the solution in the upper layer was taken for further characterizations. Finally, the solvent, ethanol, was removed by N_2 flow and the sample was redispersed in water prior to the measurements of optical properties and evaluation of photocatalytic activity, as the optical properties of organic materials can be changed dramatically by solvents. The related work is represented in **Chapter 4**.

The CD/acridine hybrid was prepared by two methods. In the first method, the nitrogen-free CDs were synthesized, solvent removed, and mixed with an aqueous saturated acridine solution. Acridine molecule is supposed to locate around the CDs surface. In the second method, acridine was mixed with the polyethylene glycol prior to synthesis. During the polymer carbonization process, acridine molecules can assembly into the CDs structure either as free molecules or incorporated into the N-heterocyclic structure.

3.1.2 Photobasic CDs

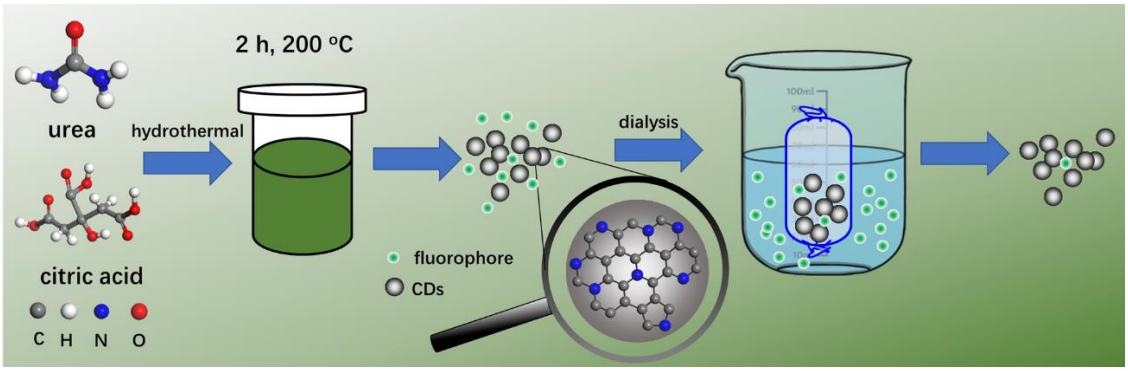

Figure 3.2 Synthetic scheme of photobasic CDs for photocatalytic water splitting.

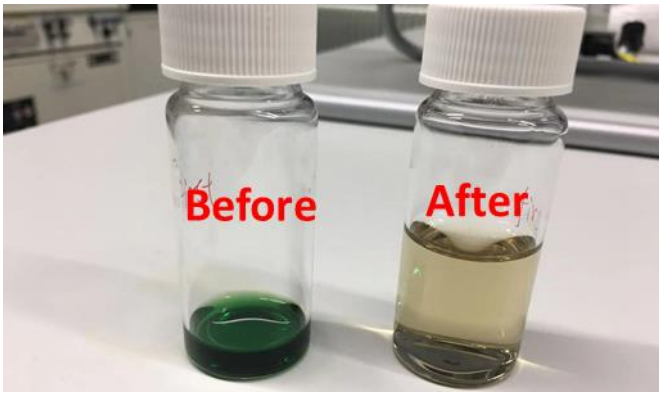

Figure 3.3 Image of CDs solution before (left) and after (right) dialysis.

The synthetic procedure of the photobasic CDs was slightly modified based on a published work by Kasprzyk *et al* [157] where citric acid and urea are selected as the precursors. **Fig. 3.2** is the corresponding synthetic scheme. Typically, 0.385 g of citric acid and 1.3 g of urea

were dissolved and mixed in 10 mL distilled water. Afterwards, the transparent solution was further transferred into a 15 mL autoclave held at 200 °C for two hours and cooled down naturally to room temperature. The resulting dark green solution contained both CDs and small fluorophore molecules as revealed in our group's previous work [158]. To remove the small fluorophore molecules and remaining unreacted precursors, the mixtures have been purified by a 1000 Da dialysis bag for 24 hours until the solution became yellowish. The small molecules would pass through the membrane and get removed, while the relatively large CDs will remain in the dialysis bag. The comparison is shown in **Fig. 3.3** where the left and the right image is the initial solution and purified solution, respectively. The solvent, water, was further removed by flowing N_2 and the sample was redispersed in acetonitrile for subsequent characterizations. The related work is represented in **Chapter 5**.

3.1.3 Phosphorescent CDs

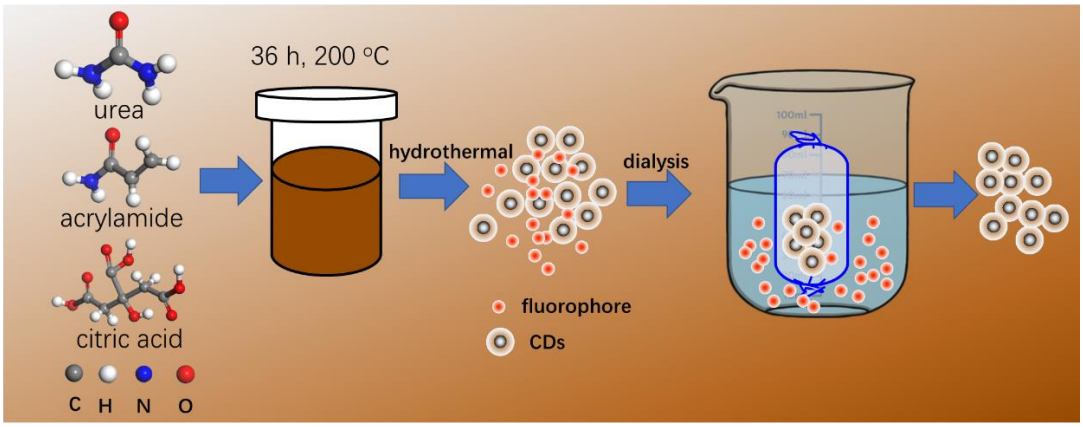

Figure 3.4 A schematic of the synthetic procedure of phosphorescent CDs.

The synthesis of the phosphorescent CDs is based on a slightly modified procedure reported by Kang *et al*. [159], as shown in **Fig. 3.4**. The experimental procedure is similar to that of photobasic CDs. Typically, 0.5 g of citric acid, 4 g of urea, and 4 g of acrylamide were mixed in 30 mL of deionized water in the presence of agitation. The obtained uniform solution was transferred into a 40 mL Teflon-lined stainless-steel autoclave. It was heated at 200 °C for 36 h under static conditions and cooled to room temperature naturally. The resulting dark brown solution was first purified by a 0.28 μm PVDF syringe filter to remove large, aggregated particles. As the phosphorescence can be efficiently quenched by impurities or other impurities, the unreacted precursors in the solution must be removed. The purified product was further purified using a 1000 Da dialysis bag. Accordingly, small molecules (precursors) and fluorophores would pass through the dialysis bag and got removed. As a result, only CDs with relatively large size remain in the dialysis bag. Eventually, the purified light brown solution dried overnight in the oven (70 °C), and CDs powder was obtained for further characterization. The related work is represented in **Chapter 6**.

3.2 Structural analysis

In this part, the size of CDs and size distribution are investigated by high-resolution transmission electron microscopy (TEM) and dynamic light scattering (DLS).

3.2.1 Transmission electron microscopy (TEM)

As the size of CDs is generally less than 5 nm, it is beyond the scope of ordinary microscopy. However, high-resolution transmission electron microscopy (HRTEM) can be used to investigate the transmission of ultra-small specimens to characterize the morphology and size. A concise introduction to the main principles of electron microscopy is given as follows. The optical ray diagram is shown in **Fig. 3.5**. If a sample with lattice distance d is irradiated by an electron beam with wavelength λ, the diffracted waves will be directed with specific angles 2θ. The Bragg condition is satisfied in this situation.

$$2d\sin\theta = \lambda \tag{3.1}$$

The diffraction spots resulting from the diffracted waves are on the back focal plane. With the electron lenses, the diffraction spots can be projected on a screen forming a diffraction pattern. In addition, an electron microscope image can also be formed on the image plane where the transmitted beam and diffracted beams interfere. By adjusting the focal lengths of the electron lenses, both the electron microscope images and diffraction patterns can be obtained.

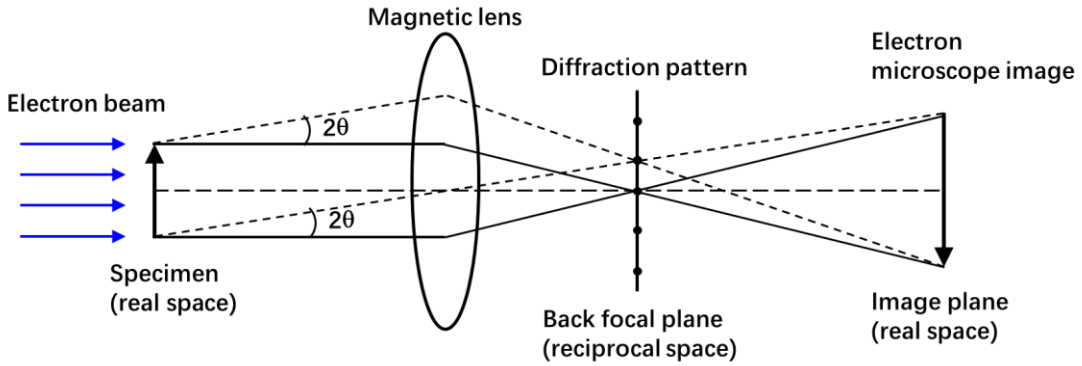

Figure 3.5 Scheme of the principle of the imaging process in a transmission electron microscope.

In this thesis, high-resolution images were recorded with a Titan 80-300 with an accelerating voltage of 300 kV. A resolution up to 0.2 nm can be achieved. Dr. Markus Döblinger performed all HRTEM related measurements at the chair of Prof. Dr. Thomas Bein.

The morphology and size distributions of the nitrogen-free CDs and phosphorescent CDs were characterized by a high-resolution transmission electron microscope. Regarding the

nitrogen-free CDs, HRTEM images show that their size is mainly around 2 nm, ranging from 1.0-3.0 nm (**Fig. 3.6**). Meanwhile, the CDs have a crystalline structure.

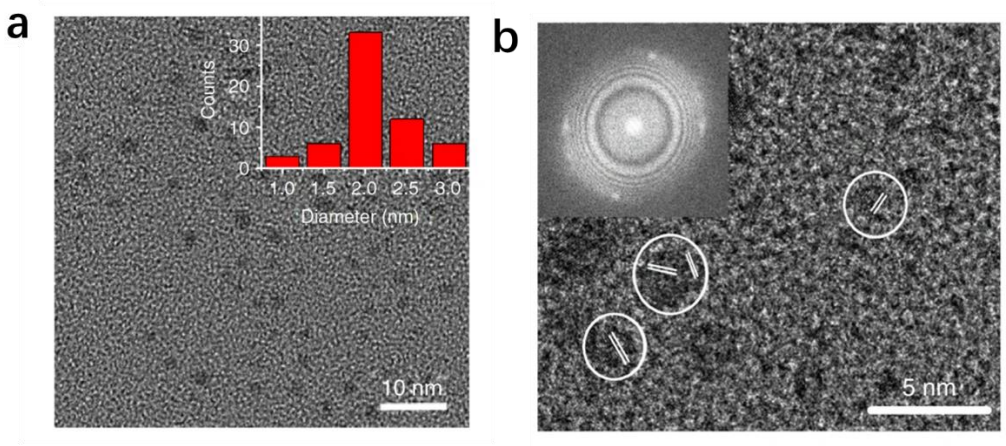

Figure 3.6 a) TEM image of nitrogen-free CDs; b) HRTEM image of nitrogen-free CDs; Insets are the size distribution and FFT image in (a) and (b), respectively.

As shown in **Fig. 3.7**, the size distribution of the phosphorescent CDs is mainly in the range of 2-3 nm and CDs have a crystalline structure.

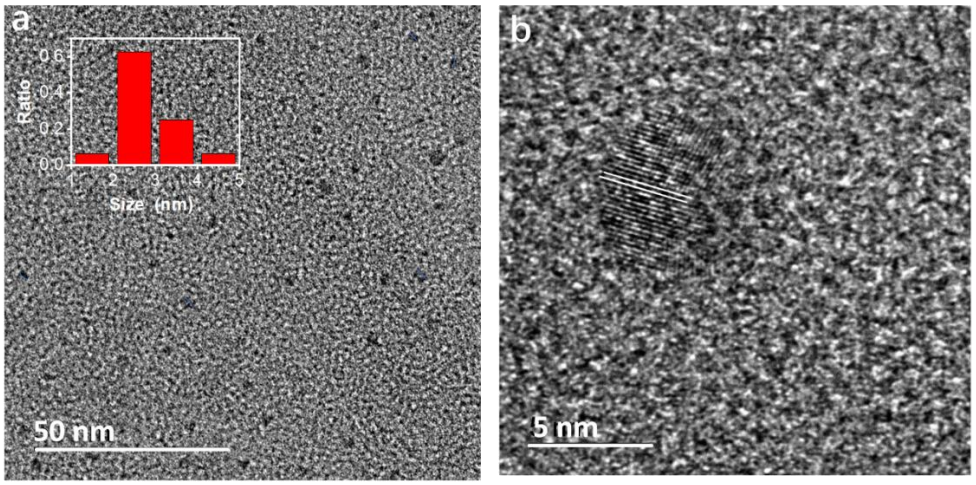

Figure 3.7. a) TEM image of phosphorescent CDs, and the inset is the size distribution. b) HR-TEM image of CDs.

3.2.2 Dynamic light scattering (DLS)

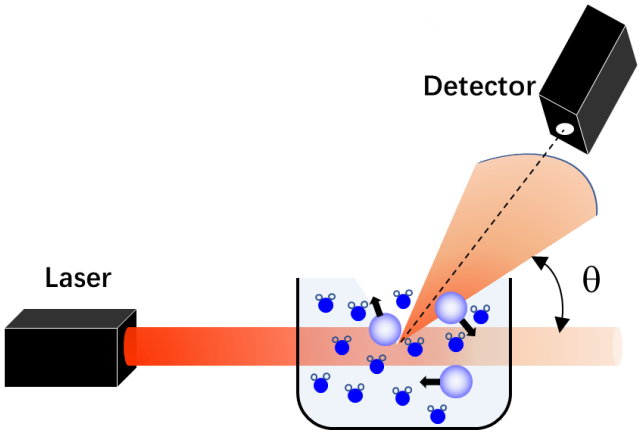

Figure. 3.8 Basic setup of the dynamic light scattering instrument.

Dynamic light scattering (DLS) has been acknowledged as a well-established, non-invasive tool for particle size analysis in solution [160]. The theory of DLS is based on the principle of Brownian motion. The principle states that the particles have collisions with the solvent molecules moving all the time randomly in all directions, as shown in **Fig. 3.8**. The particles undergoing Brownian motion will cause the laser light to be scattered at different intensities, and the distances between particles are also changing with time [161]. Therefore, the particle size and size distribution can be yielded from the analysis of intensity fluctuations with the Stokes-Einstein equation **Eq 3.2**.

$$\boldsymbol{D = \frac{k_B T}{6\pi\eta R_H}} \tag{3.2}$$

wherein D is the translational diffusion coefficient and can also be interpreted as "the speed of the particle"; η and R_H are the dynamics viscosity and hydrodynamic radius, respectively. The basic setup of a DLS instrument includes a monochromatic light source, usually a laser, and a detector. The incident laser will be scattered by the particle in all directions, and the time-dependent scattered laser light will be collected by a detector.

In this work, DLS from Malvern Zetasizer Nano has been applied to investigate the size distribution of CDs. The particle size distribution of the nitrogen-free CDs obtained from DLS is shown in **Fig. 3.9** where it indicates that CDs have dominate size around 2 nm, consistent with the TEM results. The larger size around 50 nm may be caused by aggregation.

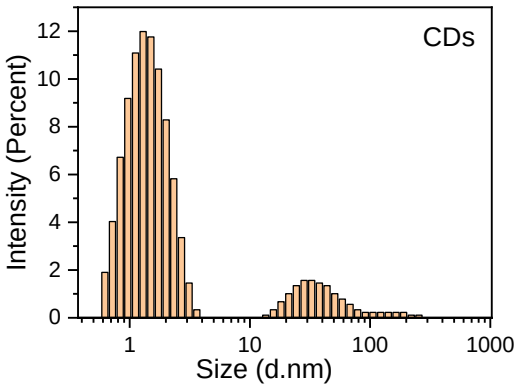

Figure 3.9. Intensity-weighted size distribution of the CDs obtained by dynamic light scattering.

3.3 Photocatalysis setup and product detection

In this thesis, a solar simulator with a Xenon lamp (300 W) has been utilized in the light source of photocatalytic reactions. The spectrum of light generated by the Xenon lamp is shown in **Fig. 3.10**, where there is a large ratio of near-infrared light spanning from ~700-1000 nm. A water filter is placed in front of the Xenon lamp to remove near-infrared light, as the near-infrared light would heat the solution. As a result, the temperature of solution for photocatalytic measurement remains in the range 25-30 °C throughout the measurements.

For photocatalytic activity measurement, the total volume of the solution, including CDs, water, and hole scavenger, is exact 2 mL. Methanol or Na_2SO_3 (1 M), whose volume accounts for 10 vol%, is employed as a hole scavenger. The pH value of the solution can be delicately adjusted to 3, 13, 15 with HCl or NaOH solution.

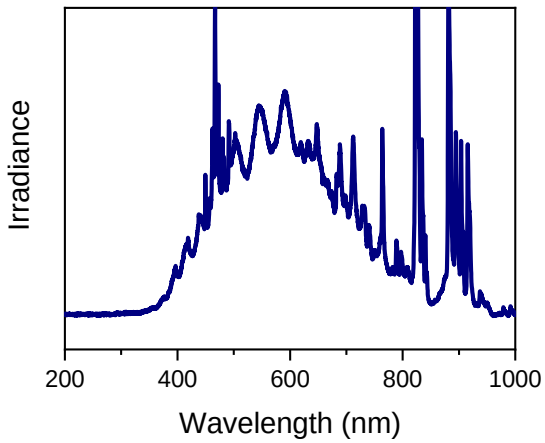

Figure 3.10 The spectrum of a Xenon lamp

The application of CDs is photocatalytic hydrogen generation. Here a gas chromatograph is utilized in identifying and calculating the amount of produced hydrogen. The diagram of a gas chromatograph is as shown in **Fig. 3.11**. The working principle is based on the fact that different gas passing through the column has various speeds, which is determined by the intrinsic properties of the materials and the interaction with the column. After passing through the column, the gases arrive at a thermal conductivity detector (TCD) at different time delays. The TCD possesses a current-conducting wire surrounded by the flowing gas, in this case, argon. Due to the difference in the heat conductivities, gases can be identified, and the amount can be also calculated.

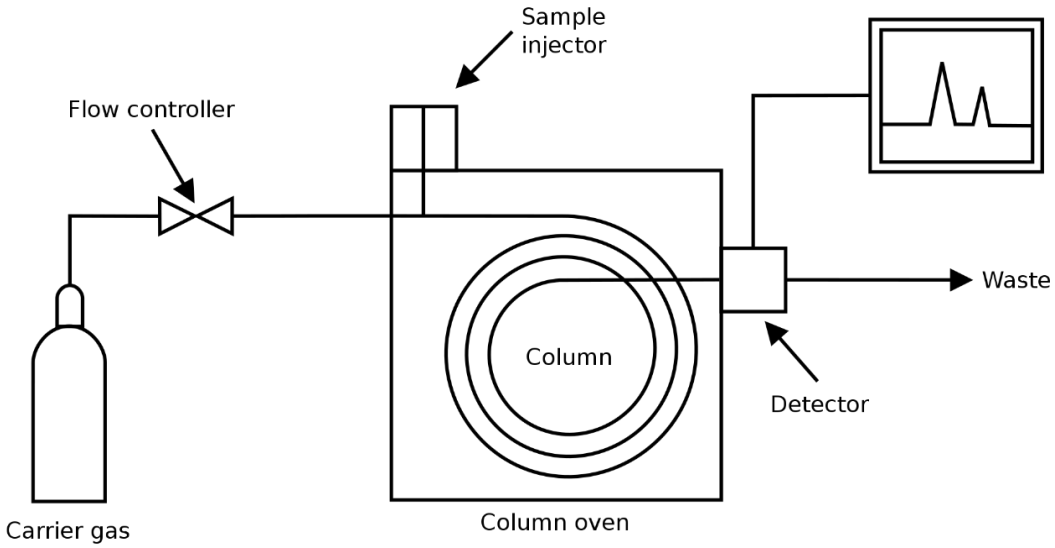

Figure 3.11. The diagram of the gas chromatography

In this thesis, Shimadzu GC 2014 has been utilized in calculating the hydrogen production.

3.4 Identification of the photobase effect

The identification of the photobase effect can be achieved by combined characterization of steady-state absorption and photoluminescence spectroscopy.

Absorption of photons results in the generation of electron and hole pair. In most cases, it occurs only for the photon with energy larger than the bandgap, as explained in detail in **Section 2.1.2**. In this work, the commercial setup "Cary 5000 UV-Vis-NIR spectrophotometer" is employed. The details about the spectroscopy can be referred to the PhD thesis of my colleague Benhard Bohn. Recalling the photoinduced proton transfer takes place in the excited state rather than in the ground state (**Section 2.3.4**), the absorption process will not be affected by the reaction in the excited state. Therefore, it can be inferred that the absorption spectrum of the deprotonated sample is the same as that of the sample protonated in the excited state. The absorption spectra of two control samples are needed: the deprotonated sample and the sample that can protonate in the excited state. The absorption spectrum of the deprotonated species can be acquired in acetonitrile, a typical

non-proton-donor solvent. In this thesis, as we focus on photocatalytic water splitting, water is selected as the proton donor. Therefore, the absorption spectra of the protonated species can be collected in a water/acetonitrile mixed solution.

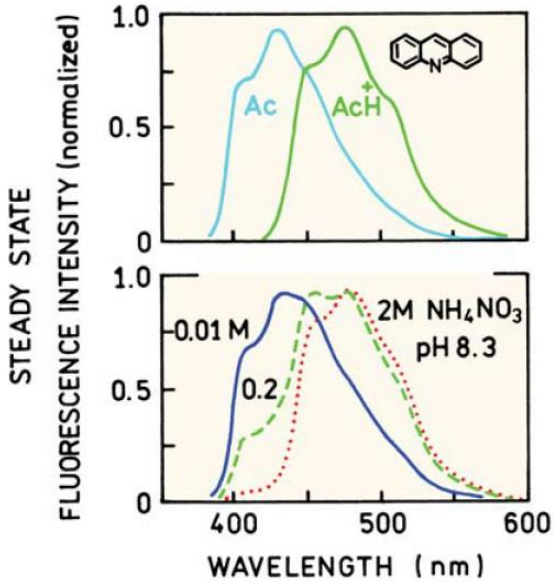

Figure 3.12 The fluorescence spectra (top) of deprotonated and protonated acridine. The fluorescence spectra (bottom) at pH 8.3 with increasing concentration of ammonium nitrate. [adapted from reference[162]]

After photon absorption, the excited molecule can relax to the ground state radiatively and nonradiatively. The radiative recombination process can be characterized by a steady-state photoluminescence spectrometer. In this thesis, two kinds of PL spectrometers are employed: *Flurolog 3, Horiba* and *Cary Eclipse, Aglient Technologies*. Steady-state PL spectra contain essential information about the excited state reactions. If the excited state protonation occurs, the protonated species have lower energy and emit photons with a longer wavelength. Therefore, a new component is expected to show up in the longer wavelength of the PL spectrum. The ratio/intensity of the new component can grow with the increasing ratio of water (proton donor) in the mixed solvents. A typical example is acridine, as shown in **Fig. 3.12**. The PL spectra redshifts to overlap that of protonated species with increasing ammonium ion concentration that serves as a proton donor.

In summary, to identify the photoinduced proton transfer process, the absorption spectra should remain the same, but the corresponding PL spectra are expected to redshift with an increasing water ratio in the mixed solution.

3.5 Time-resolved and ultrafast spectroscopy

3.5.1 Time-correlated single-photon counting

The lifetime of the photoexcited charge is an important parameter as it can provide helpful information on the deactivation pathways in the material. Together with the quantum yield value, radiative and nonradiative rate constants can be calculated. To this end, time-correlated single-photon counting (TCSPC) can be utilized in obtaining the time-resolved fluorescence. The principle of TCSPC is shown in **Fig. 3.13**.

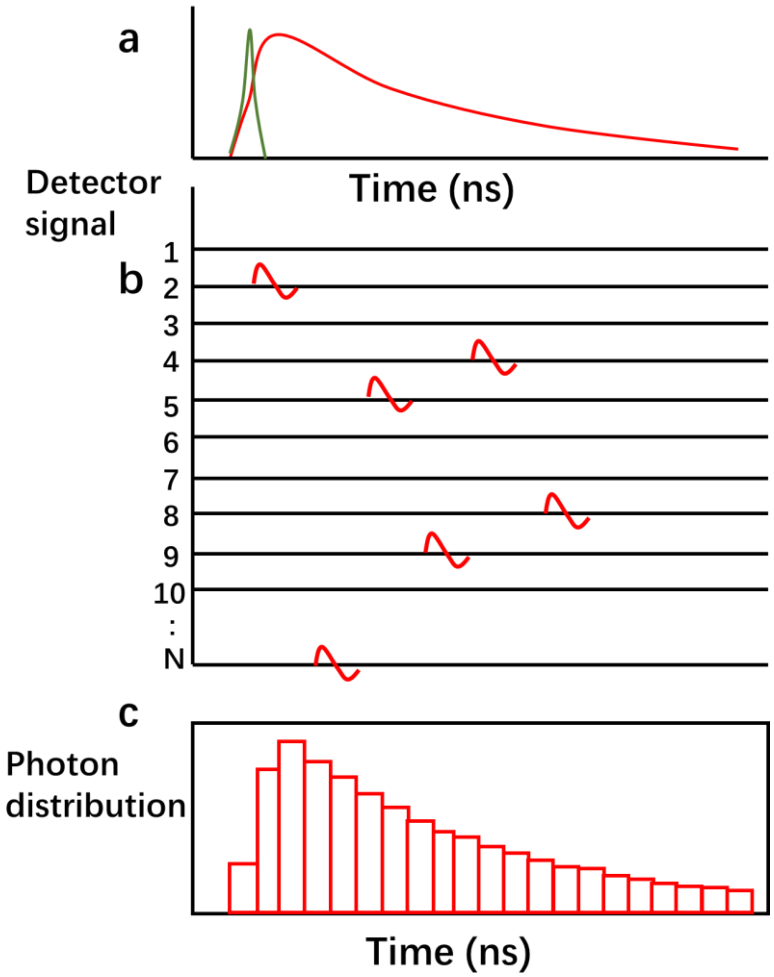

Figure 3.13 Principle of TCSPC. a). A typical PL decay together with a laser pulse. b) The pulses collected from the individual emitted photon over time. The photons are measured at different time delays after sending the *N*th laser pulse. c) A typical histogram for the case of PL photons, which resembles the PL decay. [adapted from reference [140]]

After the luminescent sample is excited with a laser pulse, a typical PL decay curve can always be observed in different fluorophores, as shown in **Fig. 3.13(a)**. As discussed in **Section 2.3.2**, the deactivation process is a random event. Following the excitation laser pulses, photons from the excited sample are emitted randomly during their lifetime. The

possibility for a spontaneous radiative recombination for fluorophore remains the same. Therefore, the photons can arrive at the detector with different time delays (**Fig. 3.13(b)**). Meanwhile, the time gap between the excitation laser pulse and the individual photons can also be calculated and stored in the histogram. The obtained time delays are plotted against the photon numbers as a histogram in **Fig. 3.13(c)**. The *x*-axis is the time difference, and the *y*-axis is the number of photons collected at a specific time delay. In this way, the histogram that can present the PL decay curve is acquired. Generally, the single-photon detector is set to detect not more than one photon per laser pulse. Therefore, if a second photon is also detected after the laser pulse, it would not yield another data point. In general case, the detection rate is typically 1 photon per 100 excitation pulses to minimize the events.

On the one hand, to obtain the whole decay and avoid measurement errors, the laser repetition rate should be small enough so that the excited sample has enough time to relax to the ground state. On the other hand, the laser repetition rate should also be large enough to collect more photons to obtain a smooth decay. Therefore, a compromise has to be made. For the case of monomolecular recombination, the PL intensity decays monoexponentially, while for bimolecular or other more complex deactivation processes, the PL decay can be deconvoluted. Consider the case of two excited localized luminescence centers, if their emissions wavelengths overlap, the PL decay can be fitted with a double-exponential decay, as shown in **Eq 3.3**.

$$\boldsymbol{i(t) = a_1 e^{-t/\tau_1} + a_2 e^{-t/\tau_2}} \tag{3.3}$$

wherein a_i $(i = 1,2)$ is the weightage of an individual component. The parameters a_1, a_2, and τ_1, τ_2 can be derived from the experimental decay curves. However, the attempt to fit the decay curve with more than two exponentials, shown in **Eq.3.4**, has to be done cautiously.

$$\boldsymbol{i(t) = \sum_{i=1}^{j} a_i e^{-t/\tau_i} \ (j \geqq 3)} \tag{3.4}$$

From the point of mathematics, a perfect fitting should be made possible between the calculation and the data curve. However, from the point of physics meaning, such a fitting can hardly be evidence for three or more existing luminescence centers. It is because that any decay curve can be modelled with three exponentials very nicely. Therefore, it makes the resulting value of a_i and τ_i highly questionable [132].

3.5.2 Transient absorption spectroscopy

Transient absorption spectroscopy (TAS) is a pump-probe spectroscopic technique especially suited to study the dynamic process of optical excitation. The technique is based on time-dependent changes in the excited-state absorbance of the sample. Typically, one pump pulse is used to excite the sample and generate electron-hole pairs. Subsequently, one probe pulse is used to investigate the carrier dynamics triggered by the pump pulse. As the name suggests, the probe pulse is used to track the perturbation created by the pump pulse.

Since the excited carrier distribution changes with time and alters the absorption of the sample, the technique can be used to investigate the underlying carrier dynamics. Thus, it is a powerful tool even for materials that emit weakly or do not emit at all. In this thesis, a transient absorption spectrometer from Newport is employed to investigate the photobase effects. The basic scheme of an experimental setup for femtosecond transient absorption spectrometer is shown in **Fig. 3.14**. A comprehensive explanation of the TAS setup can be found in the PhD thesis of my colleague Bernhard Bohn [163].

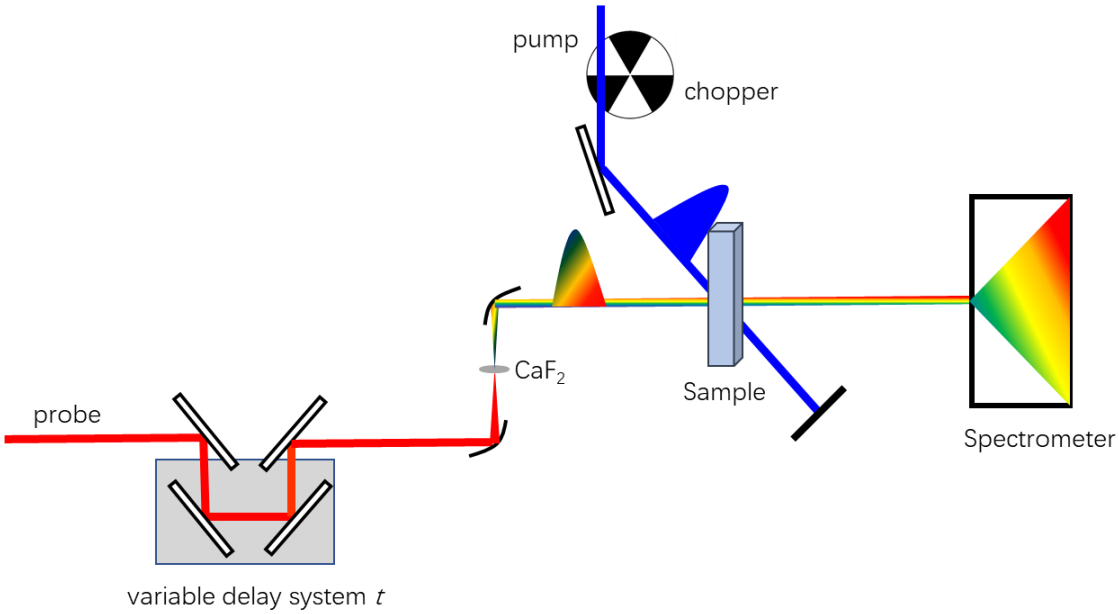

Figure 3.14 Scheme of an experimental setup for femtosecond transient absorption spectroscopy. The pump pulse (blue) is directed to go through the mechanical chopper, and every second pulse is blocked. The probe pulse (red) is focused on a CaF_2 crystal to generate a continuum light (indicated by colors). The probe pulse is directed to overlap the pump pulse spatially and temporally. The variable delay system can control the time delay between the pump and probe laser pulse.

In this TAS setup, the femtosecond laser pulses can be produced by a multi-pass *Ti:Sapphire* regenerative amplifier laser system (*Libra-HE+* system from *Coherent*). The ~100 fs laser pulses are centered at 800 nm at a repetition rate of 1 kHz. With a beam splitter, two laser beams, functioning as pump and probe pulse, can be generated. The wavelength of the pump pulse can be tuned by an Optical Parametric Amplifier (OPA). The wavelength of the resulting pump pulse can vary from 190 nm to 12 μm. To achieve such a broad wavelength range, a combination of several nonlinear processes takes place within the OPA, such as second-harmonic generation, white light generation, sum/difference frequency generation. In this thesis, as CDs absorb only in the UV range, the ideal wavelength of the pump pulse is shorter than 350 nm. The pump pulse has to go through a mechanical chopper before reaching the sample (solution in a thin cuvette or film on the substrate). The chopper synchronized with the laser at a repetition rate of 1 kHz. The chopper wheel blocks the beam every second pulse, which offers an opportunity to study the respective dynamics with/without excitation. When the pump pulse is blocked and only the weak probe pulse

reaches the sample, the situation is similar to that in steady-state absorption. The transmitted spectrum is measured and recorded by a high-performance multichannel detector. When the pump pulse is unblocked, the sample is excited, and electron and hole pairs are generated. The transmitted signal of the probe pulse is different from that in the "unpumped" case with the excited states populated. The detector alternatively receives the transmitted probe pulse from the "pumped" and "unpumped" case. Thus, the carrier dynamics triggered by the pump pulse can be obtained.

For the probe pulse, before reaching the sample, the pulse will first pass through a CaF_2 crystal that can convert the 800 nm laser into a continuous wavelength spectrum via white light generation. The continuum laser can extend the visible range to the UV region, termed "white light". Therefore, the broad continuum probe pulses can be used to measure the carrier dynamics over the whole broad wavelength range without extending the measurement time. Another crucial step is to control the time delay between the pump and probe pulses. A moving linear delay stage made of retroreflector mirrors can change the probe beam path length. In this way, the time delay between the two beams can be controlled by the path length delicately. In this setup, the maximum delay between the pump and probe pulse is up to 3,000 ps. Generally, the size of the probe beam is smaller than that of the pump beam. In this case, the probe beam has a diameter of 650 μm, which can ensure that the probe sample volume is homogeneously excited. The probe pulse should be directed to overlap the pump pulse temporally and spatially. Especially, the exact temporal overlap between the pump pulse and the probe pulse is defined as time zero, t_{delay}=0. After passing through the sample, the transmitted intensity of the probe pulse is further directed into a detector, and the information at different wavelength is recorded by a spectrometer. At each time delay, two consecutive transmitted pulse pairs due to the mechanical chopper are recorded. Then, the delay line will move to another scheduled time delay between the pump and probe pulse, and the procedure above is repeated.

According to all the description above, the change in absorbance $\Delta OD(\lambda)$ caused by the pump pulse at different time delay (t_{delay}) can be calculated (**Eq 3.5**)

$$\begin{aligned} \Delta \boldsymbol{OD}(\boldsymbol{\lambda}) &= \boldsymbol{OD}_{\mathbf{pumped}}(\boldsymbol{\lambda}) - \boldsymbol{OD}_{\mathbf{unpumped}}(\boldsymbol{\lambda}) \\ &= \mathbf{log_{10}}\left(\frac{\mathbf{I_{unpumped}}(\boldsymbol{\lambda})}{\mathbf{I_0}(\boldsymbol{\lambda})}\right) - \mathbf{log_{10}}\left(\frac{\mathbf{I_{pumped}}(\boldsymbol{\lambda})}{\mathbf{I_0}(\boldsymbol{\lambda})}\right) \\ &= \mathbf{log_{10}}(\mathbf{I_{unpumped}}(\boldsymbol{\lambda})) - \mathbf{log_{10}}(\mathbf{I_{pumped}}(\boldsymbol{\lambda})) \\ &= \mathbf{log_{10}}\left(\frac{\mathbf{I_{unpumped}}(\boldsymbol{\lambda})}{\mathbf{I_{pumped}}(\boldsymbol{\lambda})}\right) \end{aligned} \tag{3.5}$$

wherein I_0 is the initial intensity of the probe pulse before it reaches the sample. According to **Eq 3.5**, I_0 is cancelled out, indicating the change in the absorbance can be calculated in terms of the intensity of two transmitted probe pulses. The value $\Delta OD(\lambda)$ can be measured by two consecutive pulse pairs. Given the repetition rate 0.5 kHz, the spectra with a different time delay can be obtained every 2 ms, on the condition that all the charge carriers return to the initial state within 1 ms. The resulting TAS spectra can also be

referred to as absorbance difference spectra. In addition, the baseline of the absorbance difference spectra can be obtained by recording the spectrum before time zero (t_{delay}<0).

In most cases, the data collection procedure is repeated several times to test sample stability, the reproducibility and stability of the system. In this way, the difference in absorption spectra can be obtained. However, due to the different refractive index of light in matter (*e.g.*, in a lens), different spectra parts of the white light do not reach the sample at the same time. This is referred to as the chirp [164]. Thus, each wavelength has a different time zero which distorts the resulting spectra. The chirp can be further corrected with a MATLAB program written by my colleague Alexander Richter.

We can also view the "pump-probe process" in another perspective. The absorbance of a dilute solution is dependent on the absorption coefficient (ε), the thickness of the cuvette (l), and concentration (c) of the sample. According to Lambert-Beers law [138], the absorbance can be calculated according to **Eq 3.6**

$$\boldsymbol{OD_0 = \varepsilon l c} \tag{3.6}$$

After the pump pulse is imposed, the electrons are populated to excited states. Assume the concentration of the excited sample is c^*, and it has a smaller absorption coefficient ε^*. The absorbance can be derived (**Eq 3.7**)

$$\boldsymbol{OD_t = \varepsilon l(c - c^*) + \varepsilon^* l c^*} \tag{3.7}$$

Then the difference absorption can be calculated

$$\boldsymbol{\Delta OD = OD_t - OD_0 = (\varepsilon^* - \varepsilon) l c^*} \tag{3.8}$$

As **Eq 3.8** indicates, the difference absorption is proportional to the concentration of the excited sample (c^*). Meanwhile, the absorption coefficient ε is a function of wavelength (λ). Thus, **Eq 3.8** can be rewritten into **Eq 3.9**

$$\boldsymbol{\Delta OD(\lambda, t) = \big(\varepsilon^*(\lambda, t) - \varepsilon(\lambda)\big) l c^*(t)} \tag{3.9}$$

By varying the time delay (t) between the pump and probe pulse and recording the ΔOD at each time delay, difference absorption spectra can be obtained as a two-dimensional matrix of delay time and wavelength (λ). The spectrum is composed of two parts, $\varepsilon^*(\lambda, t)$ and $\varepsilon(\lambda)$, that is absorption coefficient in the excited state and ground state, respectively. The investigation and interpretation of $\Delta OD(\lambda, t)$ can reveal much information of the dynamical processes, such as relaxation/recombination, intramolecular electron transfer processes in organic molecules [165], excited-state energy migration in heavy metal complexes[166], and intersystem crossing in iron (II) photosensitizer [167, 168]. In general, the ΔOD mainly have three contributions [169]:

1) **Ground state bleach**. As the absorption coefficient in the ground state is decreased due to the phase space-filling in the excited state (**Eq 3.9**), ΔOD is negative. After being excited by the pump pulse, the probe beam will be less absorbed. Therefore, a negative signal can be observed in the wavelength where ground state absorption occurs.
2) **Stimulated emission**. After the sample is excited, one photon from the probe pulse can induce another photon's emission from the excited state, the stimulated emission. Generally, stimulated emission has the same wavelength as that of steady-state emission. The photon from stimulated emission is emitted in the same direction as the probe photon. As more photons arrive at the detector, an increase in the probe pulse intensity is detected in the spectrometer. It corresponds to a negative signal in the TAS spectrum.
3) **Excited-state absorption**. The electrons in the excited state can absorb the probe photons with specific energy and can be promoted to higher excited states. Consequently, a positive signal in the TAS spectrum will be observed in the excited-state absorption range. As the intensity of the probe pulse is weak compared to that of the pump pulse, the concentration of the excited state will not be affected significantly by the excited-state absorption [143].

There are many other effects possible, such as hot-carrier cooling [170, 171], bandgap renormalization [172, 173], optical Stark effect [174], contributing to the ΔA absorbance difference spectra.

In this thesis, transient absorption spectroscopy is utilized in investigating the photoinduced proton transfer and calculate the timescale of the protonation.

Chapter 4 Evidence of photobase effects on CDs photocatalysts

Photocatalytic water splitting can be a promising approach to fulfill carbon neutrality, as the technique utilizes sunlight in sustainably producing energy-rich fuel, hydrogen. Significant efforts have been devoted to increasing charge separation and extending the carrier lifetime, systematically explained in **Chapter 2**. Another limitation is the timescale mismatch between electron migration to the surface (~ps) and proton diffusion (~μs). The majority of the photoinduced charge carriers would recombine before the expected photocatalytic reactions occur. Rare trials or research have been reported to reduce the timescale of proton transfer in the photocatalytic system.

Carbon dots (CDs) are a newly emerging metal-free organic photocatalyst, and their photocatalytic efficiency was found related to the nitrogen positions [120]. Pyridinic nitrogen-containing CDs have been proved as efficient photocatalysts. Pyridine and its analogous N-heterocyclic compounds are bases that can be protonated at the nitrogen atom in the excited state. So far, the photoinduced proton transfer, also named photobase effect, has been well investigated [131, 138], but it has not been applied to photocatalytic reactions. The excited photobasic molecules can abstract protons in ultrafast timescale. A question naturally arises: is the photobase effect contributing to photocatalytic activity?

In this work, one hybrid system was designed: a non-photobasic CD with added acridine. Acridine, a model photobasic molecule, is introduced into the nitrogen-free CDs. First, the photobase effect within acridine is identified via steady-state absorption and PL spectroscopy. Then transient absorption spectroscopy was employed to extract the timescale of protonation. Finally, the photocatalytic performance was conducted, and the control experiment where non-photobasic molecules is added is to verify the role of the photobase effect in photocatalysis.

4.1 Photobase effect in acridine

As discussed in **Section 2.2.5**, photobasic molecules have a more significant affinity to protons in the excited state than the ground state. If the affinity is large enough, the excited molecules can abstract protons from protic solvent. The characteristic feature is that the pK_a in the excited state is generally much larger than that the ground state. Herein, acridine is selected as a model photobasic molecule for two reasons. The first one is because acridine is an N-heterocyclic aromatic compound, resembling the structure of CDs [158]. CDs have been found composed of polycyclic aromatic hydrocarbon, which is discussed thoroughly in **Section 2.2.3**. The second is due to the fact that the neutral pH locates between the ground state pK_a value (5.5) and excited state pK_a^* value (10.7) [175, 176]. The neutral environment, not corrosive or harsh, is ideal to photocatalytic reactions.

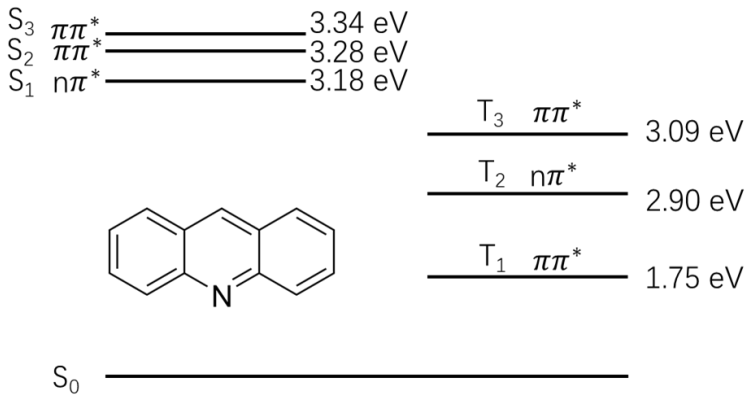

Figure 4.1 Calculated energy diagram of acridine in the vapor phase, and the inset is the chemical structure.

Before heading to discuss its optical properties, the electronic structure of acridine is investigated first. The theoretical and experimental investigation of acridine has been carried out decades ago due to its interesting optical properties, especially the dramatic fluorescence quantum yield difference in protic and aprotic solvents [176, 177]. The energy diagram of acridine has also been calculated [176], as illustrated in **Fig. 4.1**. The fact that S_1 and S_2 with two different configurations are close-lying is the reason for the difference, as their energy state order can be reversed by hydrogen bonding formation [177, 178], which has been explained in **Section 2.3.2**.

Let us first discuss how the molecular photobase effect manifests itself in the optical properties. The status (protonated, non-protonated) of acridine in the ground state and excited state is shown in **Fig. 4.2**. It indicates that acridine is protonated in the ground state in an acidic solution (pH<5.5), while acridine can be protonated in the excited state in a solution with a pH less than 10.7. While in solution with pH>10.7, even the excited acridine cannot be protonated. Therefore, the pK_a values in the ground and excite state divide the pH axis into three ranges: pH<5.5, 5.5<pH<10.7, and pH>10.7. Therefore, we can control protonation/deprotonation of acridine only by pH values.

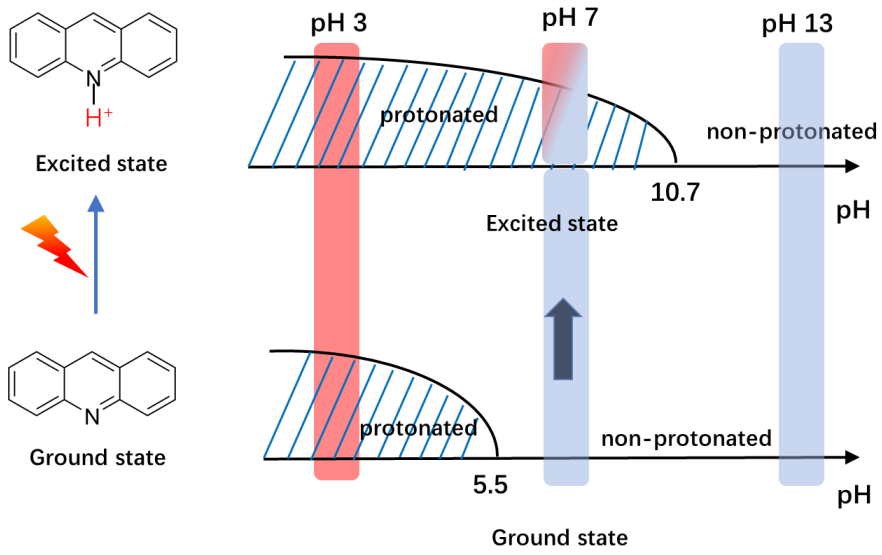

Figure 4.2 The status (protonated, non-protonated) of acridine in the ground/excited state throughout the pH axis. Three presentative values (3, 7 and 13) are selected. Blue and red color indicate non-protonated and protonated status, respectively.

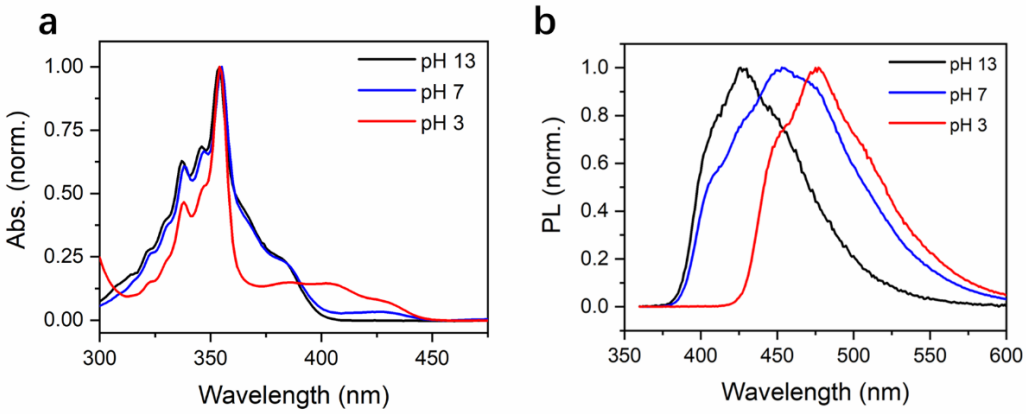

Figure 4.3 The absorption spectra and photoluminescence (PL) spectra of acridine at three different pH values (pH 3, pH 7 and pH 13).

Accordingly, three representative pH values are selected, pH 3, pH 7 and pH 13, to modulate three relevant populations of acridine: always protonated (both ground state and excited state, at pH 3), primarily non-protonated in the ground state, but protonated in the excited state (pH 7), and always non-protonated (pH 13). The corresponding absorption spectra at three pH are shown in **Fig. 4.3a**. The protonated acridine (pH 3) has extended absorption range up to 450 nm. The absorption spectrum at pH 7 is almost identical to that at pH 13 except the tiny difference in the visible range from 400 nm to 450 nm. The trivial difference is due to a small fraction (3%, see the calculation in **Appendix**) of the protonated acridine in the ground state. However, the PL spectrum of acridine at pH 7 is distinct from that at pH 13, as shown in **Fig. 4.3b**. A new component around 474 nm shows up in the photoluminescence spectrum at pH 7 except reservation of the feature at pH 13. Remarkably, the spectrum at pH 7 in the longer wavelength (start from 474 nm) overlaps

well with that of acidified acridine (pH 3). It means that the fluorescence of acridine at pH 7 has an immense contribution from the photoinduced protonated species, as it cannot be explained by the tiny ratio (3%) of ground-state protonation.

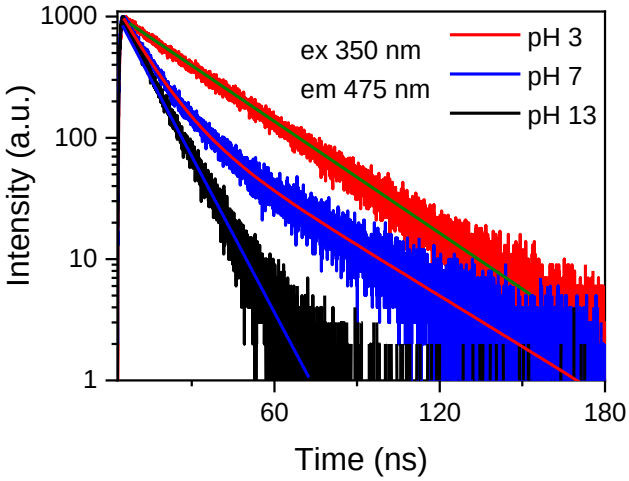

Figure 4.4 The semi-log plot of time-resolved PL decay of acridine at different pH measured at 475 nm.

The photobasic character of acridine can further be verified by the lifetime measurement at different pH. As shown in **Fig. 4.4**, the decay curves at pH 3 and pH 13 are mono-exponential with a lifetime of 27.5 ns and 9.7 ns, respectively. While the decay curve at pH 7 is clearly composed of two components, and it can be further fitted with two values: the lifetimes of protonated and non-protonated species. Moreover, the weightage of the lifetime of the protonated species constitutes around 20%, much larger than the value, 3%, due to ground-state protonation. It indicates that photoinduced protonation occurs in the excited state. Therefore, the photoinduced protonation behavior demonstrates the photobasic character of acridine.

In conclusion, acridine in neutral pH has almost same absorption spectrum as the non-protonated (**Fig. 4.3a**), but the emission has an enormous contribution from photoinduced protonated species (**Fig. 4.3b** and **Fig. 4.4**). Thus, acridine is proved to be photobasic as it can pull protons from water in the excited state. Theoretical simulations suggest that excited acridine in water can induce proton-coupled electron transfer [179]. One of the acridine-based derivatives, acridine orange, can abstract one proton even from alcohols coupled with an electron transfer [180, 181]. These findings further imply that the excited protonated acridine is prone to accept one electron, making it suitable for photocatalytic reactions. Here in this work, acridine is integrated with non-photobasic CDs to form a hybrid system, where CDs can function as an electron donor to reduce the protons acridine pull from water. The hybrid system is further applied to photocatalytic water splitting.

4.2 Attaching photobase to CDs

4.2.1 Optical properties of CDs

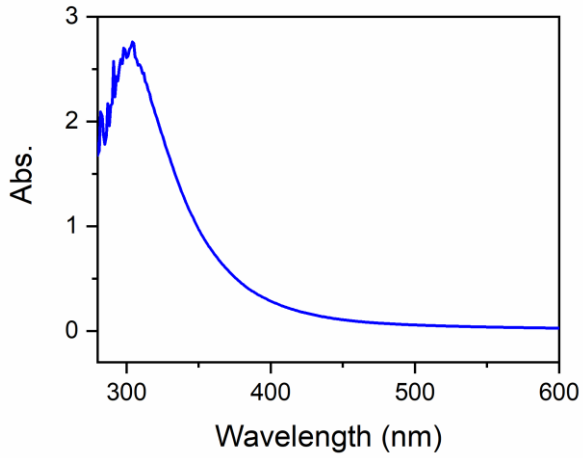

Figure. 4.5. The absorption of CDs in ethanol

Let us first investigate the optical properties of CDs. The nitrogen-free CDs were synthesized by hydrothermal method at 200 °C, and the synthesis details are in **Section 3.1.1**. The "nitrogen-free" requirement is stressed to rule out the possibility of the formation of pyridinic nitrogen [120]. The size of the resulting CDs is around 2.5 nm, as revealed in the TEM images in **Section 3.2.1**. The absorption spectrum of CDs, shown in **Fig. 4.5**, is smooth, featureless but has a strong absorption resonance in the UV range with a tail extending to the visible range. The PL spectra of CDs in ethanol, as shown in **Fig. 4.6a**, have a maximum intensity around 370 nm with 320 nm excitation wavelength but redshifts with a dramatically decreasing PL intensity at longer wavelength excitation.

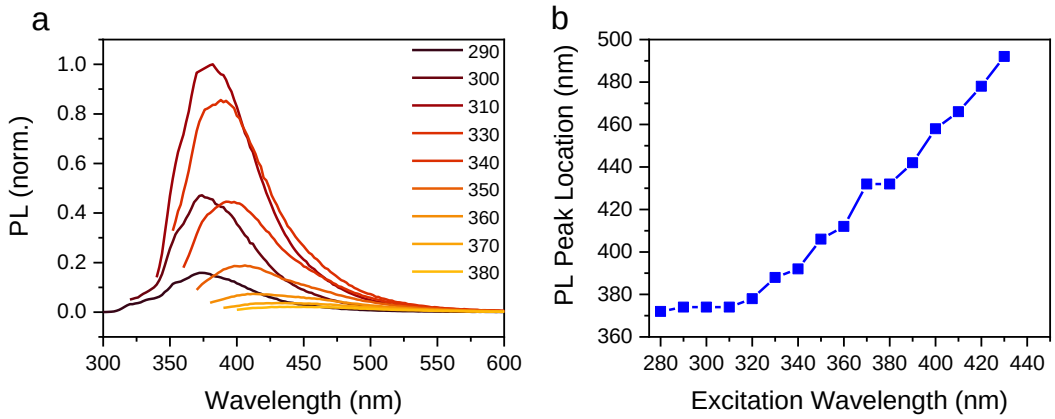

Figure. 4.6. a) The photoluminescence spectra of CDs in ethanol at different excitation wavelengths, b) Excitation wavelength-dependent emission: the PL peak location versus different excitation wavelengths.

A large Stoke-shift is found for each excitation wavelength, ranging from 60 nm to 90 nm. The decrease in PL intensity is correlated with the decreasing absorbance at longer wavelength. As shown in **Fig. 4.6a**, if the excitation wavelength is below 320 nm, the photoluminescence of CDs is independent of excitation wavelength, and the PL maximum resides between 370 to 378 nm. If the excitation wavelength increases from 330 to 440 nm, a linear dependence of emission wavelength on the excitation wavelength is observed in **Fig. 4.6b**. The excitation wavelength-dependent emission is interpreted as the energy transfer between selectively excited polycyclic aromatic hydrocarbons with different conjugation lengths. The large Stokes shift is due to exciton self-trapping, allowing dimer formation and structure relaxation in the excited state [93].

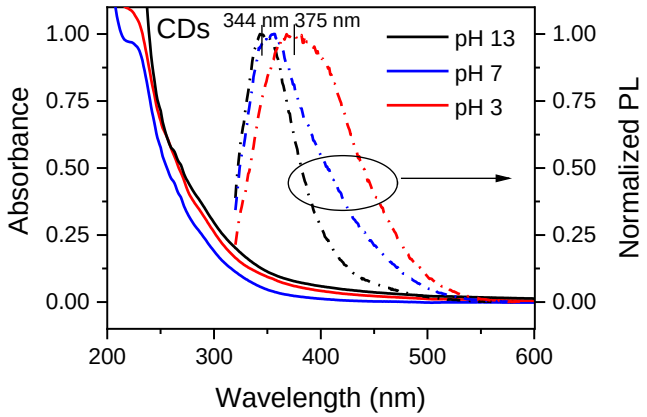

Figure 4.7 The absorption (solid line) and fluorescence (dot-dash line) spectra of CDs at three different pH values. The PL spectrum is acquired with excitation at 310 nm.

The type of solvents can affect the optical properties of organic materials dramatically. Generally, photocatalytic reactions are conducted in water. Therefore, the solvent ethanol was removed by flowing nitrogen, and the same amount of deionized water was added. As discussed previously, the pH value of the medium can control the protonation status in the ground/excited state. Three pH values (3, 7 and 13), in accord with acridine, are selected. The absorption spectra of the CDs, illustrated in **Fig. 4.7**, do not show dependence on pH. Meanwhile, CDs remain photoluminescent at different pH, though PL is quenched in water. The PL spectra with excitation wavelength 310 nm at three pH values are also presented. However, the resulting emission is pH-dependent: at pH 7, the PL peak is located at 350 nm, and blueshifts to 343 nm at pH 13 and redshifts to 375 nm at pH 3. The pH sensitive PL is also well documented, which is attributed to the intramolecular charge transfer [182].

4.2.2 Optical properties of CD/photobase hybrid

Since the optical properties of CDs and acridine have been investigated, it is time to investigate the optical properties of CD/acridine hybrid system, and explore the possible electron/energy transfer between them. The CD/acridine hybrid was prepared in two ways. The first one is relatively straightforward. The CDs were synthesized, redispersed in water, and further mixed with an aqueous solution of acridine. Acridine is anticipated to attach to

the surface of the CDs. In the second way, acridine was mixed with the CDs' precursor, polyethylene glycol, prior to synthesis. After the polymer got carbonized, acridine molecules, stable up to 346 °C, are expected to survive the high temperature and are located within the CDs either as free molecules or incorporated into the sizeable N-heterocyclic structure. The structure can mimic the proposed structure of N-doped CDs [93]. The two ways of acridine inclusion can complicate the interpretation of the individual contribution. Herein, the analysis and interpretation of the optical properties mainly focus on the samples from the first method, and the resulting sample from the second method functions as a reference.

As the size of the acridine molecule is small and is slightly soluble in water, no direct evidence can be found in HRTEM that acridine molecules are attached to the surface of CDs. However, it can be identified by comparing the optical properties of CDs and CD/acridine hybrid. Due to the oxygen-containing functional groups at the surface, CDs can function as proton donors. CDs can form hydrogen bonds with the nitrogen atom from the acridine. In this case, the distance between the CD and acridine is shortened, beneficial to the possible electron or energy transfer. Herein this part focuses on identifying the possible electron transfer or energy transfer between CDs and acridine from the analysis of optical properties.

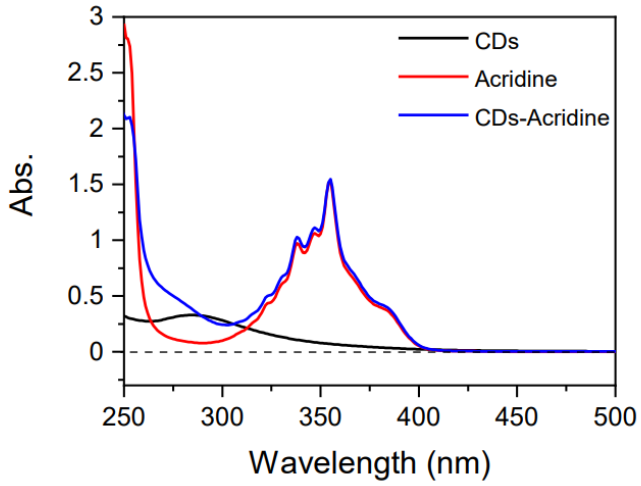

Figure.4.8 The absorption spectra of CDs, acridine and CD-acridine were taken at pH 7.

The absorption spectra of individual components (CDs and acridine) and the hybrid system are depicted in **Fig. 4.8**. Acridine has strong absorbance around 350 nm, while the absorbance of CDs is mainly centered in 280 to 310 nm. No new absorption peak is observed in the hybrid where the absorbance of acridine dominates the absorption.

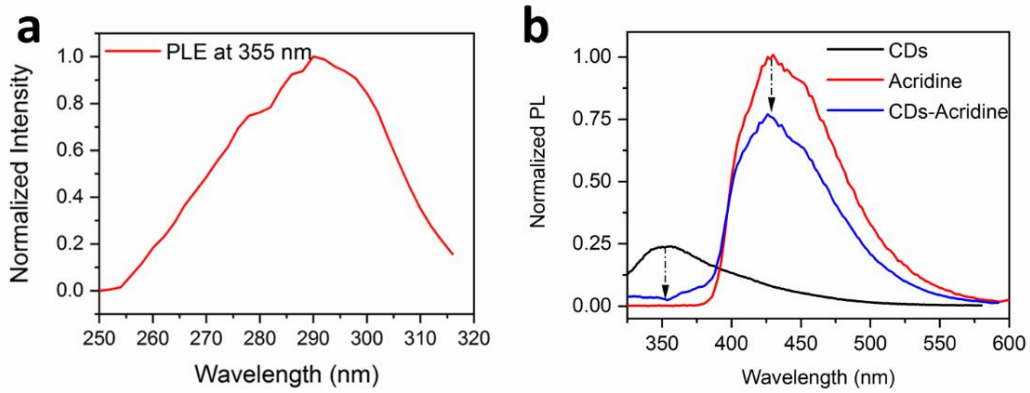

Figure. 4.9. a) Photoluminescence excitation spectrum of CDs at 355 nm; b) Comparison of the PL spectra of CDs, acridine and the CD/acridine sample acquired at 300 nm excitation.

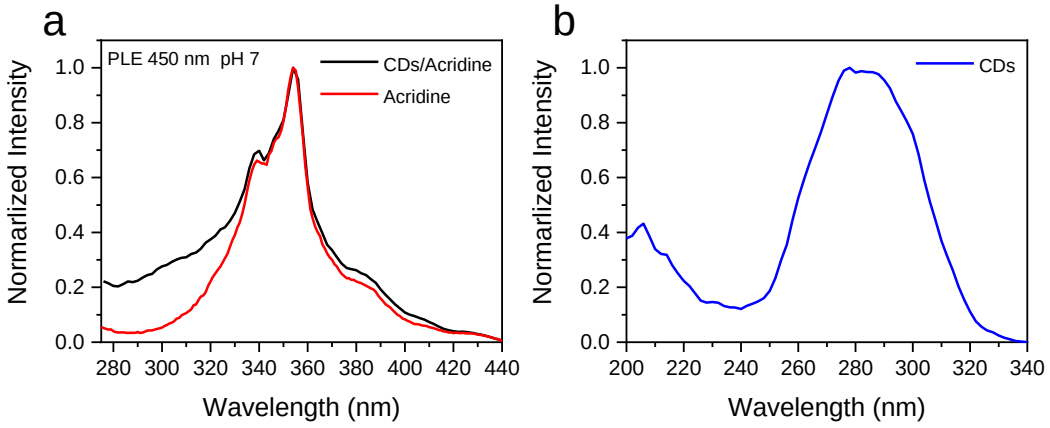

Figure. 4.10. The photoluminescence excitation spectra (λem = 450 nm) of acridine, CD/acridine hybrid (a) and CDs alone (b)

To investigate the role of PL from CDs in the hybrid system, PL excitation (PLE) spectra for emission at 355 nm were acquired. This wavelength is selected to match the emission of free CDs, and the result is shown in **Fig. 4.9a**. The PLE spectrum (**Fig. 4.9a**) peaks around 286 nm, coinciding with the absorption of CDs. Interestingly, the PL of CDs at 350 nm is significantly quenched in the hybrid system (**Fig. 4.9b**), implying the possibility of electron transfer or energy transfer from CDs to acridine. The Förster energy transfer is possible as the PL of CDs (located around 350 nm) is in the absorption range of acridine. Therefore, the PLE spectra detected at 450 nm where the hybrid system emits were further measured, as illustrated in **Fig. 4.10**. In the normalized PLE spectra, the CD/acridine hybrid system (**Fig. 4.10a**) has a higher intensity than acridine (**Fig. 4.10b**) alone in the region of 280-320 nm where CDs absorb, implying energy transfer from the CDs to acridine can occur.

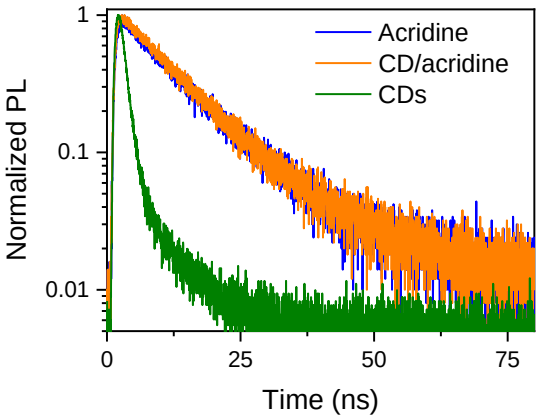

Figure. 4.11. Time-resolved PL decay of CDs, acridine, and CD/acridine hybrid, measured at 450 nm. The excitation wavelength is 350 nm.

The time-resolved PL decay can provide additional information on the deactivation process. The lifetime measurement is conducted at 450 nm, and the results are shown in **Fig. 4.11**. However, due to much stronger emission from acridine, the difference in the PL decay between the hybrid system and acridine alone is negligible. Thus, limited information from the lifetime measurement can answer whether electron transfer is possible. Herein, cyclic voltammetry, a powerful sweep method to investigate the potentials of LUMO/HOMO of molecules [183], is introduced to check the possibility of electron transfer. The cyclic voltammetry measurements of CDs and acridine are performed in mildly alkaline conditions to determine the relative positions of the LUMO level of the acridine and the conduction band edge of the CDs. Typically, 5 mg of the sample and 100 µL Nafion solution were dispersed in water/isopropanol and further sonicated to form a homogeneous slurry. 4.5 µL of the slurry was drop-cast on the polished working electrode and got dried at room temperature. Before the measurement, the electrode was immersed in the electrolyte for 20 minutes to reach an equilibrium state. The results are shown in **Fig. 4.12a.**

The arrows indicate the positions of the conduction band potential of CDs and the LUMO of acridine. The acridine molecule has a potential around -0.92 V, energetically lower than the conduction band (-1.03 V) of CDs. It implies that the electron transfer from CDs to acridine is possible. The overpotential (ΔE_1) of LUMO potential between CDs and non-protonated acridine is ~100 meV. What needs to be stressed especially is that the LUMO level of protonated acridine is even energetically lower [176, 184] as shown in **Fig. 4.12b**. The resulting overpotential (ΔE_2) will be even larger, which can provide a larger driving force for electron transfer.

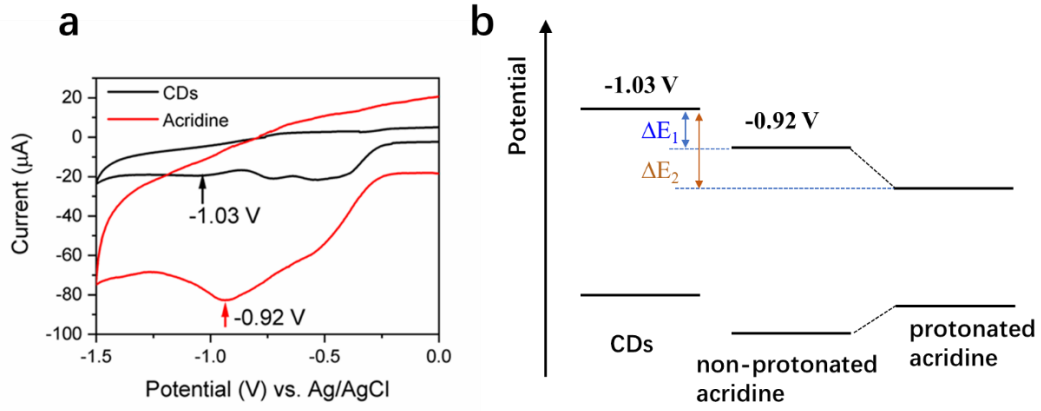

Figure.4.12 The cyclic voltammetry measurements (a) with a scan rate 100 mV/s. The arrows indicate the positions of conduction potential of the CDs and the LUMO level of acridine, respectively. (b) energy diagram of CDs, non-protonated acridine and protonated acridine. ΔE_1 and ΔE_2 are the overpotentials between CDs and non-protonated (protonated) acridine, respectively.

Overall, the optical results suggest that both electron transfer and energy transfer are possible between CDs and acridine. Another important conclusion drawn from the PL and absorption measurements of the hybrid system is that optical properties of acridine are reserved in the CD/acridine hybrid system.

4.3 Protonation dynamics

4.3.1 Protonation in acridine

The proton transfer (~μs) to the reaction sites is the rate-limiting process to photocatalytic water splitting. Electron migration to the surface (~ps) is usually much faster [11]. In the ideal case, electrons and protons can arrive at the reactive sites at the same time. This would reduce the chances of the recombination of the electron waiting for the protons. Photobase effect may help here, but to prove it, we need to determine the protonation timescale. In this thesis, transient absorption spectroscopy is employed to determine the timescale. The model photobase, acridine, at three different pH (pH 3, pH 7 and pH 13) was excited with 100 fs pump pulses at 350 nm and the differential absorption spectra were acquired as a function of time. The values were chosen to target the three regions of interest stemming from pK_a (5.5) and pK_a^* (10.7) of acridine. The results are shown in **Fig. 4.13**.

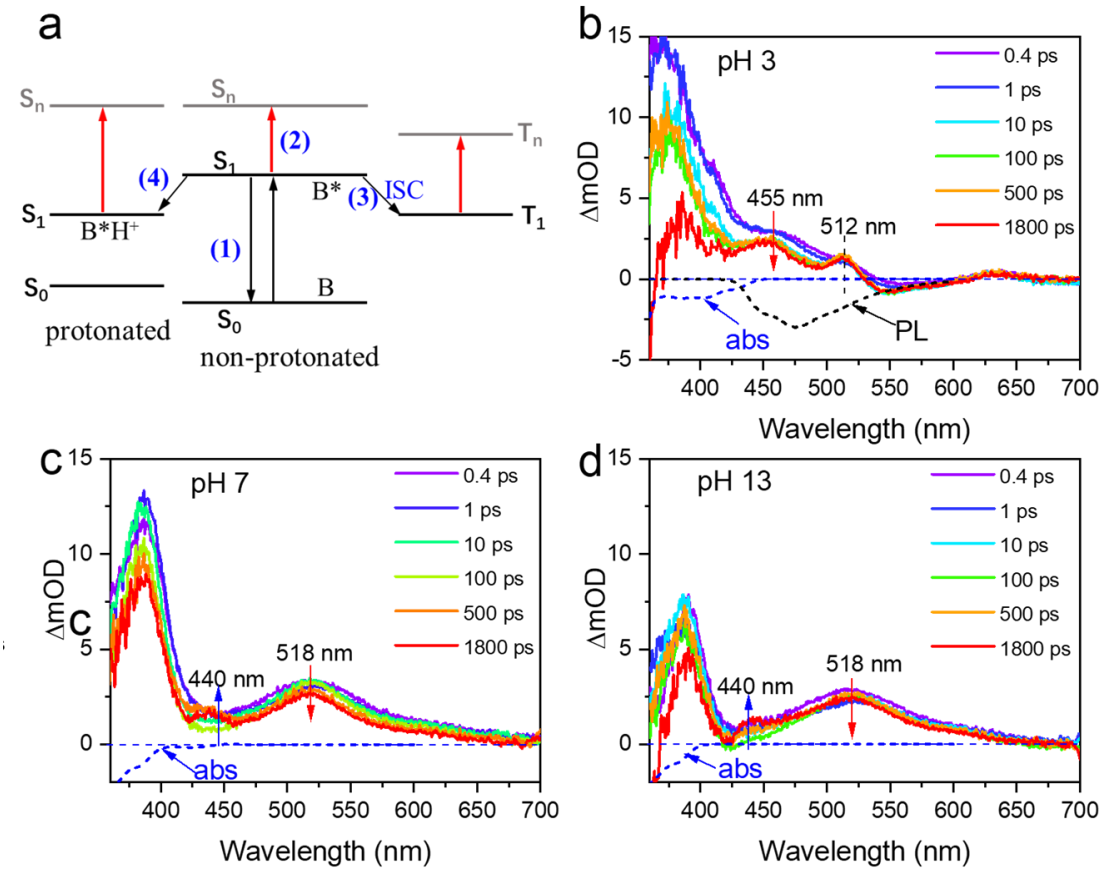

Figure.4.13 a) The schematic energy diagram of non-protonated and protonated acridine and the competing relaxation pathways: (1) recombination, (2) excited state absorption, (3) intersystem crossing, (4) excited state protonation. Transient absorption spectra of acridine at different pH b) pH 3, c) pH 7 and d) pH 13 with different time delay. The absorption is plotted inversely with a blue short-dashed line. The PL spectrum at pH 3 is also plotted inversely with short black dash.

As illustrated in **Fig. 4.13a**, after being excited, the photobasic molecules can relax to the ground state radiatively or nonradiatively. Three more competing pathways are also involved: excited state absorption (probe photons induced absorption), intersystem crossing and excited state protonation. This is complex and makes it difficulty analyzing the transient spectra. Therefore, to understand the protonation dynamics and how it can be manifested in the time-resolved spectra, it is important to understand first the spectra of the always protonated (at pH 3) and non-protonated species (at pH 13). Let us check acridine at pH 3 first. The differential absorption spectra at pH 3 are shown in **Fig. 4.13b**, which have two excited-state absorption (ESA) maxima (at 455 and 512 nm) as well as a negative absorption centered around 550 nm. ESA is caused by photon absorption, which promotes electrons from a lower excited state to a higher excited state. As the possibility of intersystem crossing in acridinium cation (Acr-H^+) is reported to be low [143], the two ESA is resulting from the singlet states (from S_1 to S_n). The ESA around 455 nm is only observed in pH 3, indicating it can be related with the protonated species. The minor ESA around 512 nm is considered to have the same origin as the broad ESA peak around 518 nm at pH 7 (**Fig. 4.13c**) and pH 13 (**Fig. 4.13d**). The blueshift from 518 nm (pH 7, 13) to 512 nm (pH 3) is caused by the superposition of negative absorption around 550 nm. Based on the energy diagram of non-protonated acridine in **Fig. 4.13d**, the ESA peak around 512/518 nm is assigned to the non-protonated species [185]. The presence of the minor ESA at 512 nm indicates that a tiny fraction of non-protonated acridine still exists even at pH 3. To further ascertain this claim, analogous measurements are conducted at a lower pH (pH 1), where the percentage of non-protonated species is negligible. The TAS spectra at pH 1 are shown in **Fig. 4.14**. Clearly, there is no ESA signal in the range of 500-525 nm, confirming the assignment of the 512/518 nm in **Fig. 4.13d**.

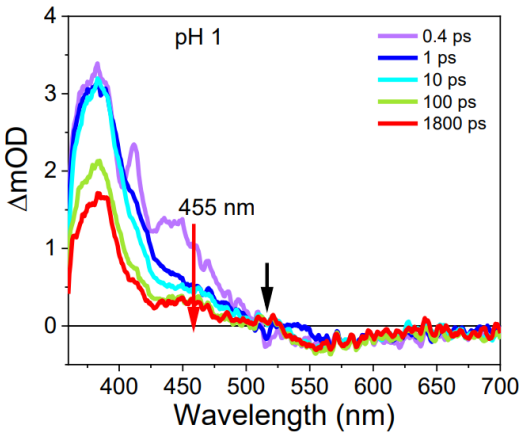

Figure.4.14 The transient absorption spectra of acridine acquired at pH 1. The black arrow indicated the expected position (512-518 nm) of the peak observed at higher pH. The red arrow at 455 nm is the ESA peak related to the S_1 to S_n transition of the protonated acridine.

Regarding the negative differential absorption starting from 515 nm (**Fig. 4.13a**), it is firstly compared with the absorption spectrum of the protonated acridine. The absorption spectrum is only extended to 450 nm, ruling out the possibility that the negative differential

absorption originates from bleach. It is further compared with the PL spectrum, and interestingly, the TAS spectrum in the 530-570 nm overlaps well with the tail of the PL spectrum. On this basis, we ascribe the negative differential absorption to the stimulated emission from acridinium cation.

Now let us investigate another situation where acridine cannot be protonated even in the excited state, that is, at pH 13. The TAS spectra at pH 13 is shown in **Fig. 4.13c**. The simulated emission around 550 nm is absent. This is consistent with numerous reports that acridine has a faster intersystem crossing rate in aprotic solvents where $^1(n, \pi^*)$ is the lowest singlet state [175-177]. According to the energy diagram in **Fig. 4.1**, the electrons can relax from the higher energy triplet state to the lower-lying T_1 state [176]. Hence, the ESA at 440 nm is ascribed to the excitation from T_1 to T_n, as shown in **Fig. 4.13c**, which has also been widely reported [185]. No traces of protonation have been observed, which is also expected in the high alkaline solution. A control experiment is done in a solvent where proton abstraction is more difficult. Ethanol was chosen because it has a larger pK_a (15.9) than water ($pK_a = 14$). The corresponding TAS spectra in ethanol is shown in **Fig. 4.15**. The differential spectrum in ethanol has the same ESA maxima at a slightly different location. Interestingly, the decay of the ESA at 550 nm is accompanied by the rise of ESA at 435 nm. The rising ESA with growing time is a typical feature of the increasing population of the triplet states. It indicates that intersystem crossing occurs from S_1 to T_1 in ethanol, as well as the alkaline solution. The same feature, growing ESA at 440 nm, is also observed in the TAS spectra obtained in neutral water (**Fig. 4.13b,c**).

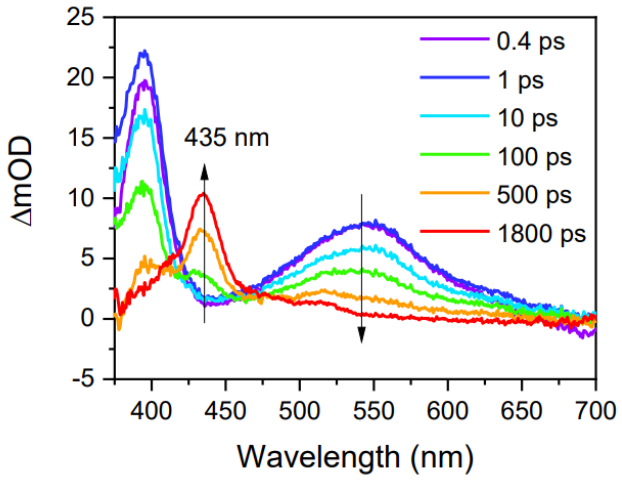

Figure.4.15 Transient absorption spectra of acridine in ethanol with specific time delay. The arrows indicate the decay of the excited state absorption (ESA) peak at 535 nm accompanied by the rise of the ESA peak at 435 nm.

Now that the TAS features in acridine at pH 3 and pH 13 have been interpreted, we can further investigate the photoinduced protonation at pH 7 and extract the protonation timescale. The TAS spectra at pH 7 in **Fig. 4.13b** broadly resemble pH 13 in **Fig. 4.13c**, consistent with the previous calculation that 97% of acridine is non-protonated at neutral

pH. To further elucidate the photoinduced protonation, the transient absorption traces at several specific wavelengths were plotted. The results are shown in **Fig. 4.16**. As discussed previously, the ESA at 455 nm is due to the transition from S_1 to S_n in protonated acridine. The wavelength of photoinduced protonated acridine is expected to locate around 455 nm. The trace at 455 nm is supposed to uncover the protonation process. However, the wavelength is quite close to the growing ESA at 440 nm from T_1 to T_n where the traces at pH 7 are dominated by the triplet growing ESA, same as at pH 13, as shown in **Fig. 4.16a**. As expected, this rise after 100 ps is absent in acidified solution (red curve in pH 3). To reduce the contribution of the growing ESA, a transient trace selected at 465 nm, shifting away from the ESA at 440 nm, is plotted and illustrated in **Fig. 4.16b**.

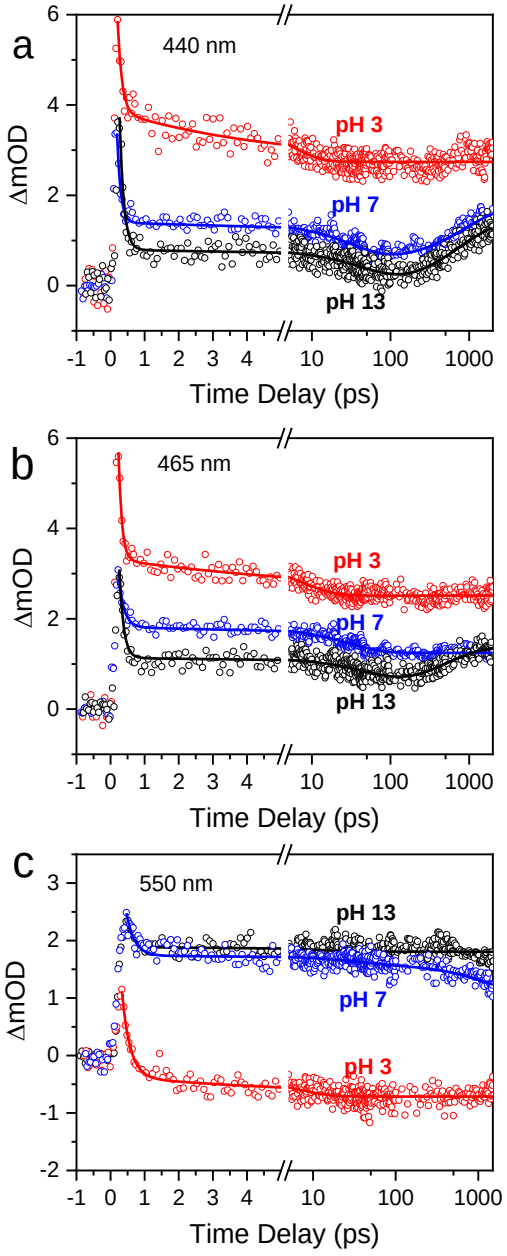

Figure 4.16 Transient absorption traces at **a** 440 nm, **b** 465 nm, and **c** 550 nm. Open circles are the data points, and the solid lines are fitting curves.

Interestingly, the traces at 465 nm (**Fig. 4.16b**) at pH 7 and pH 13 possess the same dynamics until 20-50 ps, implying at this stage the acridine is still non-protonated. After 30 ps, the two traces start to diverge. For pH 13, the trace possesses similar dynamics to that at 440 nm, while for pH 7, there is no rising signal due to T_1 to T_n. This provides direct evidence that acridine becomes protonated. After 30 ps, the dynamics at pH 7 shows the same trend as that at pH 3. The detailed fitting results are shown in **Table 4.1**. The status of protonation before and after 30ps is also illustrated in **Fig. 4.17.** The value, 30 ps, can be regarded the timescale of protonation in water. It is also in remarkable agreement with the protonation timescale of quinoline (28 ps) [142, 143], an analogous molecule to acridine.

To corroborate the finding, the traces at 550 nm were also analyzed. The results are illustrated in **Fig. 4.16d**, and the fitting results are shown in **Table 4.2**. In this region, stimulated emission of the protonated species is observed. Indeed, at pH 3 the negative differential absorption persists throughout the measurement time. On the other hand, initially, the decay dynamics of acridine at pH 7 is the same as that at pH 13. However, an additional decay component arises around 30 ps at pH 7, leading to a faster decay, consistent with the formation of the protonated species. Therefore, the spectroscopic analysis encouragingly shows that acridine is photobasic that can abstract proton in water within 30 ps. This very short time suggest that the proton transfer may be sufficiently fast not to limit the rate of photocatalytic process.

Table.4.1 Decay kinetics fit at 465 nm to a sum of two or three exponential terms.

pH Value	τ_1 (ps)	τ_2 (ps)	τ_3 (ps)
3	0.10	7.3	
7	0.16	29.7	
13	0.12	60.97	513.9*

*the value is negative in the fitting

Table.4.2 Decay kinetics fit at 550 nm to a sum of two or three exponential terms.

pH Value	τ_1 (ps)	τ_2 (ps)	τ_3 (ps)
3	0.24	6.2	
7	0.24	30.0	1617
13	0.14	12.2	

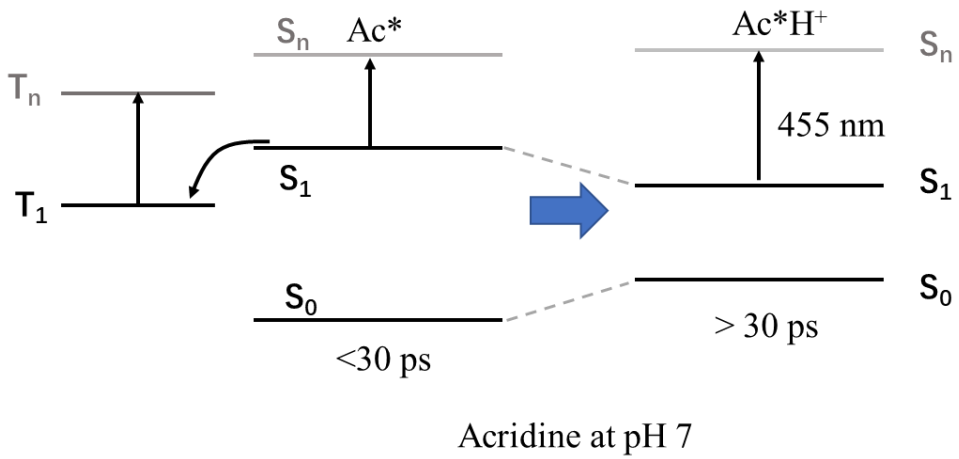

Figure 4.17. The schematic energy diagram of acridine at pH 7 before and after 30 ps.

4.3.2 Protonation in CDs/Photobase hybrids

Previous section has demonstrated that acridine can abstract protons from water at pH 7 within 30 ps. It is an encouraging result, indicating that the timescale discrepancy between the fast proton transfer and electron migration to the surface may be minimized. The scheme is shown in **Scheme 4.1**, where CD and acridine serve as the electron donor and co-catalyst, respectively. In the ideal case, electron from CDs and protons from acridine would arrive at the reaction sites at the same time, which can be beneficial to the photocatalysis. Before conducting the photocatalytic experiments, the first thing is to identify the protonation process in the hybrid system. Analogous TAS measurements were conducted, and the corresponding transient absorption spectra of the CD/acridine hybrid system are presented in **Fig. 4.18**.

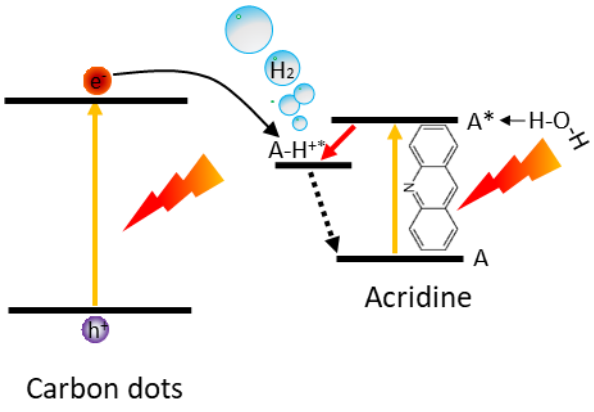

Scheme 4.1. Scheme of H_2 generation in CD/acridine hybrid system where excited acridine (A) abstracts a proton from water cooperating with the electron transfer from CDs to acridine.

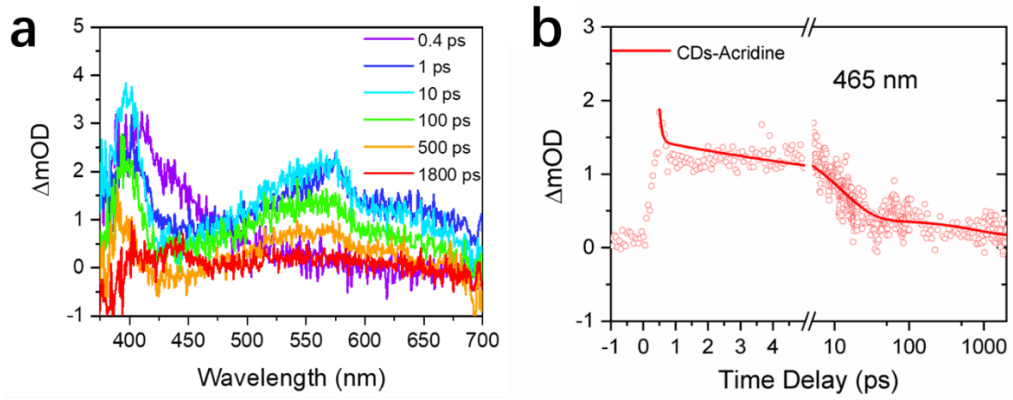

Figure 4.18 (a) The transient absorption spectra of the CD/acridine hybrid at pH 7. (b) The transient absorption traces at 465 nm. The data points are presented by the open circles and can be fitted with a multiexponential line (the solid line).

Although the incorporation of CDs complicates the analysis of the spectra of the hybrid system, however, it shows clearly that the spectra have the same features (ESA at 518 nm and 440 nm) as that in acridine alone, as shown in **Fig. 4.18a**. The new ESA peak around 560 nm originates from CDs. The transient trace at 465 nm is plotted to determine the protonation time, and the results are shown in **Fig. 4.18b**. Again, we do not see here the characteristic rise of the triplet state ESA, in line with the protonation of acridine. A very similar protonation time, around 30 ps, can be determined by fitting the transient trace at 465 nm. Therefore, the ultrafast spectroscopy shows that the photobase effect of acridine remains, and the protonation time of acridine in the hybrid system is also around 30 ps at pH 7.

The ultrafast protonation timescale, 30 ps, is comparable with the electron transfer between inorganic semiconductor and cocatalyst and is much faster than hole transfer [24, 70]. As a result, due to the photobase effect, the proton transfer is no longer a rate-limiting step in photocatalytic water reduction. The hybrid system is further applied to photocatalytic water splitting.

4.4 Photocatalytic H_2 generation with CDs

To further investigate the role of photobase effect in photocatalytic water splitting, no co-catalyst or metal cations are added to the photocatalysis system. The sample is illuminated with a 300 W Xenon lamp. The evolving hydrogen is detected and measured by a gas chromatography at a fixed time interval. The detailed method of hydrogen measurement has been discussed in **Chapter 3**. As shown in **Fig. 4.19a,b**, the average hydrogen generation rate of the hybrid system (0.032 $\mu mol \cdot h^{-1}$) at pH 7 is indeed much faster than that of an individual component (0.008 $\mu mol \cdot h^{-1}$ for both acridine and CDs). The enhancement is more straightforward for comparison when the hydrogen production amount is normalized by the mass of either CDs (**Fig. 4.20a**) or acridine (**Fig. 4.20b**). Moreover, the photocatalytic enhancement is irrespective of the preparation methods of the hybrid systems. In essence, the enhancement is even more significant (10-fold, **Fig. 4.19c**) for the sample where the acridine is embedded inside the CDs (synthesis method 2). As the acridine molecule is integrated within the CDs, the distance between CDs and acridine is smaller. Reasonably, the electron transfer between CDs and acridine molecules is more facilitated, as well as the proton-coupled electron transfer. It is more beneficial to hydrogen generation.

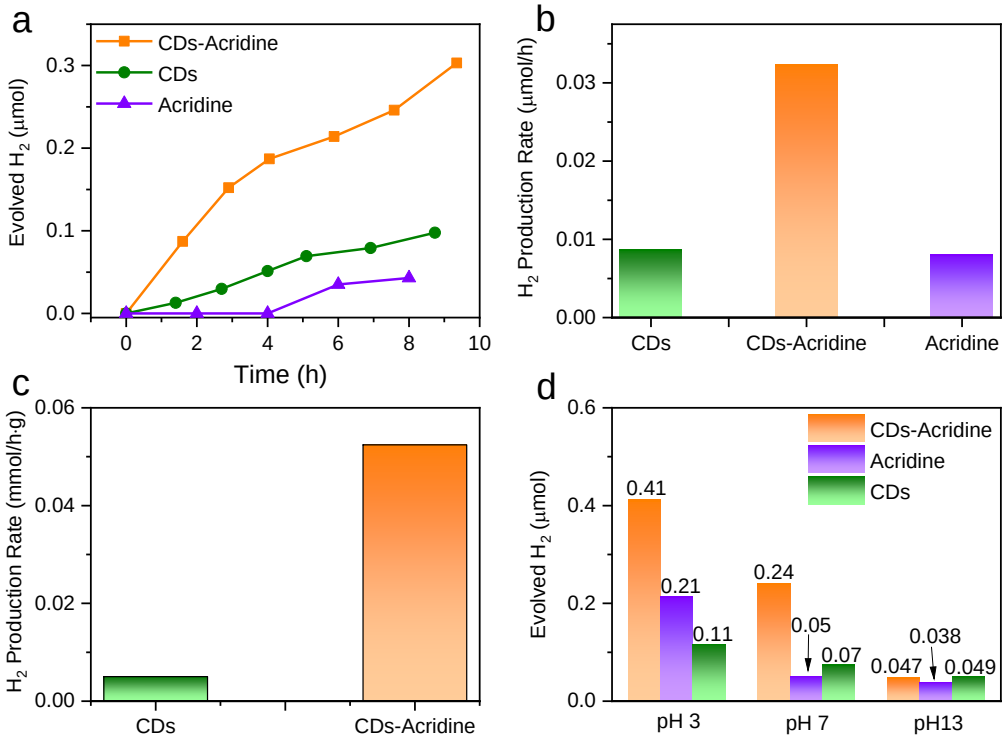

Figure. 4.19 Photocatalytic hydrogen generation of CDs, acridine, and the hybrid system. a) time-dependent hydrogen generation and b) the average hydrogen generation rate for CDs, acridine, and the hybrid at pH 7. c) photocatalytic enhancement in the system where acridine is embedded in CDs, prepared by acridine added into the precursor prior to synthesis. d) the total amount of evolved hydrogen over 6 h illumination at different pH.

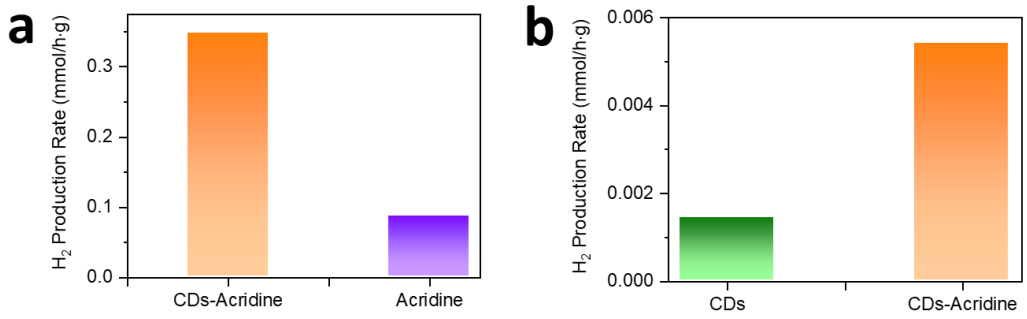

Figure. 4.20 The normalized photocatalytic hydrogen generation rate according to the mass of acridine (a) and CDs (b), respectively.

To further prove the role of photobase effect in photocatalytic performance, the pH of the solution is varied to control the photobase effect. The photocatalytic enhancement (2 times) is the strongest in neutral condition where the photobase effect manifests itself (**Fig. 4.19d**). However, no enhancement is found in the high alkaline solution (pH 13), as acridine cannot pull the proton even in the excited state. Although photocatalytic improvement is also observed in acidic solution (pH 3), the enhancement is much less pronounced. This is due to the fact that both CDs and acridine are protonated in the ground state, and the proton transport is not the rate-limiting parameter. Meanwhile, the fact that the hydrogen generation rate is highest at pH 3 also indicates that proton transport can be the limiting factor at its low concentrations.

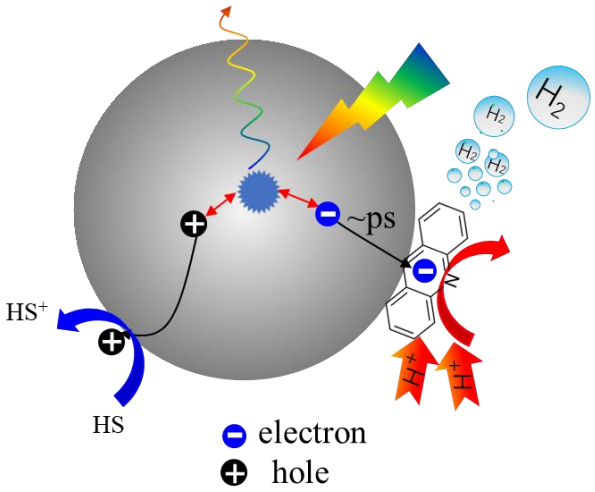

Scheme 4.2. The scheme of proton-coupled electron transfer in CD/acridine hybrid system. Acridine abstracts a proton from water, and electron transfer occurs from CDs to acridine.

Several studies have been done to investigate the process after protonation. It is reported that photoinduced proton transfer cooperates with electron transfer from the same molecules. Eventually, acridine radical (Acr-H•) can dissociate driven by light and lead to form molecular hydrogen via the Heyrovsky mechanism [186, 187]. Although one acridine

molecule can only abstract one proton, in carbon-based nanomaterials exist multiple photobasic moieties potentially in the vicinity. Thus, hydrogen generation via Tafel reaction is also possible [188]. In the CD/acridine hybrid system, the excited CDs can also donate electrons to the acridine, which is supported by cyclic voltammetry measurements. The electron transfer is anticipated to be more efficient for the structure where a photobasic moiety is integrated into polycyclic aromatic structures. This structure has been postulated in nitrogen-doped CDs and carbon nitride [120]. The time mismatch between proton transfer to the surface and electron migration to the surface can be reduced, which is depicted in **Scheme 4.2**. This can reduce the chances of possible charge recombination which is detrimental to photocatalysis. Generally, the direct electron transfer from the proton donor reported in literature will simultaneously result in an oxidized form of the latter (e.g. hydroxyl radicals).

4.5 Photocatalytic control experiments

To further identify the role of photobase effect in photocatalysis, control experiments are also conducted. A 400 nm long-pass filter was added prior to illumination of the hybrid system in a control experiment. The filter can cut off the absorption of acridine, thus the photoinduced proton transfer cannot occur. Meanwhile, CDs have a long tail in the visible range, implying that the CDs can still be excited by the light from a Xenon lamp. Only a tiny amount of hydrogen production can be detected, confirming that acridine is necessary to the photocatalysts. Further control experiments were also performed to check whether merely the similar absorption of acridine-like compounds, rather than photobase effect, can lift photocatalytic performance. To this end, two structurally analogous molecules, anthracene, aminoacridine, are selected and added into the CD systems at pH 7. Anthracene is not photobasic. Although aminoacridine is photobasic, it has an inappropriate pK_a value where pK_a=10 and the pK_a^* is higher [189], which implies that it cannot abstract a proton from water at neutral pH. As shown in **Fig. 4.20**, neither of the two cases shows any enhancement in the hydrogen generation, confirming that the photobase effect is essential to the enhancement.

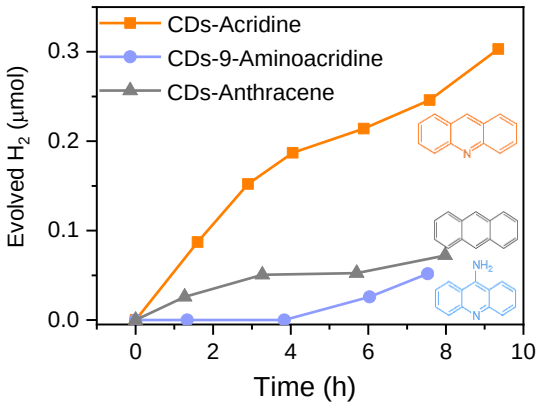

Figure 4.20 Comparison of photocatalytic performance of CD/acridine hybrid, anthracene (non-photobase) and 9-aminoacridine (photobase) with pK_a10.

Finally, it is meaningful and essential to investigate the source of the evolving hydrogen. Herein the DI water is replaced by heavy water (D_2O), and a photocatalytic experiment is conducted. A decrease in hydrogen generation rate by a factor of **1.43** was found. Therefore, a robust kinetic isotope effect is proved to exist. It is direct evidence that water, instead of CDs or acridine, is the proton source for the produced hydrogen [190].

In summary, this work demonstrates that the photobase effect, the photoinduced proton transfer, can be utilized in photocatalytic water splitting. After being excited, the photobasic molecule can abstract a proton from the solvent within 30 ps, as probed by transient absorption spectroscopy. This facilitates fast proton-coupled electron transfer, which can increase the overall photocatalytic reaction rates substantially. The photocatalytic control

experiments also confirm the importance of pyridinic nitrogen in the organic photocatalyst. As the photobasic moieties also exist as building blocks in many nitrogen-containing carbon materials, including CDs and carbon nitride, the photobasic effect may be involved in the photocatalytic reactions and may partially account for their success in the photocatalytic H_2 production. This work can open a new avenue for designing efficient organic materials-based photocatalysts.

Chapter 5 Intrinsically photobasic CDs for photocatalysis

Chapter 4 has shown that the protonation of organic molecules, known as photobases, can be manipulated by light. It was also shown that the photoinduced proton transfer in the model photobase, acridine, can occur very fast, within ~30 ps. The photocatalytic activity of the CD/photobase hybrid system has been dramatically improved. It is substantial progress towards a better understanding of metal-free organic photocatalyst applied to photocatalytic hydrogen generation. It confirms and underlines the importance of pyridinic nitrogen in organic functional materials used in photocatalysis, which was firstly found in carbon dots [120]. As the pyridinic nitrogen, or the photobasic moieties, can also exist in many organic materials, such as carbon nitride, it raises the question: could CDs be photobasic intrinsically? Could the photocatalytic activity come from the photobasic effect in CDs? It can provide a rational design of organic materials/molecule-based photocatalysts if it is the case.

We selected citric acid and urea, two classical precursors, for nitrogen-containing CD synthesis to validate this hypothesis. The photobase effect of the resulting sample has been identified and confirmed through steady-state absorption and PL spectroscopic measurement. The photoinduced proton transfer has been further verified using transient absorption spectroscopy, and the timescale of protonation has been determined. The application to photocatalytic water reaction has also been tested.

5.1 Identification of the photobase effect

In this work, two typical precursors, citric acid and urea, were selected as the precursors. The synthesis protocol is based on Kasprzyk *et al* [157] and is described in detail in **Section 3.1.2**. According to an earlier work in the group (Bhattacharyya *et al*.[120]), the amount of nitrogen-containing precursor is crucial to forming pyridinic nitrogen in the CDs, which is decisive to the photocatalytic activity [120]. Only a large ratio of nitrogen-containing precursor can lead to the formation of pyridinic nitrogen in CDs. In this work, three different molar ratios of urea to citric acid (3.1, 6.7 and 10.8) were selected to synthesize nitrogen-containing CDs. Here only the CDs resulting from the largest molar ratio (10.8) have been extensively investigated.

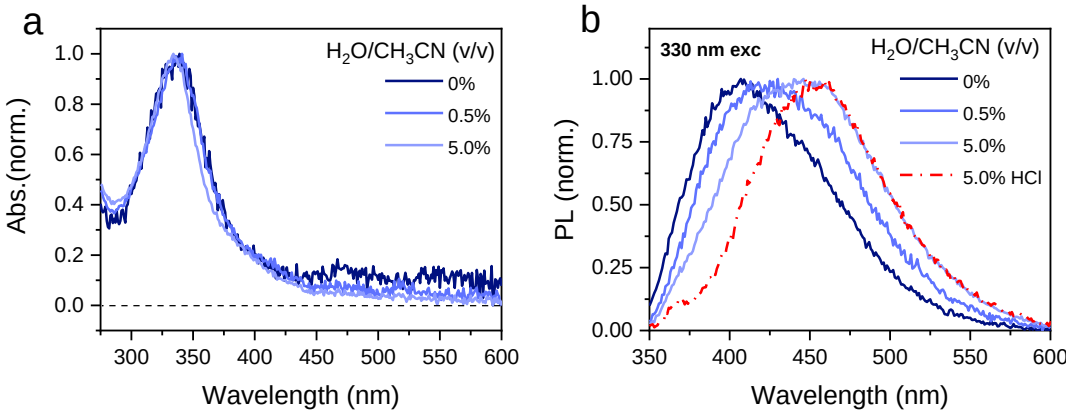

Figure 5.1 The normalized absorption spectra (a) and the photoluminescence spectra (b) of CDs in the different volume ratios of water in acetonitrile. The red curve in (b) is the PL spectrum of CDs in 5 vol% HCl. The excitation wavelength is 330 nm.

The method to identify the photobase effect in CDs is to compare the difference of both absorption and PL spectra with/without the presence of protic/proton donor in aprotic solvent, which has been discussed in detail in **Chapter 3.4**. In this case, water and acetonitrile are selected as the protic and aprotic solvents, respectively. Here we need to clarify that the reaction solvent is water. Nitrogen-containing CDs can probably be protonated in the ground state in water as CDs are miscible in water. Thus, the resulting fluorescence is likely to have contributions both from protonated and deprotonated species. To differentiate the contributions, the initial solvent of CDs solution was removed by evaporation under the flow of nitrogen and CDs were further redispersed in acetonitrile where CDs cannot be protonated. As our focus is photocatalytic water splitting, the main concern is whether CDs can abstract protons from water in the excited state, manifesting the photobasic character. Therefore, controlled amounts of water, from 0.5 vol% to 5 vol%, were added into acetonitrile. A tiny amount of water will not largely change the dielectric constant of the solvent that affects the relaxation process.

The normalized absorption and PL spectra of CDs in water/acetonitrile mixed solution are shown in **Fig. 5.1**. In general, there is sharp absorbance at 340 nm in the normalized absorption spectra albeit different ratio of water added and no substantial absorbance above 420 nm are observed. Neither the location nor the shape of the absorption spectra exhibits any significant change upon the addition of water to the acetonitrile solution of CDs. The noisy and tiny absorbance in the range of 450-600 nm in pure acetonitrile solution may be attributed to light scattering, which is reduced significantly upon the addition of even a tiny amount of water. It is reasonable as CDs have limited solubility in acetonitrile but are dispersed easily in water. The absorption spectra indicates that water addition does not affect the population of the ground states, which is expected for photobase effect. And it is necessary to identify how the proton donor affect the depopulation process.

In contrast, the PL spectra reveal a significant redshift upon increasing the concentration of water in the acetonitrile solution of CDs (**Fig. 5.1b**). The PL spectrum of CDs in pure acetonitrile unveils a broad PL emission in the region around 350-550 nm upon excitation at 330 nm. The non-protonated CDs show a governing PL peak at 400 nm. Upon adding an increasing amount of water (0.5 vol% to 5 vol%) that acts as a proton source, the peak position of the PL spectra gets redshifted and finally settle at 460 nm. The population process (absorption) is not altered by the presence of the proton donor, while the depopulation process (emission) of CDs is largely changed. The difference is caused by the photoinduced proton transfer in the excited state, which is the definition of the photobase effect. Thus, the newly emerging PL component at 460 nm stems from protonated CDs, indicating the nitrogen-containing CDs are intrinsically photobasic.

Additional evidence regarding the photobasic character of CDs comes from the PL spectrum in the presence of 5 vol% HCl in acetonitrile solution. In this case, CDs are expected to be protonated already in the ground state. CDs are found to emit preliminarily at 460 nm due to protonation, as shown in red dashed curve in **Fig. 5.1b**. The normalized PL spectrum of CDs in the 5 vol% water/acetonitrile mixture appears remarkably resembles that of 5 vol% HCl/acetonitrile solution, especially in the red region of the spectra (starting from 450 nm, **Fig. 5.1b**). It is the direct evidence that there is a contribution from the protonated species to the PL of CDs in 5 vol% water/ acetonitrile solution.

The intrinsically photobasic character of CDs is further supported by photoluminescence excitation (PLE) measurements. To identify the origin of the emission around 460 nm, we probed the PLE at 500 nm at different water/acetonitrile mixtures, where the emission from protonated species is anticipated to constitute a larger ratio. As shown in **Fig. 5.2**, the PLE spectrum monitored at 500 nm has a single peak at 340 nm, overlapping the absorption spectrum (red curve) quite well. Interestingly, a new shoulder shows up in the PLE spectrum of CDs in 5 vol% water solution in the range between 360 to 420 nm. However, the shoulder is absent in the PLE spectrum in pure acetonitrile or in the absorption spectrum. It may indicate that the new shoulder is due to the protonation in the excited state. For comparation, the PLE spectrum detected at 500 nm of the acidified CDs (green curve) is also plotted and compared. A more dominant shoulder appears in the same range as in 5

vol% water (from 360 to 460 nm), which is due to the protonated species. This supports the claim that CDs are protonated in the excited state in water.

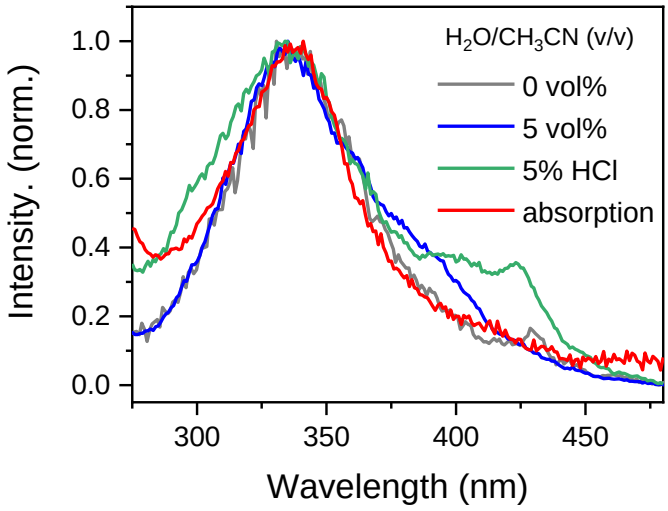

Figure 5.2 The photoluminescence excitation spectra (PLE, λ_{em} = 500 nm) of CDs in two different amounts (0 vol% and 5 vol%) of water/acetonitrile (H_2O/acetonitrile, v/v) mixture. The corresponding PLE spectrum of the acidified CDs is shown in green. CH_3CN is the formula acetonitrile. The absorption spectrum in the presence of 5 vol% water in the acetonitrile solution is plotted in red for comparison.

Now that the photobase effect has been identified in CDs, how to characterize the capability of attracting protons? The pK_a value can be viewed as a quantitative measurement of the affinity to proton in solution [191]. The difference value, ΔpK_a, between the pK_a in the ground state and pK_a^* in the excited state, can present the difference in affinity to proton, and can be calculated by **Eq 2.22**. The equation is rewritten as follows.

$$\Delta pK_a = pK_a^* - pK_a = 0.00209(\nu_B - \nu_{BH+})/\text{cm}^{-1}$$

The ΔpK_a can be determined by the wavenumbers of PL peak location of non-protonated CDs and protonated CDs, and the resulting value is 6.8 units. The result indicates that the affinity to proton of the CDs has increased $10^{6.8}$ times in the excited state. The significant increment in the proton affinity can explain why the excited CDs can be protonated in water.

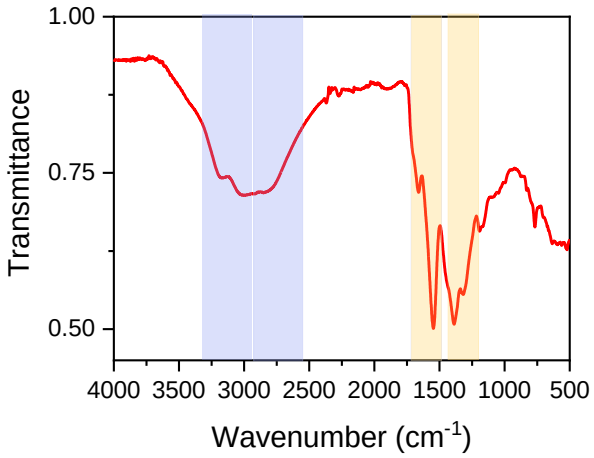

Figure 5.3 FTIR spectra of the photobasic CDs

CDs were further characterized by Fourier-transformed infrared spectroscopy (FTIR) in the range between 500 to 4000 cm^{-1}. The spectrum in **Fig. 5.3** reveals that there exists a lot of functional groups such as amino (3250 cm^{-1}), phenol (1377 cm^{-1}), functioning as typical electron donors [192]. Meanwhile, there are also electron acceptors present in the CDs, such as conjugated ketone (1676 cm^{-1}), nitro (1542 cm^{-1}) [193, 194]. Furthermore, the weak stretching vibrations of pyridinic nitrogen (C-N=) in FTIR is also observed (~1420-1470 cm^{-2}) [120]. According to **Section 2.3.4**, intramolecular charge transfer can occur in the excited conjugated molecules with electron donor and electron acceptors [131]. In this case, the electron acceptor group, including pyridinic nitrogen, can accept an additional electron in the excited state to attract the proton and even abstract protons from water.

Therefore, the CDs synthesized from the precursors citric acid and urea have been identified to be photobasic, which can abstract protons from water in the excited state. In the following section, the timescale of photoinduced protonation is extracted from ultrafast spectroscopy.

5.2 Protonation dynamics in CDs

After identifying the photobasic character of CDs, femtosecond transient absorption spectroscopy (TAS) was employed to investigate the excited state dynamics and to estimate the timescale of proton transfer in the excited state. Two solvents, acetonitrile and water, were utilized in differentiating the features in the TAS spectra: non-protonated in the excited state, and protonated in the excited state. Herein CDs were excited at 330 nm with a 100 fs pump pulse, and the differential absorption spectra were acquired with a time-delayed white light probe pulse. The TAS spectra of CDs in acetonitrile solution where CDs cannot be protonated consists of a broad and structureless excited state absorption (ESA) in the entire probe region (between 350-700 nm) (**Fig. 5.4a**). Even at a longer delay time, no other features appear in the spectra. However, upon addition of a minor amount of water (10 vol%, as shown in **Fig. 5.4b**) in the acetonitrile solution, the TAS spectra of CDs change dramatically. At a very early time (<200 fs), the TAS spectra resemble the broad ESA in pure acetonitrile solution. Surprisingly, a strong negative ΔOD signal emerges between 400 to 550 nm on top of the ESA signal at a later time. Altogether, three regions of interest are observed upon the addition of 10 vol% water: two ESA features (<400 nm and >500 nm) and one negative absorption in the range from 400 to 550 nm.

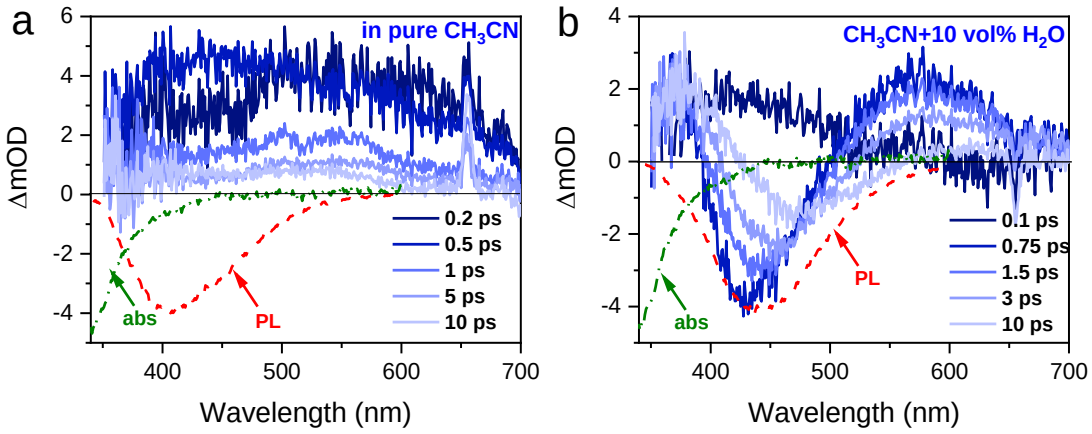

Figure 5.4 Transient absorption spectra of CDs after excitation at 330 nm, a) in pure acetonitrile and b) in the presence of 10 vol% water in acetonitrile solution at the selected time interval between 0.1 to 10 ps, respectively. The PL and absorption spectrum is also plotted in a red short-dashed and green-dotted line, respectively, for comparison. CH_3CN is short for acetonitrile.

Let us investigate the ESA first. The broad ESA observed in pure acetonitrile in a sample transparent region indicates the transient absorption to higher excited states caused by the photoinduced carriers by absorbing the time-delayed probe pulse, in agreement with literature on graphene dot and carbon dots [195]. It is of great importance to trace the origin of the emerging negative absorption after water addition. The steady-state absorption spectrum is compared to the negative differential absorption at first. The absorption

spectrum of CDs has a maximum at 340 nm, and the absorption cross-section is very low for the wavelength above 400 nm, irrespective of the water concentration (see green dash-dots in **Fig. 5.4b**). There is negligible overlap between the linear absorption spectrum and the negative feature in the TAS spectra, as shown in **Fig. 5.4b**. Meanwhile, the PL spectrum of CDs in the water/acetonitrile solvent overlaps nicely with the negative ΔA signal between 400 to 550 nm. Recall that the absorption signature of CDs remains unaltered in water/acetonitrile solvents, here we tentatively ascribe the negative ΔOD signal in such a sample transparent region to stimulated emission (SE). In particular, the negative ΔOD signal at the early time has significant overlap with the blue side of the PL spectrum while it has more overlap with the red side of the PL at a later time (~10 ps).

Further evidence of the SE comes from the overlap between the steady-state PL and the difference spectrum derived from TAS spectra (at early time ~0.5 ps) in the presence of 10 vol% water in acetonitrile and pure acetonitrile solution. The difference spectrum with the corresponding PL spectrum sits exactly on top of each other, as shown in **Fig. 5.5**.

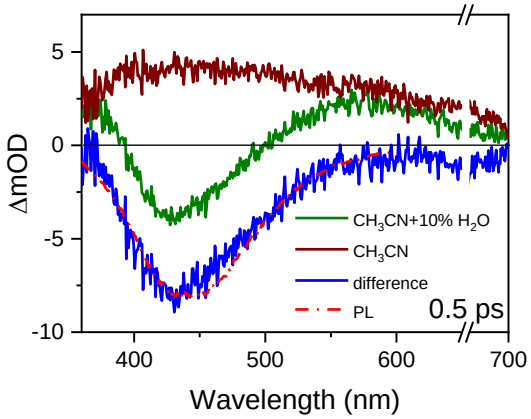

Figure 5.5 TAS spectra at 0.5 ps (a) in 10 vol% water/acetonitrile mixture and pure acetonitrile solution, along with the difference between the two (in blue line) are shown. The PL spectrum is also plotted in a red dot-dashed line for comparison.

The observation of the stimulated emission can be explained by the four-level photobasic scheme depicted in **Fig. 5.6** After absorption of photons, the photobasic CDs are excited and have much stronger affinity to protons. The CDs can get protonated in the excited state (S_1') where CDs can be stimulated to emit excess energy. As the protonated ground state (S_0') is energetically higher than the non-protonated ground state (S_0), a rapid relaxation from S_0' to S_0 can lead to a negligible population of S_0'. Therefore, a population inversion can be formed (S_1') with respect to protonated ground state (S_0'). Thus, the stimulated emission from S_1' to S_0' can occur.

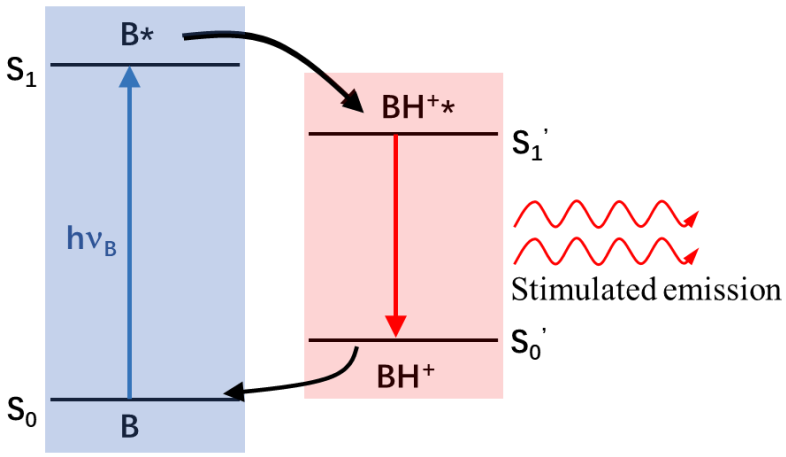

Figure 5.6 The energy diagram of photoinduced proton transfer. After photon absorption, the photobasic CDs would abstract a proton in the excited state and become protonated.

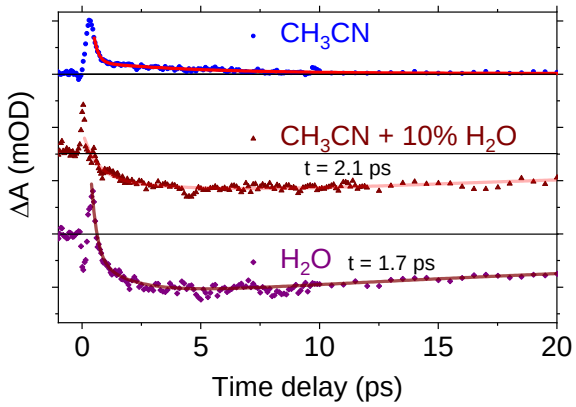

Figure 5.7. Comparison of the transient traces at 490 nm for pure acetonitrile (CH_3CN), 10 vol% H_2O in acetonitrile and pure H_2O solution.

The presence of stimulated emission indicates that the transition between S_1 and S_1' is fast. It is essential to determine the timescale of the transition, also called photoinduced proton transfer. It is an important parameter in photocatalysis, which can be determined by the TAS spectra. The easiest method is to inspect the appearance time of the SE signal. Due to the substantial overlap between the SE and the ESA signals, it is not easy to extract the protonation time. To reduce the contribution from ESA features, SE transients at 490 nm (**Fig. 5.7**) were plotted where the contribution of ESA (both <400 nm and >500 nm) is minimal, in both 10 vol% water/acetonitrile mixture and pure water. The transient in pure acetonitrile solution at 490 nm is also compared in **Fig. 5.7** and consists of an ultrafast ~200 fs and a 4 ps components. The onset growth of the SE signal can be characterized by 2.1 ps and 1.7 ps for 10 vol% water/acetonitrile and pure water, respectively. Recall that the SE

signal appears due to the formation of the protonated CDs, therefore, the growth in the SE signal corresponds to the timescale of the excited-state proton transfer in the excited state. The protonation time in the presence of pure water (1.7 ps), as expected, is faster compared to 10 vol% water/acetonitrile mixture (2.1 ps). However, the difference in protonation timescale of pure water and 10 vol% water is small, probably due to the solubility difference of CDs in acetonitrile and water. As mentioned before, CDs have low solubility in acetonitrile. The water added is expected to cover the surface of CDs to form hydrogen bonding, giving equally easy access to protonation as that in pure water.

What is important to note is that the timescale of photoinduced protonation in the present work is one order of magnitude faster than acridine (~30 ps) (in **Chapter 4**) [103], where an extrinsic photobasic molecule was utilized to sensitize the CDs. The protonation timescale of the photobasic CDs is also much faster than other molecules, such as quinoline [142, 143], aminoanthraquinones[141], probably due to the strong electron donors and polycyclic aromatic hydrocarbon built into the CD structure. Such an ultrafast protonation process in CDs that are intrinsically photobasic can potentially apply in photocatalytic H_2 generation, and in opto-protonics. It suggests new design pathways to prepare next generations of efficient photocatalysts that exploit the the ability to control the proton transport with light.

5.3 Analogue to excimer emission

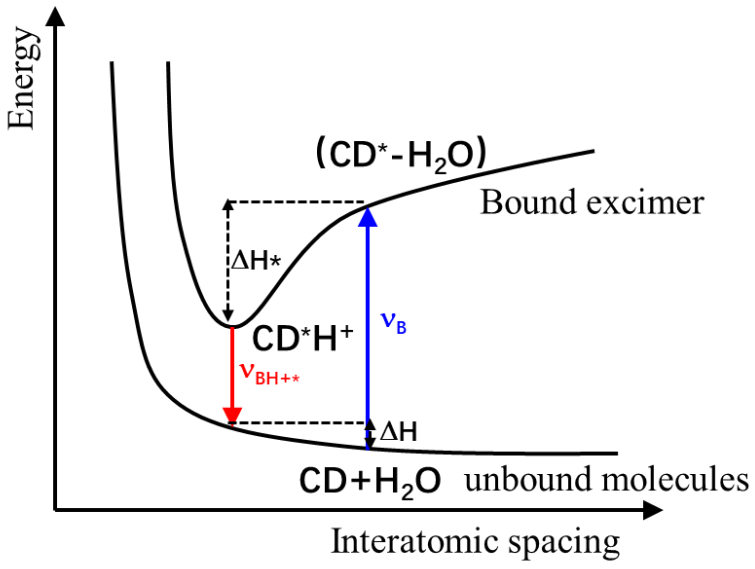

Figure 5.8 The scheme of excimer formation.

The four-level photobasic scheme (**Fig. 5.6**) reminds us of the excimer formation, and the corresponding scheme is also shown (**Fig. 5.8**). Excimers are formed when an excited aromatic molecule interacts with a second molecule in the ground state [196]. It indicates that the photoinduced protonation process in CDs can also be regarded as the excimer

formation. In the ground state, only weak hydrogen bonding exists between CDs and water molecules. CDs and protons have a considerable intermolecular distance. After CDs absorb a photon, the resonance interaction can be large enough to cause the excited CDs and water molecule to reorient, and the resulting distance between CDs and water molecule becomes smaller. Meanwhile, the excited CDs have a larger affinity to proton, which can abstract proton from water, thereby forming an excimer (the protonated CDs). Due to the attractive interaction, the potential energy in the excited state is shifted, and emission occurs at an intermolecular distance where the ground state potential is non-bonding and repulsive [196]. Meanwhile, a population inversion with respect to the ground state of CDs can be formed in the excimer. Incident photons can stimulate electrons back to the ground state radiatively, appearing as SE. Interestingly, the observation of SE feature in nitrogen-derived CDs can be interpreted in terms of 4-level excimer lasing. It points to an extension of the application of CDs to the excimer laser.

5.4 Photobasic CDs for photocatalytic water splitting

As discussed in **Chapter 2** and **Chapter 4**, the proton transfer is a rate-determining step to photocatalytic water splitting. The photobasic CDs synthesized from citric acid and urea can abstract protons from water molecules in an ultrafast timescale (~ 2 ps), exhibiting the great potential of utilization in photocatalytic water splitting.

No noble metal or metal cation was added in this experiment to eliminate the effects of a co-catalyst. At the same time, to exclude the possibility of hydrogen generation from methanol, sodium sulfite, Na_2SO_3, instead of methanol, was selected as the hole scavenger. The hydrogen generation rate is shown in **Fig. 5.9**. In 8.5 hours, CDs could produce ~100 μmol hydrogen per gram, and the average hydrogen rate was ~12.1 μmol/g·h. In the photocatalytic control experiment where CDs are not dispersed, no hydrogen was detected. It evidences that CDs are necessary for the photocatalytic reaction and can reduce water into hydrogen without co-catalyst. Although the hydrogen generation rate is low compared to those where co-catalyst is involved, the photocatalytic activity has already outperformed some classical photocatalyst, such as TiO_2 without co-catalyst [197]. Therefore, the photobasic CDs, as one kind of organic materials, have proven to be an extraordinary photocatalyst candidate.

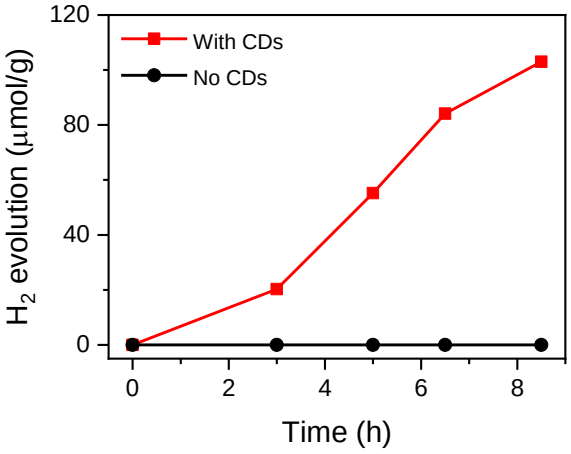

Figure 5.9 The time-dependent photocatalytic hydrogen generation in the presence of or absence of CDs

5.4.1 pH-dependence

Recall that the pH of the solvent can control the photobase effect in **Chapter 4**. To further prove the photobase effect in photocatalytic activity, CDs were dispersed in a water solution with three pH values, pH 7, pH 9 and pH 15. Although the exact pK_a^* value in the excited state cannot be directly obtained, it can be roughly estimated. As CDs can abstract protons at pH 7, and the ΔpK_a is calculated to be 6.8 units, the pK_a^* ($= pK_a + \Delta pK_a$) value should

be smaller than 14. Herein a sufficiently high pH value, 15, was selected to create the environment where the CDs cannot undergo excited-state protonation. The pH-dependent photocatalytic performances are shown in **Fig. 5.10**.

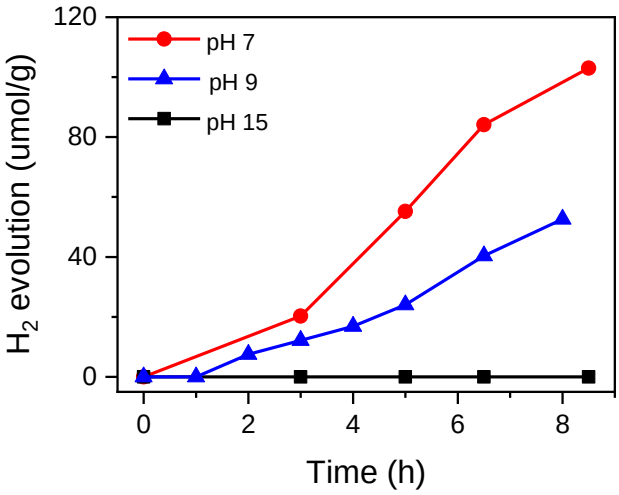

Figure 5.10 The photocatalytic performance at different pH.

As expected, the nitrogen-containing CDs cannot reduce water at a high pH value (pH 15) when the photobase effect was "switched off" due to the blocked access to the protons. It reemphasizes the importance of proton concentration in photocatalytic water splitting. The photocatalytic performance is contrary to the case of CdS [198, 199] where the nanostructures exhibit extraordinary high photocatalytic activity at high pH. The exceptional hydrogen performance of CdS in high pH solution is due to the efficient extraction of holes by hydroxyl anions, prolonging the lifetime of the photoinduced electrons. Another reason for the "switched off" photocatalytic performance is likely to be the instability caused by hydroxyl radical.

The photocatalytic activity is observed only at two pH values, pH 7 and pH 9, where photobase effect manifests itself. Therefore, an easier access to proton due to a lower pH will grant CDs more enhanced photocatalytic performance, as CDs have a higher hydrogen generation rate at pH 7 than at pH 9.

5.4.2 Dependence on the ratio of urea/citric acid

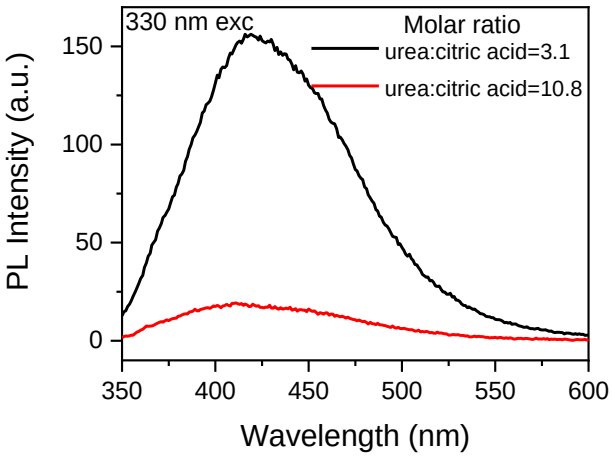

Figure 5.11 The PL spectra of CDs resulting from two different molar ratios (urea to citric acid) excited at 330 nm. The measurement was conducted in pure acetonitrile.

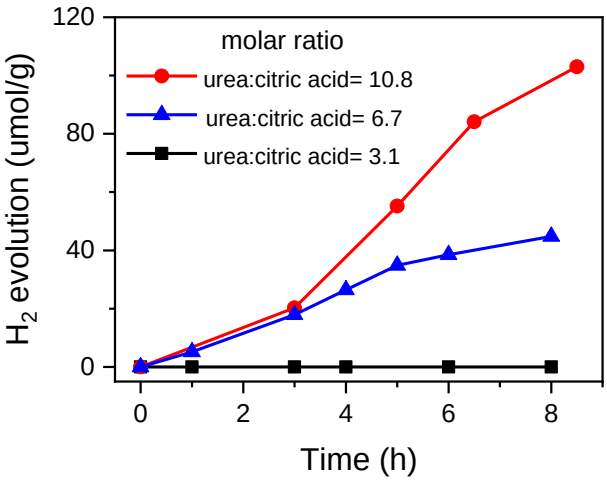

Figure 5.12 The photocatalytic performances of CDs resulting from three different molar ratios (3.1, 6.7 and 10.8).

Inspired by Bhattacharyya's work of controlling the nitrogen position by the amount of nitrogen in the precursor [120], another control experiment was set to further evidence the photobase effect in photocatalytic reactions. The sample that the previous discussion is based on is derived from urea and citric acid with a molar ratio of 10.8:1, where urea mass was 1.35 g. As concluded in Bhattacharyya's work, a higher concentration of nitrogen-containing urea will lead to the formation of pyridinic nitrogen at the edge sites of the aromatic domains [120]. Therefore, the other two kinds of CDs were synthesized with two smaller molar ratios (urea to citric acid): 6.7 and 3.1. As revealed in **Fig. 5.11**, the PL

spectrum of CDs resulting from molar ratio 3.1 has a much stronger intensity than that from molar ratio 10.8. It shows that a lower amount of nitrogen precursor will make the CDs more emissive. A higher ratio probably endows CDs with more pyridinic nitrogen, which still needs to be evidenced by further characterization. The photocatalytic performances of the three kinds of CDs are tested, compared, and the results are illustrated in **Fig. 5.12**. CDs with a higher ratio exhibited higher photocatalytic activity, while emissive CDs (molar ratio 3.1) showed no photocatalytic activity. The results can further support the conclusion that the nitrogen positions in organic materials are essential to photocatalytic water splitting.

In summary, the CDs derived from two commonly used precursors, citric acid and urea, have been proven to be photobasic. The photobasic CDs can abstract proton from water in the excited state, and the process can also be viewed as excimer formation. The stimulated emission in CDs was also observed and identified in transient absorption spectroscopy, evidencing that CDs can be applied to the excimer laser. Based on the ultrafast spectroscopy, the timescale of protonation is around 2 ps. The ultrafast protonation time makes the photobasic CDs an excellent photocatalyst, producing hydrogen without co-catalyst efficiently.

Chapter 6 Using triplet states for photocatalysis

The efficiency of photocatalytic reactions is mainly limited by the timescale discrepancy between short lifetime (~ns) and proton diffusion (~μs) [11]. The majority of the photogenerated electrons cannot be utilized in the hydrogen generation [16]. Although **Section 2.1.3** have illustrated the developed methods to enhance charge transfer to achieve longer lifetime, the timescale mismatch remains an issue. Another solution is to utilize the triplet states with a much longer lifetime, typically >1 μs. The lifetime timescale overlaps the timescale of proton diffusion, which indicates triplet states are plausible to use for photocatalysis. To achieve this goal, increasing the magnitude of spin orbit coupling is the key.

In this chapter, metal-free phosphorescent CDs were synthesized. The quantum yield of triplet states can be controlled by an ISC inhibitor. As the triplet states can be quenched heavily in water, the photocatalytic activity is tested in methanol, where phosphorescence can still be detected. The photocatalytic performance is also measured.

6.1 Evidence of long-lifetime triplet states

Prior to identify whether triplet states can be utilized in photocatalytic water splitting, synthesizing phosphorescent materials is the first step. Heavy atoms, generally platinum and iridium, can increase the magnitude of spin-orbit coupling and are generally included to increase intersystem crossing and achieve a higher quantum yield of phosphoscreens. The heavy atom effect is also explained in **Section 2.3.3**. However, the heavy metal can also function as a co-catalyst that can dramatically improve the photocatalytic performance [200, 201]. Therefore, to exclude the metal's effects on photocatalytic activity, metal-free phosphorescent materials are requested. As discussed in **Chapter 2**, elements with non-bonding electrons, such as nitrogen and oxygen, are mandatory to be included to enhance the magnitude of spin-orbit coupling. Herein, two chemicals with high ratios of oxygen and nitrogen element, citric acid and urea, were chosen as precursors [159]. Besides that, acrylamide was also included because it can increase the conjugation length of CDs. The experiment details have been explained in **Section 3.1.3**.

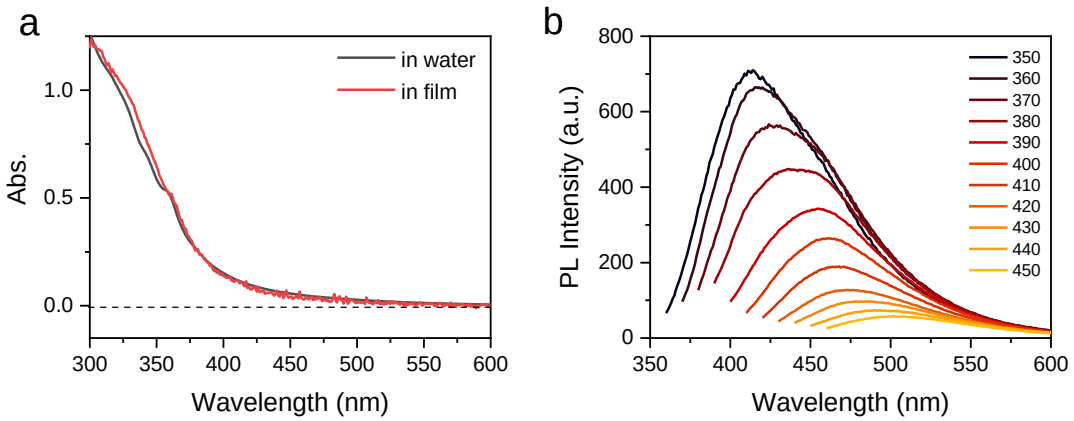

Figure 6.1 The absorption spectra of CDs (a) in water and dispersed in polyvinyl alcohol film, and PL spectra (b) at different excitation wavelength in water.

The resulting CDs are yellowish and highly soluble in water, and the absorption spectrum is shown in **Fig. 6.1a.** CDs absorb light strongly in the UV rang with a tail extending up to 600 nm. The absorption onset bands around 300 nm results from the $\pi \rightarrow \pi^*$ and $n \rightarrow \pi^*$ transition of the chromophores (e.g., C=O, -NH_2, and C=N-C). Meanwhile, the typical excitation wavelength dependent fluorescence in CDs has also been observed (**Fig. 6.1b**). However, only prompt fluorescence is detected in the aqueous solution, proved by the lifetime measurement (**Fig. 6.2**). The PL decay shows that the lifetime is short, around 8 ns, in the typical lifetime range of singlet state. However, no phosphorescence is detected in water. The absence of or negligible phosphorescence in a solvent is commonly encountered, as the slow radiative recombination process is outcompeted by a faster nonradiative relaxation. A range of external stimuli, including oxygen, impurities and temperature, can quench the triplet states [202, 203]. Generally, covalent integration of samples into the polymer matrix remains the most appealing approach, as it can suppress the nonradiative

relaxation by intermolecular stacking with restricted vibration and rotation [204]. The phosphors are also shielded from the external quenchers, such as oxygen and moisture. Thus, phosphorescence with a stronger intensity can be expected. Herein, polymer polyvinyl alcohol (PVA) is selected, and CDs are encapsulated in the polymer matrix. As expected, the strong phosphorescence appears in the film and is still visible after several seconds even by naked eyes, which indicates the presence of long lifetime triplet states. The phosphorescence decay is shown in **Fig. 6.3**.

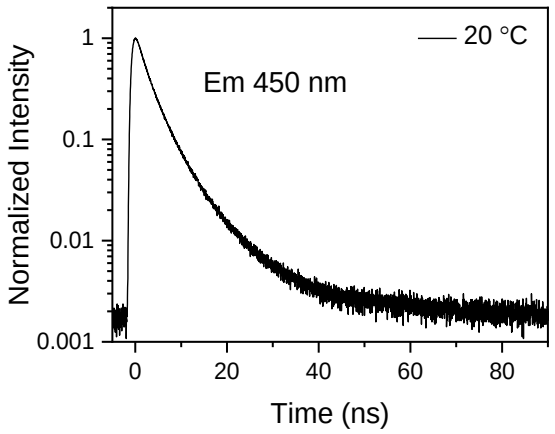

Figure 6.2 The PL decay of CDs at emission wavelength 450 nm in a water solution (excitation wavelength: 350 nm).

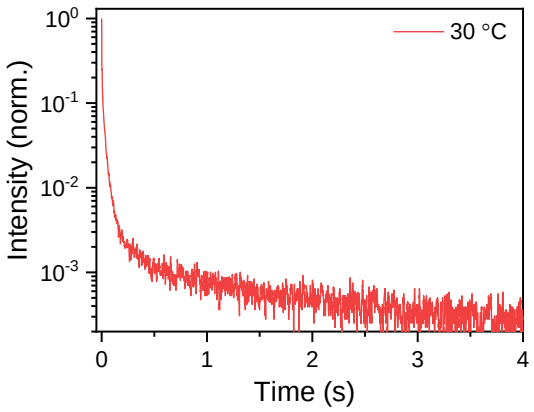

Figure 6.3 The semi-log plot of phosphorescence decay at the emission wavelength 520 nm (excitation wavelength: 460 nm).

The decay trace of phosphorescence can provide more information about the deactivation process, and the results are shown in the semi-log plot (**Fig. 6.3**). There are two components observed, a faster one (~ms) and a slower one (~s). Thus, the decay can be fitted with a biexponential function with a lifetime 28 ms (99%) and 1.03 s (1%), respectively. More information can be derived regarding the timescale of each lifetime component. As discussed in **Section 2.3.5**, because the transition from π^* to π is forbidden in triplet

states because of no change in the orbital angular momentum, the T_1 state with a $^3(\pi, \pi^*)$ configuration usually has an extremely slow decay rate and a relatively small quantum yield. The typical timescale is more than 1 s. While the transition π^* to n is allowed in triplet states due to spin-orbit coupling, the T_1 state with a $^3(n, \pi^*)$ configuration usually has a shorter lifetime and relatively larger quantum yield. The typical lifetime is less than 10 ms. Therefore, it can be inferred that the triplet state (T_1) has a dominant (99.0%) (n, π^*) configuration mixed with a tiny ratio (1%) of a (π, π^*) configuration.

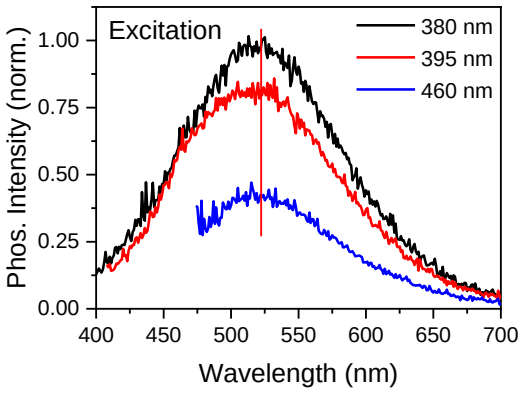

Figure 6.4 The phosphorescence spectra of CDs with three different excitation wavelength (380, 395 and 460 nm).

As shown in **Fig. 6.1,** the UV-vis absorption spectrum of CDs in the matrix is almost identical to that in the water solvent, and no new peak is observed. To select an appropriate excitation wavelength, three excitation wavelengths, 380 nm, 395 nm, and 460 nm, are selected. The location and shape of phosphorescence spectra are almost independent of the excitation wavelength, as shown in **Fig. 6.4**. The excitation wavelength independent phosphorescence indicates the photoinduced electron will relax to S_1 and spin flip to the same triplet state. In this work, the wavelength 460 nm is selected as the excitation wavelength as a tradeoff between resonate energy above S_1 and a relatively large absorption coefficient.

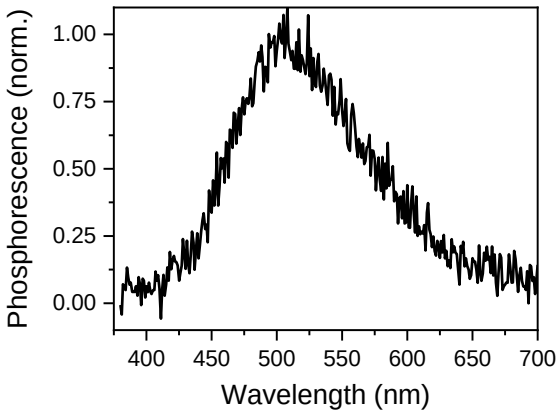

Figure 6.5 Weak phosphorescence of CDs in methanol with the excitation wavelength 350 nm.

What is the next is to check whether triplet states can be utilized in photocatalysis. Recall that the triplet states are quenched heavily in water, accordingly barely any phosphorescence can be observed in water. Thus, an aqueous system is not the ideal choice for the investigation of triplet states in photocatalytic reactions. Methanol is selected instead as both the solvent and proton source. As shown in **Fig. 6.5**, weak phosphorescence of CDs can still be detected in methanol solvent, indicating the triplet states can be reserved in methanol. The phosphorescence peak location is around 505 nm. It blueshifts 15 nm compared to that in PVA film, as methanol has a larger dielectric constant.

6.2 Triplet states on photocatalysis

No heavy metal nanoparticle or metal cations is introduced in the photocatalytic solution. As CDs are not soluble in methanol, 10 vol% aminoethanol has been added to enhance the dispersion in methanol. **Fig. 6.6** shows that the CDs can convert methanol into hydrogen at room temperature and possess a high and steady photocatalytic activity. In a control experiment where no CDs were added, no hydrogen production has been detected, indicating CDs are necessary to the photocatalytic methanol-reforming. There is no hydrogen detected in pure aminoethanol without methanol, either, indicating the highly polar solvent only serves to disperse CDs in methanol.

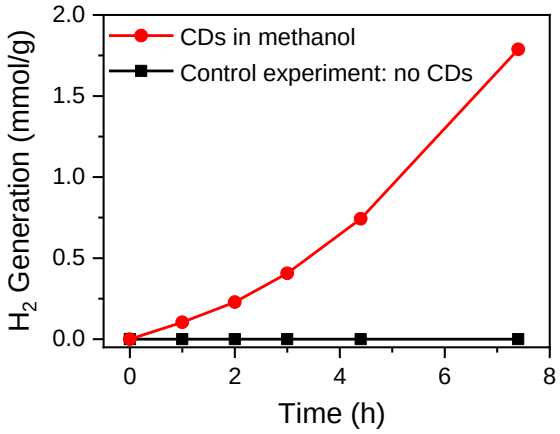

Figure 6.6 Time-dependent hydrogen generation of CDs in methanol.

6.2.1 Effects of the ISC inhibitor on triplet states

Although the phosphorescent CDs are photocatalytic, it is intriguing to know whether the triplet states contribute to photocatalytic performance. As both the singlet and triplet states are generated after the absorption of photons, it is necessary to design a control experiment to identify their contributions to the photocatalytic performance.

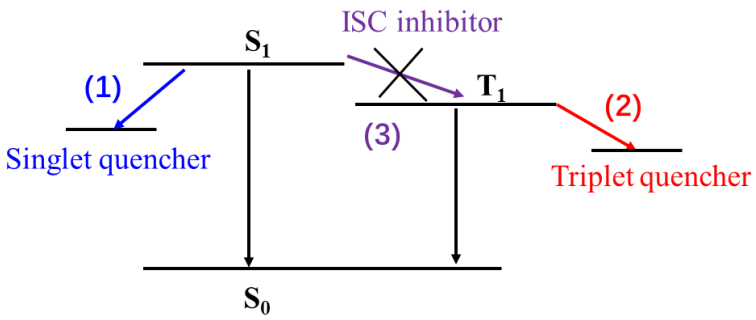

Scheme 6.1 The process (1) and (2) indicates that singlet and triplet states are quenched by a singlet quencher and a triplet quencher, respectively. Process (3) denotes the ISC is quenched by an ISC inhibitor.

The easiest way is to introduce a singlet or triplet quencher, as shown in **Scheme 6.1**. As the absorption coefficient of the transition $S_0 \rightarrow T_1$ usually is extremely small, the limited number of triplet states generated directly from the ground state absorption cannot account for photocatalysis. The origin of triplet states is mainly due to intersystem crossing from the singlet state. If the singlet quencher is introduced (**process (1)** in **Scheme 6.1**), both singlet and triplet states are expected to be quenched dramatically. The decline in photocatalytic activity cannot be tracked back to the specific source. Therefore, singlet quenchers are not the ideal. Regarding the triplet quencher (**process (2)** in **Scheme 6.1**), the typical examples are oxygen [196] and butadiene [126]. Singlet oxygen is produced during the triplet quenching by triplet oxygen via Dexter energy transfer. The singlet oxygen is so reactive that it attacks the π bond, detrimental to the photostability. Butadiene, a non-polar molecule, is insoluble in polar solvents, resulting in a limited quenching effect on the triplet states. Therefore, neither singlet nor triplet quenchers are suitable for the investigation of applying triplet states in photocatalysis.

In this work, an ISC inhibitor is introduced (**process (3)** in **Scheme 6.1**), which can reduce the quantum yield of triplet states. Water is one ideal ISC inhibitor as it is miscible in methanol and photostable. As previously discussed in **Section 2.3.5**, a large magnitude of spin-orbit coupling is mandatory for an efficient intersystem crossing. Water can form hydrogen bonding with N/O atoms in CDs in the ground state, and the density of non-pair electrons will be reduced, detrimental to the spin-orbit coupling and ISC. Accordingly, the quantum yield of triplet states can be controlled by water addition. As a small ratio of water in methanol will not change the polarity, the fluorescence is not expected to be largely affected.

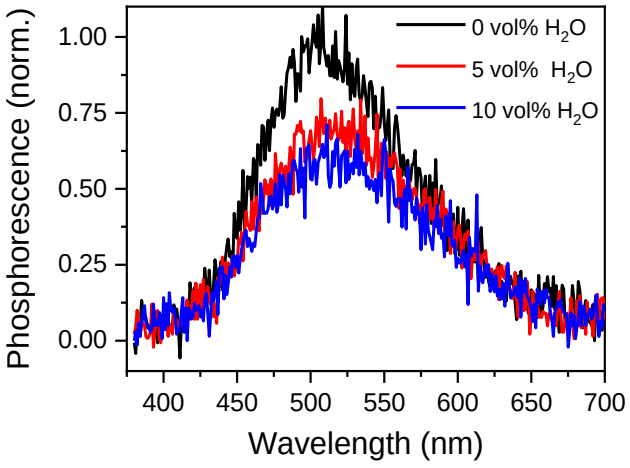

Figure.6.7 The CDs phosphorescence is quenched with increasing volume ratio of water into methanol.

Herein different amounts of water were added into the methanol to control the quantum yield of triplet states. No more than 10 vol% water was added into the methanol, and the dielectric constants of the solvent can be regarded as the same. The intensity of the phosphorescence can be regarded as an indicator of the quantum yield of the triplet states, as nonradiative recombination is usually much faster. Control experiments with two different amounts of water concentration, 5 vol%, and 10 vol%, were done. The corresponding phosphorescence spectra are shown in **Fig. 6.7**. It shows that, as expected, the phosphorescence intensity has decreased as more water was added.

6.2.2 Effects of the ISC inhibitor on singlet states

It is also necessary to check how the singlet states change with water addition, and the corresponding results are shown in **Fig. 6.8a**. There is almost no difference in the spectrum shape or intensity of the fluorescence spectrum, no matter the amount of water added into the methanol. After 10 vol% water addition, a slight increase in the fluorescence intensity is observed, probably due to the destabilization of the (n, π^*) singlet state caused by the hydrogen bonding. The hydrogen bond caused emission change is due to the slow decay of the $^1(n, \pi^*)$ singlet state. The singlet state with a (n, π^*) configuration can even be destabilized and possibly change their position relative to the (π, π^*) state [205], making CDs more emissive (See **Section 2.3.2**). Moreover, the fluorescence decay time of CDs in the water/methanol mixture is not affected by the water concentration, either, as shown in **Fig. 6.8b**.

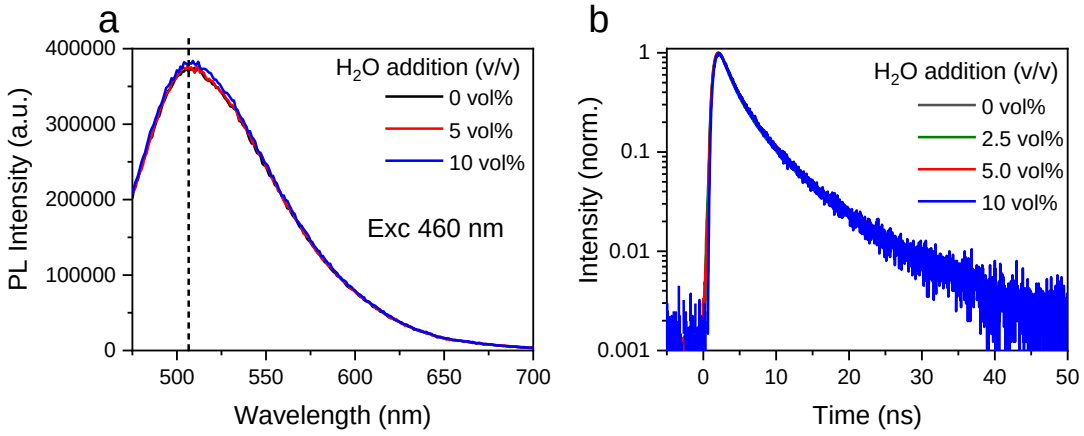

Figure.6.8 The fluorescence spectra a) with excitation wavelength 460 nm and the PL decay at 510 nm b) in different methanol/water mixture.

Therefore, the ISC inhibitor does not affect the deactivation process of singlet states, while the quantum yield of triplet states is controllable by the ISC inhibitor.

6.2.3 Effects of the ISC inhibitor on photocatalysis

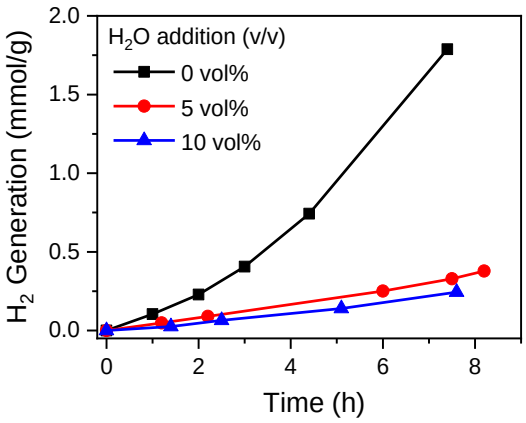

Figure.6.9 The time-dependent photocatalytic methanol-reforming with different amount of water addition (in neutral pH).

The effects of the ISC inhibitor on the photocatalytic activities of methanol-reforming are also investigated, and the results are shown in **Fig. 6.9**. In pure methanol, the hydrogen generation rate is 0.24 mmol/g·h. With even 5 vol% water addition, the hydrogen generation rate is dramatically reduced to 0.046 mmol/g·h. With a higher amount of water addition, the hydrogen production rate is further reduced to 0.032 mmol/g·h. The reduction trend correlates quite well with the decline in the intensity of phosphorescence, an indicator of the quantum yield of triplet states. When the ISC inhibitor ratio was increased from 5 vol% to 10 vol%, a slight decrease in phosphorescence was also consistent with the tiny drop of hydrogen generation rate. At the same time, recalling the fluorescence spectrum or the lifetime of singlet state is not even changed by increasing the water ratio in the water/methanol mixture. It may indicate that the triplet states can be used in photocatalytic activity.

From the discussion of effects of ISC inhibitor on water ratio-dependent photocatalytic activity and change of the fluorescence and phosphorescence, it is reasonable to relate the triplet states with photocatalytic activity. As inferred from the deconvolution of the phosphorescence decay, electrons from the triplet state with $^3(n, \pi^*)$ configuration account for 99%. It indicates that the photocatalytic methanol-reforming is probably related to triplet states with $^3(n, \pi^*)$ configuration.

6.3 Heavy atom effect

Based on previous analysis, the photocatalytic activity may correlate with triplet states. More control experiments and data are needed to evidence that long-lifetime triplet states could be used for photocatalytic reactions. One control experiment is designed to show the effects of triplet states in photocatalysis indirectly. Here the heavy atom effect is utilized in photocatalytic reactions. As detailed in **Chapter 2**, heavy atoms can enhance the magnitude of spin-orbit coupling and achieve a higher quantum yield of triplet states. Non-metal anion (Cl^-, Br^-), instead of metal cation, was selected and introduced to the CDs solution (same CDs as **Chapter 4**). The PL intensity, as expected, is found quenched with an increasing amount of NaCl/KBr (both with same molar concentration), as shown in **Fig. 6.10a,b**. One explanation is due to the enhanced intersystem crossing where the heavy-atom effect manifests itself. Moreover, the PL of CDs is quenched more heavily by Br anion addition. It can be explained by the fact that Br atom has a larger atomic number, inducing a more efficient ISC.

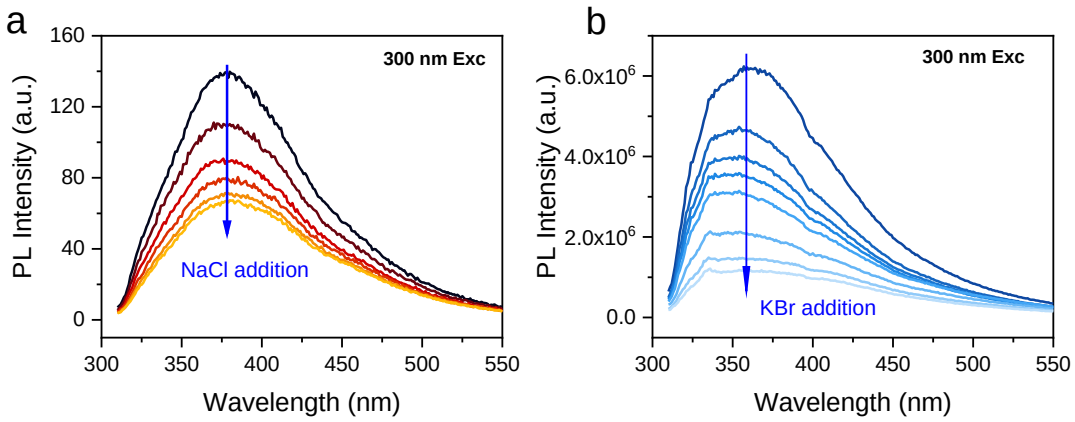

Figure 6.10 The fluorescence spectra of CDs in water solution added with increasing amounts of NaCl (a) and KBr (b). The spectra in (a) and (b) are obtained from Cary Eclipse Spectrometer and Horiba Spectrometer, respectively.

The photocatalytic performance of CDs is further characterized. Firstly, aqueous CDs solution was mixed with same volume of 0.1 M NaCl or KBr solution. Their photocatalytic activity has increased 9 and 23 times for Cl and Br anions addition, respectively (**Fig. 6.11a**). The large photocatalytic enhancement is consistent with our proposal that triplet states are playing a role in photocatalysis. The larger enhancement brought by Br ion is in agreement with a larger magnitude of spin-orbit coupling. The photocatalytic enhancement is also dependent on the anion concentration in the solution, as shown in **Fig. 6.11b**. When a small amount of KBr (0.1 mL) added to the CDs solution, the hydrogen generation is only slightly enhanced. It increases notably when more KBr (0.1 mL) solution is added. As the spin-orbit coupling is a local effect depending on the distance between the electron and the heavy atom, higher concentration can decrease the distance between CDs and anions, and can lead to a higher quantum yield of triplet states.

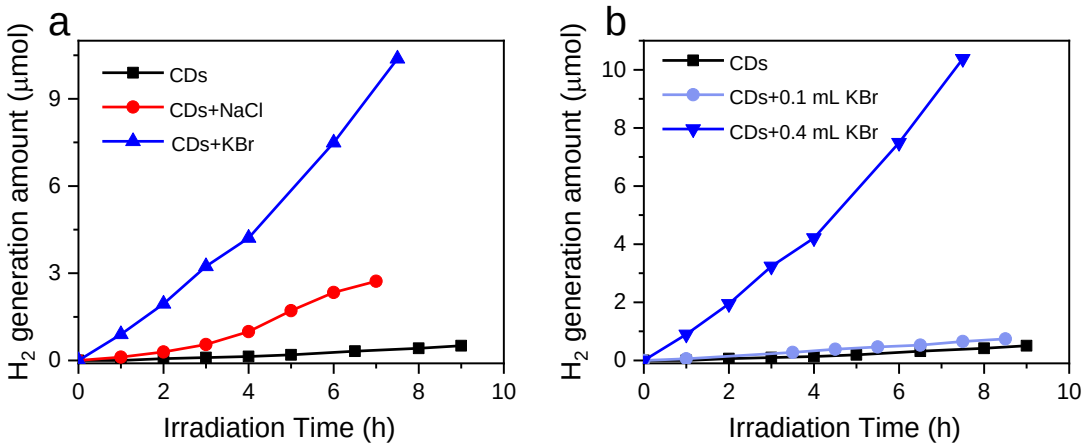

Figure 6.11 (a) The photocatalytic hydrogen generation of CDs added with same molar concentration of NaCl and KBr. (b) The hydrogen generation of CDs added with different amount of KBr.

The results indicate that the presence of heavy atom is beneficial to photocatalysis. However, no phosphorescence is detected in the water solution. We have to be cautious to make a statement that triplet states can be used in photocatalysis. Therefore, further experiments and TAS measurements are still needed to detect whether there are any species with a long lifetime.

In summary, the triplet states with a long lifetime correlate with photocatalytic performance, which is consistent with the results that heavy atom anion addition is beneficial to the photocatalytic performance. However, more experiments are needed to support the statement.

Chapter 7 Conclusions and summary

The motivation of this thesis is to apply organic materials/molecules to photocatalytic hydrogen generation taking advantage of their unique organic photophysical properties, including photobase effects and longlifetime . With optical spectroscopy, the related carrier dynamics and proton transfer can be delicately investigated. As the electronic structure of carbon dots can be easily tuned, metal-free CDs have been the focus materials in this thesis. It is the first time that classical organic photophysical properties are utilized in photocatalytic hydrogen generation instead of adopting the conventional methods in inorganic materials, such as doping.

Firstly, the photoinduced proton transfer (also named photobase effect) is applied to photocatalytic reaction. A model photobase, acridine, with pyridinic nitrogen was employed. The acridine is introduced into the nitrogen-free CDs system to form a hybrid. The non-photobasic CDs function as an electron donor and electron can transfer from CDs to the model photobasic molecule, acridine. As investigated by transient absorption spectroscopy, acridine in the excited state can pull a proton from the water at neutral pH within 30 ps, due to its photobasic property. The ultrafast proton transfer can notably reduce the time discrepancy between the proton diffusion and electron migration (~ps) to the surface, where the proton diffusion generally is around ~μs range. The proton-coupled electron transfer can substantially increase the photocatalytic performance. The photocatalytic hydrogen generation rate of the hybrid system has increased 4-10 times for acridine/CDs hybrid compared to free CDs This work provides significant insight that the photoinduced proton transfer is beneficial to photocatalytic performance. At the same time, it can pave the way to the design of nitrogen-containing efficient organic photocatalyst.

As nitrogen element is widely contained in many organic materials/molecules, the photobasic moieties can be their building block. Therefore, there is possibility that nitrogen-containing CDs are photobasic intrinsically. In the second work, nitrogen-containing CDs were designed and synthesized with the classical CDs precursors, citric acid and urea. The intrinsically photobasic character of CDs in water is proved by steady-state absorption and PL spectrometer, where the PL spectra redshift from 406 to 460 nm with proton donor addition. The photobase effect in CDs was further evidenced by ultrafast transient absorption spectroscopy. The timescale of photoinduced protonation was estimated around 2 ps, much faster than acridine. Moreover, stimulated emission appearing in the transient absorption spectroscopy exhibits the potential application of photobasic CDs in excimer laser. The photobasic CDs are proven to be an efficient photocatalyst which can outperform TiO_2. The control experiments show that only when the photobase effect manifest itself, the intrinsically photobasic CDs can show the photocatalytic activity. It further proves that photobase effect may be an essential part of the mechanism responsible for the photocatalytic water splitting.

Besides the proton diffusion, the electron lifetime is also a decisive parameter to photocatalytic performance. Triplet states usually have a much longer lifetime (>1 μs), reducing the time discrepancy between the electron lifetime and photoreaction (> ms). Therefore, it is plausible to utilize triplet states in photocatalytic hydrogen generation. The phosphorescent CDs can provide an opportunity to investigate the long-lifetime triplet states on the photocatalytic methanol-reforming, as the triplet states are reserved in methanol. Here an ISC inhibitor is added to control the quantum yield of intersystem crossing, as well as the quantum yield of triplet states. The consistency between reduced phosphorescence and declining photocatalytic activity indicates that the triplet states can be utilized in photocatalytic reactions. Given lifetime deconvolution, the triplet state with a $^3(n, \pi^*)$ configuration is probably decisive to methanol-reforming. The conclusion derived from methanol-reforming can also apply to the photocatalytic water splitting, as the heavy atom (Br, Cl) can notably boost the photocatalytic performance of non-phosphorescent CDs.

In summary, this thesis has presented a spectroscopic investigation of applying organic photophysical properties, photobase effect and long-lifetime triplet states, to the photocatalytic hydrogen generation. The photocatalytic activity is highly boosted when the photobase effect manifests itself. The triplet states with a long lifetime can be utilized in photocatalytic reactions. Through these attempts, the unique organic photophysical properties that cannot be found in inorganic semiconductor have shown to aid the photocatalytic reactions. Thus, organic materials/molecules with tunable electronic properties can be pinned with more hope to fulfil the aggressive goal of carbon neutrality.

Appendix

Acridine protonation equilibria

The reaction of water deprotonation by acridine is given by:

$$Ac + H_2O \rightleftarrows AcH^+ + OH^-$$

The equilibrium constant is then given by:

$$K = \frac{[AcH^+][OH^-]}{[Ac]}$$

The reaction of dissociation of acridine conjugated acid can be written as:

$$AcH^+ \rightleftarrows Ac + H^+$$

With the equilibrium constant $K_{a,Ac}$:

$$K_{a,Ac} = \frac{[Ac][H^+]}{[AcH^+]}$$

pK_a of acridine in the ground state is 5.5, in the excited state it rises to 10.7. For water the dissociation can be written as

$$H_2O \rightleftarrows H^+ + OH^-$$

with $K_{a,water}$ defined as

$$K_{a,water} = [H^+][OH^-]$$

pK_a of water equals 14, so that $K_{a,water} = 10^{-14}$. Combining the two reactions, K can be calculated as:

$$K = \frac{K_{a,water}}{K_{a,Ac}}$$

Hence, in the ground state of acridine, K equals $10^{-(14-5.5)} = 3.2 \cdot 10\text{-}9$. In the excited state, K equals $10^{-(14-10.7)} = 5.0 \cdot 10^{-4}$. From this the ratios of the concentrations of the protonated to deprotonated acridine can be calculated for any given pH:

$$\frac{[AcH^+]}{[Ac]} = \frac{K}{[OH^-]}$$

For instance, at pH 7 the ratio in the ground state is 0.032, so that around 3% of acridine molecules are protonated. In the excited state the ratio is ~5000, so that the majority of the acridine molecules are protonated. It should be noted that the deprotonation of water in a closed volume leads to the formation of OH^- anions that would increase the pH and

decrease the protonation ratio. However, the concentration of the saturated solution of acridine in water is only 0.25mM, so that the majority of excited acridine molecules should still be in the protonated form.

References

[1] A. Fujishima, K. Honda, Nature, 238 (1972) 37-38.
[2] B. O'regan, M. Grätzel, Nature, 353 (1991) 737-740.
[3] R. Asahi, T. Morikawa, T. Ohwaki, K. Aoki, Y. Taga, Science, 293 (2001) 269-271.
[4] A. Kudo, Y. Miseki, Chemical Society Reviews, 38 (2009) 253-278.
[5] X. Chen, S. Shen, L. Guo, S.S. Mao, Chemical Reviews, 110 (2010) 6503-6570.
[6] S.U. Khan, M. Al-Shahry, W.B. Ingler, Science, 297 (2002) 2243-2245.
[7] Z. Zou, J. Ye, K. Sayama, H. Arakawa, Nature, 414 (2001) 625-627.
[8] H. Tong, S. Ouyang, Y. Bi, N. Umezawa, M. Oshikiri, J. Ye, Advanced Materials, 24 (2012) 229-251.
[9] Q. Xiang, J. Yu, M. Jaroniec, Chemical Society Reviews, 41 (2012) 782-796.
[10] D.D. Dionysiou, G.L. Puma, J. Ye, J. Schneider, D. Bahnemann, Photocatalysis: Applications, Royal Society of Chemistry, 2016.
[11] J. Tang, J.R. Durrant, D.R. Klug, Journal of the American Chemical Society, 130 (2008) 13885-13891.
[12] T. Hisatomi, J. Kubota, K. Domen, Chemical Society Reviews, 43 (2014) 7520-7535.
[13] H. Kisch, Angewandte Chemie International Edition, 52 (2013) 812-847.
[14] A.L. Linsebigler, G. Lu, J.T. Yates Jr, Chemical Reviews, 95 (1995) 735-758.
[15] J. Yu, M. Jaroniec, C. Jiang, Surface Science of Photocatalysis, Academic Press2020.
[16] J.K. Stolarczyk, S. Bhattacharyya, L. Polavarapu, J. Feldmann, ACS Catalysis, 8 (2018) 3602-3635.
[17] A. Kubacka, M. Fernandez-Garcia, G. Colon, Chemical Reviews, 112 (2012) 1555-1614.
[18] W. Shockley, H.J. Queisser, Journal of Applied Physics, 32 (1961) 510-519.
[19] M. Shalom, S. Inal, C. Fettkenhauer, D. Neher, M. Antonietti, Journal of the American Chemical Society, 135 (2013) 7118-7121.
[20] S. Chen, L.W. Wang, Chemistry of Materials, 24 (2012) 3659-3666.
[21] J. Aldana, Y.A. Wang, X. Peng, Journal of the American Chemical Society, 123 (2001) 8844-8850.
[22] D. Meissner, R. Memming, B. Kastening, The Journal of Physical Chemistry, 92 (1988) 3476-3483.
[23] K. Tarafder, Y. Surendranath, J.H. Olshansky, A.P. Alivisatos, L.W. Wang, Journal of the American Chemical Society, 136 (2014) 5121-5131.
[24] K. Wu, Z. Chen, H. Lv, H. Zhu, C.L. Hill, T. Lian, Journal of the American Chemical Society, 136 (2014) 7708-7716.
[25] F.M. Pesci, A.J. Cowan, B.D. Alexander, J.R. Durrant, D.R. Klug, The Journal of Physical Chemistry Letters, 2 (2011) 1900-1903.
[26] G.R. Bamwenda, T. Uesigi, Y. Abe, K. Sayama, H. Arakawa, Applied Catalysis A: General, 205 (2001) 117-128.
[27] G. Hitoki, T. Takata, J.N. Kondo, M. Hara, H. Kobayashi, K. Domen, Chemical Communications, (2002) 1698-1699.
[28] A. Kudo, K. Asakura, H. Kato, Journal of the American Chemical Society, 125 (2003) 3082-3089.
[29] S. Yan, L. Wan, Z. Li, Z. Zou, Chemical Communications, 47 (2011) 5632-5634.
[30] R.A. Marcus, The Journal of Chemical Physics, 24 (1956) 966-978.
[31] A. Manzi, Y. Tong, J. Feucht, E.P. Yao, L. Polavarapu, A.S. Urban, J. Feldmann, Nature Communications, 9 (2018) 1-6.

[32] A. Mills, S. Le Hunte, Journal of Photochemistry and Photobiology A: Chemistry, 108 (1997) 1-35.
[33] W.J. Youngblood, S.H.A. Lee, K. Maeda, T.E. Mallouk, Accounts of Chemical Research, 42 (2009) 1966-1973.
[34] S.N. Habisreutinger, L. Schmidt-Mende, J.K. Stolarczyk, Angewandte Chemie International Edition, 52 (2013) 7372-7408.
[35] X. Liu, C.H. Yan, J.A. Capobianco, Chemical Society Reviews, 44 (2015) 1299-1301.
[36] J. Zhou, Q. Liu, W. Feng, Y. Sun, F. Li, Chemical Reviews, 115 (2015) 395-465.
[37] G. Chen, H. Qiu, P.N. Prasad, X. Chen, Chemical Reviews, 114 (2014) 5161-5214.
[38] B. Zhou, B. Shi, D. Jin, X. Liu, Nature Nanotechnology, 10 (2015) 924-936.
[39] M. Haase, H. Schäfer, Angewandte Chemie International Edition, 50 (2011) 5808-5829.
[40] W. Qin, D. Zhang, D. Zhao, L. Wang, K. Zheng, Chemical Communications, 46 (2010) 2304-2306.
[41] S. Obregón, A. Kubacka, M. Fernández-García, G. Colón, Journal of Catalysis, 299 (2013) 298-306.
[42] W. Fan, H. Bai, W. Shi, CrystEngComm, 16 (2014) 3059-3067.
[43] W.S. Han, K.R. Wee, H.Y. Kim, C. Pac, Y. Nabetani, D. Yamamoto, T. Shimada, H. Inoue, H. Choi, K. Cho, Chemistry–A European Journal, 18 (2012) 15368-15381.
[44] E. Bae, W. Choi, The Journal of Physical Chemistry B, 110 (2006) 14792-14799.
[45] K. Maeda, M. Eguchi, W.J. Youngblood, T.E. Mallouk, Chemistry of Materials, 20 (2008) 6770-6778.
[46] P.V. Kamat, The Journal of Physical Chemistry Letters, 3 (2012) 663-672.
[47] P.A. Sant, P.V. Kamat, Physical Chemistry Chemical Physics, 4 (2002) 198-203.
[48] J. Hensel, G. Wang, Y. Li, J.Z. Zhang, Nano Letters, 10 (2010) 478-483.
[49] L. Polavarapu, S. Mourdikoudis, I. Pastoriza-Santos, J. Pérez-Juste, CrystEngComm, 17 (2015) 3727-3762.
[50] L.M. Liz-Marzán, Langmuir, 22 (2006) 32-41.
[51] S. Linic, P. Christopher, D.B. Ingram, Nature Materials, 10 (2011) 911-921.
[52] W. Hou, S.B. Cronin, Advanced Functional Materials, 23 (2013) 1612-1619.
[53] S. Mubeen, G. Hernandez-Sosa, D. Moses, J. Lee, M. Moskovits, Nano Letters, 11 (2011) 5548-5552.
[54] M. Wang, M. Ye, J. Iocozzia, C. Lin, Z. Lin, Advanced Science, 3 (2016) 1600024.
[55] N. Zhou, V. López-Puente, Q. Wang, L. Polavarapu, I. Pastoriza-Santos, Q.H. Xu, RSC Advances, 5 (2015) 29076-29097.
[56] K. Maeda, K. Domen, The Journal of Physical Chemistry C, 111 (2007) 7851-7861.
[57] Z.H. Cui, H. Jiang, The Journal of Physical Chemistry C, 121 (2017) 3241-3251.
[58] F. Yoshitomi, K. Sekizawa, K. Maeda, O. Ishitani, ACS Applied Materials & Interfaces, 7 (2015) 13092-13097.
[59] G. Sahara, H. Kumagai, K. Maeda, N. Kaeffer, V. Artero, M. Higashi, R. Abe, O. Ishitani, Journal of the American Chemical Society, 138 (2016) 14152-14158.
[60] G. Sahara, O. Ishitani, Inorganic Chemistry, 54 (2015) 5096-5104.
[61] X. Chen, L. Liu, Y.Y. Peter, S.S. Mao, Science, 331 (2011) 746-750.
[62] Y.H. Hu, Angewandte Chemie International Edition, 51 (2012) 12410-12412.
[63] N. Serpone, D. Lawless, R. Khairutdinov, The Journal of Physical Chemistry, 99 (1995) 16646-16654.
[64] D.W. Bahnemann, M. Hilgendorff, R. Memming, The Journal of Physical Chemistry B, 101 (1997) 4265-4275.

[65] M.J. Berr, A. Vaneski, C. Mauser, S. Fischbach, A.S. Susha, A.L. Rogach, F. Jäckel, J. Feldmann, Small, 8 (2012) 291-297.
[66] J.L. White, M.F. Baruch, J.E. Pander III, Y. Hu, I.C. Fortmeyer, J.E. Park, T. Zhang, K. Liao, J. Gu, Y. Yan, Chemical Reviews, 115 (2015) 12888-12935.
[67] Y. Wang, Q. Wang, X. Zhan, F. Wang, M. Safdar, J. He, Nanoscale, 5 (2013) 8326-8339.
[68] T. Teranishi, M. Sakamoto, The Journal of Physical Chemistry Letters, 4 (2013) 2867-2873.
[69] C.Y. Jimmy, L. Wu, J. Lin, P. Li, Q. Li, Chemical Communications, (2003) 1552-1553.
[70] T. Simon, M.T. Carlson, J.K. Stolarczyk, J. Feldmann, ACS Energy Letters, 1 (2016) 1137-1142.
[71] L. Amirav, A.P. Alivisatos, The Journal of Physical Chemistry Letters, 1 (2010) 1051-1054.
[72] M.J. Berr, P. Wagner, S. Fischbach, A. Vaneski, J. Schneider, A.S. Susha, A.L. Rogach, F. Jäckel, J. Feldmann, Applied Physics Letters, 100 (2012) 223903.
[73] X. Xu, R. Ray, Y. Gu, H.J. Ploehn, L. Gearheart, K. Raker, W.A. Scrivens, Journal of the American Chemical Society, 126 (2004) 12736-12737.
[74] Y.P. Sun, B. Zhou, Y. Lin, W. Wang, K.S. Fernando, P. Pathak, M.J. Meziani, B.A. Harruff, X. Wang, H. Wang, Journal of the American Chemical Society, 128 (2006) 7756-7757.
[75] J.C.E. da Silva, H.M. Gonçalves, TrAC Trends in Analytical Chemistry, 30 (2011) 1327-1336.
[76] Z. Kang, S.T. Lee, Nanoscale, 11 (2019) 19214-19224.
[77] H. Li, X. He, Z. Kang, H. Huang, Y. Liu, J. Liu, S. Lian, Angew Chem Int Edit, 49(2010)4430-4434.
[78] N. Suzuki, Y. Wang, P. Elvati, Z.B. Qu, K. Kim, S. Jiang, E. Baumeister, J. Lee, B. Yeom, J.H. Bahng, J. Lee, A. Violi, N.A. Kotov, ACS Nano, 10 (2016) 1744-1755.
[79] F. Yuan, T. Yuan, L. Sui, Z. Wang, Z. Xi, Y. Li, X. Li, L. Fan, Z.a. Tan, A. Chen, Nature Communications, 9 (2018) 1-11.
[80] B. Yao, H. Huang, Y. Liu, Z. Kang, Trends in Chemistry, 1 (2019) 235-246.
[81] A.B. Bourlinos, A. Stassinopoulos, D. Anglos, R. Zboril, M. Karakassides, E.P. Giannelis, Small, 4 (2008) 455-458.
[82] Z. Gan, X. Wu, G. Zhou, J. Shen, P.K. Chu, Advanced Optical Materials, 1 (2013) 554-558.
[83] H.M. Goncalves, A.J. Duarte, J.C.E. da Silva, Biosensors and Bioelectronics, 26 (2010) 1302-1306.
[84] Y. Li, X. Zheng, X. Zhang, S. Liu, Q. Pei, M. Zheng, Z. Xie, Advanced Healthcare Materials, 6 (2017) 1600924.
[85] P.G. Luo, S. Sahu, S.T. Yang, S.K. Sonkar, J. Wang, H. Wang, G.E. LeCroy, L. Cao, Y.P. Sun, Journal of Materials Chemistry B, 1 (2013) 2116-2127.
[86] Q. Wang, X. Huang, Y. Long, X. Wang, H. Zhang, R. Zhu, L. Liang, P. Teng, H. Zheng, Carbon, 59 (2013) 192-199.
[87] H. Yu, R. Shi, Y. Zhao, G.I. Waterhouse, L.Z. Wu, C.H. Tung, T. Zhang, Advanced Materials, 28 (2016) 9454-9477.
[88] F. Arcudi, L. Đorđević, M. Prato, Angewandte Chemie International Edition, 56 (2017) 4170-4173.
[89] J. Zhang, Y. Yuan, G. Liang, S.H. Yu, Advanced Science, 2 (2015) 1500002.
[90] X. Miao, D. Qu, D. Yang, B. Nie, Y. Zhao, H. Fan, Z. Sun, Advanced materials, 30 (2018) 1704740.
[91] J. Ge, Q. Jia, W. Liu, L. Guo, Q. Liu, M. Lan, H. Zhang, X. Meng, P. Wang, Advanced Materials, 27 (2015) 4169-4177.
[92] J. Schneider, C.J. Reckmeier, Y. Xiong, M. von Seckendorff, A.S. Susha, P. Kasák, A.L. Rogach, The Journal of Physical Chemistry C, 121 (2017) 2014-2022.
[93] M. Fu, F. Ehrat, Y. Wang, K.Z. Milowska, C. Reckmeier, A.L. Rogach, J.K. Stolarczyk, A.S. Urban, J. Feldmann, Nano Letters, 15 (2015) 6030-6035.

[94] J.A. Sichert, Y. Tong, N. Mutz, M. Vollmer, S. Fischer, K.Z. Milowska, R. García Cortadella, B. Nickel, C. Cardenas-Daw, J.K. Stolarczyk, Nano Letters, 15 (2015) 6521-6527.
[95] Y. Wang, N. Herron, The Journal of Physical Chemistry, 95 (1991) 525-532.
[96] S.N. Baker, G.A. Baker, Angewandte Chemie International Edition, 49 (2010) 6726-6744.
[97] S. Zhu, Y. Song, X. Zhao, J. Shao, J. Zhang, B. Yang, Nano Research, 8 (2015) 355-381.
[98] L. Li, G. Wu, G. Yang, J. Peng, J. Zhao, J.J. Zhu, Nanoscale, 5 (2013) 4015-4039.
[99] X.T. Zheng, A. Ananthanarayanan, K.Q. Luo, P. Chen, Small, 11 (2015) 1620-1636.
[100] R.J. Fan, Q. Sun, L. Zhang, Y. Zhang, A.H. Lu, Carbon, 71 (2014) 87-93.
[101] W. Liu, C. Li, Y. Ren, X. Sun, W. Pan, Y. Li, J. Wang, W. Wang, Journal of Materials Chemistry B, 4 (2016) 5772-5788.
[102] K. Jiang, S. Sun, L. Zhang, Y. Lu, A. Wu, C. Cai, H. Lin, Angewandte Chemie, 127 (2015) 5450-5453.
[103] J. Fang, T. Debnath, S. Bhattacharyya, M. Döblinger, J. Feldmann, J.K. Stolarczyk, Nature Communications, 11 (2020) 1-8.
[104] X. Wang, L. Cao, F. Lu, M.J. Meziani, H. Li, G. Qi, B. Zhou, B.A. Harruff, F. Kermarrec, Y.P. Sun, Chemical Communications, (2009) 3774-3776.
[105] M.L. Liu, B.B. Chen, C.M. Li, C.Z. Huang, Green Chemistry, 21 (2019) 449-471.
[106] L. Bao, Z.L. Zhang, Z.Q. Tian, L. Zhang, C. Liu, Y. Lin, B. Qi, D.W. Pang, Advanced Materials, 23 (2011) 5801-5806.
[107] H. Ding, S.B. Yu, J.S. Wei, H.M. Xiong, ACS Nano, 10 (2016) 484-491.
[108] L. Wang, S.J. Zhu, H.Y. Wang, S.N. Qu, Y.L. Zhang, J.H. Zhang, Q.D. Chen, H.L. Xu, W. Han, B. Yang, ACS Nano, 8 (2014) 2541-2547.
[109] H. Tetsuka, R. Asahi, A. Nagoya, K. Okamoto, I. Tajima, R. Ohta, A. Okamoto, Advanced Materials, 24 (2012) 5333-5338.
[110] F. Yuan, Y.K. Wang, G. Sharma, Y. Dong, X. Zheng, P. Li, A. Johnston, G. Bappi, J.Z. Fan, H. Kung, Nature Photonics, 14 (2020) 171-176.
[111] B. Zhao, Z. Wang, Z.a. Tan, Nature Photonics, 14 (2020) 130-131.
[112] Z. Xie, Z. Yin, Y. Wu, C. Liu, X. Hao, Q. Du, X. Xu, Scientific Reports, 7 (2017) 1-9.
[113] A. Singh, A. Wolff, S.D. Yambem, M. Esmaeili, J.D. Riches, M. Shahbazi, K. Feron, E. Eftekhari, K.K. Ostrikov, Q. Li, Advanced Materials, 32 (2020).
[114] M.B. Alam, K. Yadav, D. Shukla, R. Srivastava, J. Lahiri, A.S. Parmar, ChemistrySelect, 4 (2019) 7450-7454.
[115] K.S. Fernando, S. Sahu, Y. Liu, W.K. Lewis, E.A. Guliants, A. Jafariyan, P. Wang, C.E. Bunker, Y.P. Sun, ACS applied materials & interfaces, 7 (2015) 8363-8376.
[116] C. Hu, M. Li, J. Qiu, Y.P. Sun, Chemical Society Reviews, 48 (2019) 2315-2337.
[117] H. Li, X. He, Z. Kang, H. Huang, Y. Liu, J. Liu, S. Lian, C.H.A. Tsang, X. Yang, S.T. Lee, Angewandte Chemie, 122 (2010) 4532-4536.
[118] H. Li, R. Liu, S. Lian, Y. Liu, H. Huang, Z. Kang, Nanoscale, 5 (2013) 3289-3297.
[119] Z. Ma, H. Ming, H. Huang, Y. Liu, Z. Kang, New Journal of Chemistry, 36 (2012) 861-864.
[120] S. Bhattacharyya, F. Ehrat, P. Urban, R. Teves, R. Wyrwich, M. Döblinger, J. Feldmann, A.S. Urban, J.K. Stolarczyk, Nature Communications, 8 (2017) 1-9.
[121] S.Y. Lim, W. Shen, Z. Gao, Chemical Society Reviews, 44 (2015) 362-381.
[122] S. Fang, Y. Xia, K. Lv, Q. Li, J. Sun, M. Li, Applied Catalysis B: Environmental, 185 (2016) 225-232.

[123] H. Yu, Y. Zhao, C. Zhou, L. Shang, Y. Peng, Y. Cao, L.Z. Wu, C.H. Tung, T. Zhang, Journal of Materials Chemistry A, 2 (2014) 3344-3351.
[124] J. Liu, Y. Liu, N. Liu, Y. Han, X. Zhang, H. Huang, Y. Lifshitz, S.T. Lee, J. Zhong, Z. Kang, Science, 347 (2015) 970-974.
[125] P.W. Atkins, R.S. Friedman, Molecular Quantum Mechanics, Oxford University Press, 2011.
[126] N.J. Turro, V. Ramamurthy, J.C. Scaiano, Principles of Molecular Photochemistry: An Introduction, University Science Book, 2009.
[127] M. Karelson, M.C. Zerner, Journal of the American Chemical Society, 112 (1990) 9405-9406.
[128] G.G. Guilbault, Practical Fluorescence, CRC Press, 2020.
[129] P. Klán, J. Wirz, Photochemistry of Organic Compounds: from Concepts to Practice, John Wiley & Sons, 2009.
[130] H.H. Jaffé, M. Orchin, Theory and Applications of Ultraviolet Spectroscopy, John Wiley & Sons, 1962.
[131] M. Klessinger, J. Michl, Excited States and Photochemistry of Organic Molecules, VCH Publishers, 1995.
[132] I. Pelant, J. Valenta, Luminescence Spectroscopy of Semiconductors, Oxford University Press, 2012.
[133] V. Balzani, P. Ceroni, A. Juris, Photochemistry and Photophysics: Concepts, Research, Applications, John Wiley & Sons, 2014.
[134] G.W. Robinson, R. Frosch, The Journal of Chemical Physics, 38 (1963) 1187-1203.
[135] G.W. Robinson, R.P. Frosch, The Journal of Chemical Physics, 37 (1962) 1962-1973.
[136] W. Siebrand, The Journal of Chemical Physics, 46 (1967) 440-447.
[137] W. Siebrand, The Journal of Chemical Physics, 47 (1967) 2411-2422.
[138] B. Valeur, Digital Encyclopedia of Applied Physics, (2003) 477-531.
[139] W. Zhao, Z. He, B.Z. Tang, Nature Reviews Materials, (2020) 1-17.
[140] J.R. Lakowicz, Principles of Fluorescence Spectroscopy, Springer Science & Business Media, 2013.
[141] W. Sheng, M. Nairat, P.D. Pawlaczyk, E. Mroczka, B. Farris, E. Pines, J.H. Geiger, B. Borhan, M. Dantus, Angewandte Chemie International Edition, 57 (2018) 14742-14746.
[142] J.R. Hunt, J.M. Dawlaty, The Journal of Physical Chemistry A, 122 (2018) 7931-7940.
[143] E.W. Driscoll, J.R. Hunt, J.M. Dawlaty, The Journal of Physical Chemistry A, 121 (2017) 7099-7107.
[144] E.T. Ryan, T. Xiang, K.P. Johnston, M.A. Fox, The Journal of Physical Chemistry A, 101 (1997) 1827-1835.
[145] G. Favaro, U. Mazzucato, F. Masetti, The Journal of Physical Chemistry, 77 (1973) 601-604.
[146] J.R. Hunt, C. Tseng, J.M. Dawlaty, Faraday Discussions, 216 (2019) 252-268.
[147] J.R. Hunt, J.M. Dawlaty, The Journal of Physical Chemistry A, 123 (2019) 10372-10380.
[148] M. Klessinger, Angewandte Chemie International Edition in English, 34 (1995) 549-551.
[149] G. Méhes, H. Nomura, Q. Zhang, T. Nakagawa, C. Adachi, Angewandte Chemie International Edition, 51 (2012) 11311-11315.
[150] T. Nakagawa, S.Y. Ku, K.T. Wong, C. Adachi, Chemical Communications, 48 (2012) 9580-9582.
[151] K. Nasu, T. Nakagawa, H. Nomura, C.J. Lin, C.H. Cheng, M.R. Tseng, T. Yasuda, C. Adachi, Chemical Communications, 49 (2013) 10385-10387.
[152] Z. He, C. Ke, B.Z. Tang, ACS Omega, 3 (2018) 3267-3277.

[153] K. Byrappa, M. Yoshimura, Handbook of Hydrothermal Technology, William Andrew, 2012.
[154] K. Byrappa, T. Adschiri, Progress in Crystal Growth And Characterization of Materials, 53 (2007) 117-166.
[155] C. Xia, S. Zhu, T. Feng, M. Yang, B. Yang, Advanced Science, 6 (2019) 1901316.
[156] G.A. Hutton, B.C. Martindale, E. Reisner, Chemical Society Reviews, 46 (2017) 6111-6123.
[157] W. Kasprzyk, T. Świergosz, S. Bednarz, K. Walas, N.V. Bashmakova, D. Bogdał, Nanoscale, 10 (2018) 13889-13894.
[158] F. Ehrat, S. Bhattacharyya, J. Schneider, A. Löf, R. Wyrwich, A.L. Rogach, J.K. Stolarczyk, A.S. Urban, J. Feldmann, Nano Letters, 17 (2017) 7710-7716.
[159] H. Li, S. Ye, J. Guo, J. Kong, J. Song, Z. Kang, Journal of Materials Chemistry C, 7 (2019) 10605-10612.
[160] W.I. Goldburg, American Journal of Physics, 67 (1999) 1152-1160.
[161] M. Kaszuba, D. McKnight, M.T. Connah, F.K. McNeil-Watson, U. Nobbmann, Journal of Nanoparticle Research, 10 (2008) 823-829.
[162] J.R. Lakowicz, A. Balter, Biophysical Chemistry, 16 (1982) 117-132.
[163] B.J. Bohn, Exciton Dynamics in Lead Halide Perovskite Nanocrystals: Recombination, Dephasing and Diffusion, Springer Nature, 2019.
[164] U. Megerle, I. Pugliesi, C. Schriever, C.F. Sailer, E. Riedle, Applied Physics B, 96 (2009) 215-231.
[165] M.R. Son, Y.J. Cho, S.Y. Kim, H.J. Son, D.W. Cho, S.O. Kang, Physical Chemistry Chemical Physics, 19 (2017) 24485-24492.
[166] E.O. Danilov, I.E. Pomestchenko, S. Kinayyigit, P.L. Gentili, M. Hissler, R. Ziessel, F.N. Castellano, The Journal of Physical Chemistry A, 109 (2005) 2465-2471.
[167] R.M. Jay, S. Eckert, V. Vaz da Cruz, M. Fondell, R. Mitzner, A. Föhlisch, Angewandte Chemie International Edition, 58 (2019) 10742-10746.
[168] J.D. Braun, I.B. Lozada, C. Kolodziej, C. Burda, K.M. Newman, J. van Lierop, R.L. Davis, D.E. Herbert, Nature Chemistry, 11 (2019) 1144-1150.
[169] R. Berera, R. van Grondelle, J.T. Kennis, Photosynthesis Research, 101 (2009) 105-118.
[170] D. Giovanni, W.K. Chong, Y.Y.F. Liu, H.A. Dewi, T. Yin, Y. Lekina, Z.X. Shen, N. Mathews, C.K. Gan, T.C. Sum, Advanced Science, 5 (2018) 1800664.
[171] M.B. Price, J. Butkus, T.C. Jellicoe, A. Sadhanala, A. Briane, J.E. Halpert, K. Broch, J.M. Hodgkiss, R.H. Friend, F. Deschler, Nature Communications, 6 (2015) 1-8.
[172] S. Aharon, I. Gdor, C. Yang, L. Etgar, S. Ruhman, Journal of Materials Chemistry A, 4 (2016) 3546-3553.
[173] P. Schiettecatte, P. Geiregat, Z. Hens, The Journal of Physical Chemistry C, 123 (2019) 10571-10577.
[174] M.T. Trinh, X. Wu, D. Niesner, X.Y. Zhu, Journal of Materials Chemistry A, 3 (2015) 9285-9290.
[175] V.Y. Artyukhov, T. Kopylova, L. Samsonova, N. Selivanov, V. Plotnikov, V. Sazhnikov, A. Khlebunov, G. Mayer, M. Alfimov, Russian Physics Journal, 51 (2008) 1097-1111.
[176] Ò. Rubio-Pons, L. Serrano-Andrés, M. Merchán, The Journal of Physical Chemistry A, 105 (2001) 9664-9673.
[177] K. Kasama, K. Kikuchi, S. Yamamoto, K. Ujiie, Y. Nishida, H. Kokubun, The Journal of Physical Chemistry, 85 (1981) 1291-1296.
[178] L.A. Diverdi, M.R. Topp, The Journal of Physical Chemistry, 88 (1984) 3447-3451.
[179] X. Liu, T.N. Karsili, A.L. Sobolewski, W. Domcke, The Journal of Physical Chemistry B, 119

(2015) 10664-10672.
[180] T.T. Eisenhart, J.L. Dempsey, Journal of the American Chemical Society, 136 (2014) 12221-12224.
[181] X. Liu, T.N. Karsili, A.L. Sobolewski, W. Domcke, Chemical Physics, 464 (2016) 78-85.
[182] L. Yang, W. Jiang, L. Qiu, X. Jiang, D. Zuo, D. Wang, L. Yang, Nanoscale, 7 (2015) 6104-6113.
[183] N. Elgrishi, K.J. Rountree, B.D. McCarthy, E.S. Rountree, T.T. Eisenhart, J.L. Dempsey, Journal of Chemical Education, 95 (2018) 197-206.
[184] J. Rak, J. Blazejowski, R.J. Zauhar, The Journal of Organic Chemistry, 57 (1992) 3720-3725.
[185] Y. Hirata, I. Tanaka, Chemical Physics Letters, 41 (1976) 336-338.
[186] S. Hammes-Schiffer, A.A. Stuchebrukhov, Chemical Reviews, 110 (2010) 6939-6960.
[187] O.F. Mohammed, D. Pines, E.T. Nibbering, E. Pines, Angewandte Chemie, 119 (2007) 1480-1483.
[188] S.A. Machado, L. Avaca, Electrochimica Acta, 39 (1994) 1385-1391.
[189] R. Casadio, B. Melandri, Journal of bioenergetics and Biomembranes, 9 (1977) 17-29.
[190] T. Hisatomi, K. Takanabe, K. Domen, Catalysis Letters, 145 (2015) 95-108.
[191] D.D. Perrin, B. Dempsey, E.P. Serjeant, pKa Prediction for Organic Acids and Bases, Springer, 1981.
[192] L. Zhao, F. Di, D. Wang, L.H. Guo, Y. Yang, B. Wan, H. Zhang, Nanoscale, 5 (2013) 2655-2658.
[193] M. Tan, L. Zhang, R. Tang, X. Song, Y. Li, H. Wu, Y. Wang, G. Lv, W. Liu, X. Ma, Talanta, 115 (2013) 950-956.
[194] A. Konwar, N. Gogoi, G. Majumdar, D. Chowdhury, Carbohydrate polymers, 115 (2015) 238-245.
[195] L. Wang, H.Y. Wang, Y. Wang, S.J. Zhu, Y.L. Zhang, J.H. Zhang, Q.D. Chen, W. Han, H.L. Xu, B. Yang, Advanced materials, 25 (2013) 6539-6545.
[196] A. Köhler, H. Bässler, Electronic processes in organic semiconductors: An introduction, John Wiley & Sons2015.
[197] Q. Wu, F. Huang, M. Zhao, J. Xu, J. Zhou, Y. Wang, Nano Energy, 24 (2016) 63-71.
[198] T. Simon, N. Bouchonville, M.J. Berr, A. Vaneski, A. Adrović, D. Volbers, R. Wyrwich, M. Döblinger, A.S. Susha, A.L. Rogach, Nature Materials, 13 (2014) 1013-1018.
[199] D.W. Wakerley, M.F. Kuehnel, K.L. Orchard, K.H. Ly, T.E. Rosser, E. Reisner, Nature Energy, 2 (2017) 1-9.
[200] P. Wang, B. Huang, Y. Dai, M.H. Whangbo, Physical Chemistry Chemical Physics, 14 (2012) 9813-9825.
[201] R. Konta, T. Ishii, H. Kato, A. Kudo, The Journal of Physical Chemistry B, 108 (2004) 8992-8995.
[202] H. Wu, L. Gu, G.V. Baryshnikov, H. Wang, B.F. Minaev, H. Ågren, Y. Zhao, ACS Applied Materials & Interfaces, 12 (2020) 20765-20774.
[203] Q. Li, M. Zhou, M. Yang, Q. Yang, Z. Zhang, J. Shi, Nature Communications, 9 (2018) 1-8.
[204] R. Tian, S.M. Xu, Q. Xu, C. Lu, Science Advances, 6 (2020) eaaz6107.
[205] M. Kitamura, H. Baba, Bulletin of the Chemical Society of Japan, 48 (1975) 1191-1195.

Acknowledgement

As a foreign student from China, I travel thousands of miles to this country, hold back the thoughts of my dearest family members and friends, and experience numerous difficulties before finishing this doctoral dissertation. In these seemingly short four years, I start my organic photophysics research from scratch and complete three interesting and meaningful projects. The whole process is like a dream, as if I only joined the group yesterday and met **Dr. Santanu Bhattacharya** smoking at the door at Amalienstr. 54.

To start with, I have a strong desire to thank my "Doktorvater" **Prof. Dr. Jochen Feldmann**, who is willing to accept me as his student. I know him before I start to know LMU and the great country Germany. His meaningful research and in-deep knowledge of semiconductor generates powerful "Coulomb force" in real life and attracts me here from 8,000 km away. During the four years, I cannot value his support highly enough. His critical view to research and his perseverance to seek the physical truth has pushed me to take a step further. His rigorous attitude towards research always inspires me to ask myself "what is new" before starting a new project. This rigorous attitude also drives me to self-learn and know better of organic photophysics principles. The fruitful discussions benefit me greatly, as I can always get sobering inputs from him. Therefore, I always expect to have a new discussion with him. I am also very thankful to his trust and the opportunities he gives to present my research results in front of different audience. It is also my first time to realize that research does not end in publishing a paper but extend to convince people. I thank him for all the opportunities and trust he has given to me.

I also want to thank **Dr. Jacek K. Stolarczyk**. As a tutor, he is patient and meticulous with every idea/project I come up with and provides constructive suggestions. From the beginning I joined the group, he has been very patient and tolerant. He is always generous to share his time, physics knowledge, and scientific experiences with us, and I benefit a lot from that. He is also a master of making a presentation and giving lectures, which is amazing. I regret missing his lectures in the first year. He always keeps a smiling face and be kind to everyone. He is also a "laughter spreader" as he always has jokes prepared.

The chair is also a gathering place for the most excellent. Many of them have been my role models as they are experienced in both physical theory and hands-on ability. To be more specific, not only can they generate excellent and interesting ideas, but also can manipulate every facility and solve all the problems encountered. Besides that, they are generous and willing to offer help, and never show their impatience. I have to express my special thanks to **Dr. Tushar Debnath**, **Dr. Enping Yao**, **Dr. Alexander Richter**, **Dr. Amrita Dey**, **Dr. Benhard Bohn**, **Sebastian Rieger**, **Florian Ehart** and **Ilka Vincon**. **Dr. Tushar Debnath**, **Dr. Enping Yao** and **Dr. Alexander Richter** gave me all the help whenever I needed. I am very thankful to that. Among these, **Dr. Tushar Debnath, Dr. Enping Yao** and **Dr. Santanu Bhattacharya** are also my collaborators. Through daily communication and discussion

with them, I gain a deeper physical understanding of the project and some of the misunderstanding physics concepts were corrected through discussions. They are like the Sun, making me warm-hearted. **Dr. Yiou Wang** is a very clever person and has plenty of interesting ideas and work very efficiently. He helps a lot especially for the second work. I hope we can collaborate more in the near future.

Special thanks are given to my dear colleagues and friends who helped me proofreading this thesis: **Dr. Jacek K. Stolarczyk, Dr. Tushar Debnath**, **Dr. Yiou Wang, Sebastian Rieger, Dr. Amrita Dey, Ilka Vincon, Anja Barfüßer**, and **Qi Chang** (Shanghai Jiaotong University), **Chao Wang** (University College London). Especially **Dr. Jacek K. Stolarczyk, Dr. Tushar Debnath** and **Dr. Yiou Wang** proofread every chapter and gave constructive suggestions.

The great colleagues and lunch/coffee breaks also make the daily work enjoyable. Therefore, I also want to express my gratitude to them who enriched my life: especially to **Dr. Tushar Debnath**, **Dr. Enping Yao**, **Dr. Amrita Dey**, **Dr. You Wang**, **Sharmistha Paul**, all other previously mentioned people and **Francis Schuknecht**, **Dr. Aurora Manzi**, **Nicola Kerschbaumer**, **Stefanie Pritzl**, **Simone Strohmair**, **Dr. He Huang**, **Dr. Lakshminarayana Polavarapu**, **Mariam Kurashvili**…

I also want to thank **Gerlinde Adam** for her patient and great help regarding administrative work. Many thanks go to **Stefan Niedermaier** and **Talee Barghouti** for the timely technical support in the laboratories. **Stefan Niedermaier** designed one temperature-controlled facility to meet my requirement and saved me a lot of time.

Last but not the least, I am especially grateful for the financial aid from China Scholarship Council. China is a misfortune shadowed but resilient country. I hope I can be a useful person and can contribute to our country's development. Meanwhile, I would like to thank my family and friends, especially my parents (**Shengjiao Wang**, **Fugui Fang**) and my girlfriend (**Xiaoli Zheng**) for their endless support, which gives me enormous encouragement in my four-year days of living alone.

With ageing going, my memory will get worse, and a lot of things are bound to flush in my head and occupy my brain memory. However, there will be enough space for the treasured memories of the four years in Germany and the adorable people in this chair.